

**3D Tomography of Ionospheric Anomalies
immediately before and after Large Earthquakes**



By
Ihsan Naufal Muafiry

Supervisor: Prof. Kosuke Heki

A dissertation submitted in partial fulfillment
of the requirements for the degree of
Doctor of Philosophy

Department of Natural History Science
Graduate School of Science, Hokkaido University

September 2021

Table of contents

Abstract	5
Acknowledgments.....	7
Chapter 1: Introduction	9
1.1 GNSS for Positioning.....	9
1.2 GNSS for Ionospheric Studies	10
1.3 Ionospheric Structure	12
1.4 Solid Earth and Ionosphere	14
1.5 Ionospheric Disturbance due to the Sea Surface Motion	16
1.6 Earthquake Precursors in Ionosphere.....	18
1.7 3D Tomography for Ionospheric Electron Density Anomalies	19
1.8 Research Objectives	20
Chapter 2: Data and Method.....	21
2.1 GNSS Network in Japan	21
2.2 GNSS Network in South Korea	22
2.3 GNSS Networks in South America.....	24
2.4 GNSS-TEC Method	25
2.5 Strategies to Isolate Anomalies from GNSS-TEC Data	28
2.6 Ionospheric 3D Tomography Method.....	29

Chapter 3: 3D Tomography of the Ionospheric Anomalies immediately before Earthquakes: The 2011 Tohoku-oki Earthquake	35
3.1 Introduction: History of Debate	36
3.2 Data set.....	39
3.3 Data Processing Strategy	40
3.3 Resolution tests	49
3.4 Tomography results	53
3.5 Growth and polarity balances of the preseismic anomalies.....	62
3.6 Discussion on the physical mechanism of the preseismic anomalies	63
Chapter 4: 3D Tomography of the Ionospheric Anomalies Before the 2010 Maule Earthquake, Chile: Comparison with the 2011 Tohoku-oki and 2015 Illapel Earthquake	68
4.1 Introduction: Structure of preseismic ionospheric anomalies.....	69
4.2 Data set.....	70
4.3 Data processing strategy	72
4.4 Resolution test.....	73
4.5 Tomography result.....	76
4.6 Comparison with the 2011 Tohoku-oki and 2015 Illapel Earthquakes	83
Chapter 5: 3D Tomography of the Ionospheric Anomalies after Earthquakes: The 2011 Tohoku-oki Earthquake	86

5.1	Introduction: Tsunamigenic ionospheric anomalies	87
5.2	Data set.....	87
5.3	Data processing strategy	87
5.4	Resolution tests	89
5.5	Tomography result.....	91
5.6	Physical mechanism of post-seismic anomalies	91
5.7	Origin of variety of waveforms.....	92
	Chapter 6: Conclusions and Recommendation	94
6.1	Conclusions.....	94
6.2	Recommendation	97

1 **Abstract**

2 A dense network of ground global navigation satellite system (GNSS) receivers detected
3 ionospheric total electron content (TEC) changes starting ~40 minutes before the 2011 Tohoku-
4 oki (M_w 9.0) earthquake around the ruptured fault, together with the long-lasting postseismic TEC
5 drop. In this study, I robustly estimate three-dimensional (3D) distribution of both pre- and post-
6 seismic ionospheric anomalies of the 2011 M_w 9.0 Tohoku-oki and the 2010 M_w 8.8 Maule
7 earthquakes by tomographic inversions of electron density anomalies. For the 2011 case, I set up
8 more than 6,000 blocks, as large as 1.0° (east-west) \times 0.9° (north-south) \times 60 km (vertical), over
9 the Japanese Islands, the Sea of Japan, and the Korean Peninsula, up to 870 km altitude. I used
10 slant-TEC residuals obtained using 8 satellites and 1,493 ground stations as inputs to the 3D
11 tomographic inversion. For the Maule earthquake, TEC data are obtained from 6 GNSS satellites
12 and 89 ground stations mainly in Chile and Argentina. I set up $>3,500$ blocks, with the size of 1.0°
13 (east-west) \times 1.2° (north-south) \times 75 km (vertical) for altitudes 75-750 km. I adopted objective
14 standards in determining reference curves of TEC from which the anomalies are defined. I
15 regularized the inversion by introducing two different constraints, the continuity constraint and
16 constraints around zero with altitude-dependent allowances. Performances of the 3D tomography
17 have been confirmed by various resolution tests for artificial patterns.

18 I compare the spatial and temporal distribution of the 3D structure of ionospheric electron
19 density anomalies immediately before these two megathrust earthquakes together with those of
20 another large earthquake (the 2015 M_w 8.3 Illapel) studied by He and Heki (2018). The results of
21 the three cases showed that the preseismic ionospheric anomalies have following common
22 features; (1) they are composed of pairs of low-altitude positive and high-altitude negative electron
5

23 density anomalies, (2) they occur above the land area close to the submarine faults, and (3) they
24 have clear onsets a few tens of minutes before earthquakes (~40 min before 2011 Tohoku-oki, and
25 Maule, and ~20 minutes before the Illapel earthquakes) and grow with decaying rates.

26 I hypothesize the physical process consistent with such 3D structure as follows. Electric
27 fields made by surface positive charges reach the ionosphere. The field generates electromotive
28 forces and makes electrons move down along geomagnetic fields, and this upward current makes
29 eastward/westward magnetic field in regions to the south/north of the epicenter before earthquakes
30 in northern/southern hemisphere. The current will continue until the induced electric field cancels
31 the external field made by surface charges, making the electric potential uniform along the
32 magnetic field. The current will depend on the along-field component of the external electric field
33 and the density of free electrons as a function of altitude. The nonuniform electric currents would
34 result in convergence/divergence of electrons and make positive/negative electron density
35 anomalies at the lower/higher ionosphere along the magnetic field, the structure consistent with
36 those found for these three earthquakes by 3D tomography. I will also compare strengths and
37 dimensions of the electron density anomalies before these three earthquakes and discuss future
38 perspective of preseismic ionospheric anomalies.

39

40 **Acknowledgments**

41 In the name of Allah, God, the greatest one,

42 First of all, I praise to Allah subhanahuwata'ala for the things He has given to me. Since in
43 the last three years period of my study, it is not only a journey of achieving a highest degree, but
44 also is becoming my greatest experience ever in my life. Indeed, the second place for all of these,
45 I would acknowledge my parents who have always been supporting and praying for me to go
46 further just for the sake of knowledge. Third place is without a doubt, I thank to my little family
47 (my wife and my children) who have been accompanying and supporting my journey in Japan as
48 well as coloring my new life.

49 Over the three years, an incredible number of people have been helping me a lot in my
50 journey. They deserve the gratitude of a thousand pages. First, I would like to express my sincere
51 gratitude to Prof. Kosuke Heki, my supervisor, who has given me opportunity to become greater
52 and smarter researcher. I learned many lessons and all of those are really valuable for my carrier
53 path. He taught me about programming with its technical aspects, making a presentation,
54 presenting slides, writing a scientific paper, and gave me chances to speak at international
55 conferences. Sensei inspires me, and I could not have written this thesis without that inspiration.
56 Thanks again sensei as always.

57 My sincere gratitude to Prof. Masato Furuya, Prof. Kiyoshi Yomogida, Dr. Kazunori
58 Yoshizawa, and Dr. Youichiro Takada for the advices delivered to my study during weekly solid-
59 earth science seminar or after the seminar. Those are definitely encouraging me to become better

60 and better in scientific field. Also, my colleagues at Space Geodesy and Seismology Laboratories.
61 I received many new perspectives of earth-sciences after discussing with them.

62 I thank the Geospatial Information Authority (GSI) for GEONET data (available from
63 terras.gsi.go.jp) and Electric Navigation Research Institute (ENRI) for the inter-frequency bias
64 data for GEONET stations (access www.enri.go.jp or write to Takeyasu Sakai sakai@enri.go.jp to
65 obtain the bias). I also thank Dr. Byung-Kyu Choi, Korea Astronomy and Space Science Institute,
66 for the Korean RINEX data files on March 11, 2011. One needs to write to bkchoi@kasi.re.kr to
67 access the Korean data. I thank Dr. He Liming, Northeast University, for helpful comments. It is
68 also grateful to have GIM data from University of Berne, Switzerland. Thanks for providing them.

69 Finally, I thank the Ministry of Education, Culture, Sports, Science and Technology
70 (MEXT) who supported me financially during my PhD study in Hokkaido University.

71

72 **Chapter 1: Introduction**

73 **1.1 GNSS for Positioning**

74 The era of precise positioning system available worldwide started by the launches of the
75 global navigation satellite system (GNSS) satellites in late 1980s. The Global Positioning Systems
76 (GPS), maintained by the United States, is the first GNSS with a constellation of satellites orbiting
77 the earth at altitude $\sim 20,000$ km. GPS is designed to extract the positions and velocities of moving
78 objects in three-dimensional (3D) space continuously all over the world regardless of weather and
79 time. Such information used to be only for military purposes and closed for civilian services.
80 Nowadays, the technology is available for everyone, thus the position of any objects around the
81 globe can be obtained using various GNSS including GPS.

82 There are several GNSS newer than GPS. The Russian GNSS, called Globalnoya
83 Navigatsionnaya Sputnikovaya Sistema (GLONASS) is orbiting the earth at altitudes somewhat
84 lower than those of GPS, $\sim 19,000$ km above the earth's surface. Galileo (European Navigation
85 System) flies at $\sim 23,000$ km altitude whereas some of the Chinese GNSS satellites (Beidou, BDS)
86 and the Japanese navigation satellites (Quasi-Zenith Satellite System, QZSS) employ much higher
87 geostationary and quasi-zenith orbits, respectively. Wherever they are, all the GNSS satellites
88 transmit microwave signals to earth to enable global navigation.

89 By measuring distances between an object (equipped with a GNSS receiver) and satellites,
90 we can exactly tell where the object is. GNSS satellites transmit digital information about e.g.
91 satellite orbits, clocks, as well as the satellite condition, using two L-band microwave carriers,
92 which are often called L1 and L2 (and sometimes additional L5).

93 The national datum for surveying and mapping in a country is often maintained by GNSS,
94 for example by building control points with precise GNSS surveying. The latitude and longitude
95 measured by GNSS at one control point are defined on a reference ellipsoid of the earth, and the
96 height can be directly measured relative to the ellipsoid instead of the local mean sea level. The
97 standard ellipsoidal model widely used for GNSS is World Geodetic System 1984 (WGS-84). By
98 establishing ties to reference systems, GNSS has improved the accuracy and consistency with the
99 national datum so that it can be used for further scientific applications.

100 The microwave signals from GNSS satellites face delays caused by two layers of the
101 earth's atmosphere before they reach receivers on the ground. The first layer is the ionosphere
102 (ionized upper atmosphere) and the second is the troposphere (both water vapor and dry
103 atmosphere). Atmospheric delays that occur in microwaves cause serious positioning errors, and
104 precise positioning by GNSS needs to consider these atmospheric delays in processing the GNSS
105 data. On the other hand, existence of such delays in the microwave signals enables us to study
106 changes in these two layers. This thesis makes use of the atmospheric delays, especially those in
107 the ionosphere, to investigate the dynamics within the ionosphere.

108 **1.2 GNSS for Ionospheric Studies**

109 Total Electron Content (TEC) signifies the number of electrons within a column of 1 m^2
110 along the signal path in the ionosphere and is expressed with TEC unit (TECU, 1 TECU equivalent
111 to 10^{16} electrons/ m^2). It is an integration of electron density, $n_e(s)$ along line-of-sight (LoS)
112 connecting the satellite with the ground receiver as shown in equation (1).

113

114
$$TEC = \int_{satellite}^{receiver} n_e(s) ds \quad (1)$$

115 TEC is a useful quantity to indicate the total amount of free electrons in the ionosphere. A
116 convenient way to measure TEC is to utilize GNSS data, using a technique called GNSS-TEC or
117 GPS-TEC. Further details of the ionosphere and the GPS-TEC technique will be explained later.
118 In comparison with conventional methods like ionosondes, GNSS-TEC method has much better
119 resolution both in space and time in regions where dense GNSS networks are available (Heki,
120 2021).

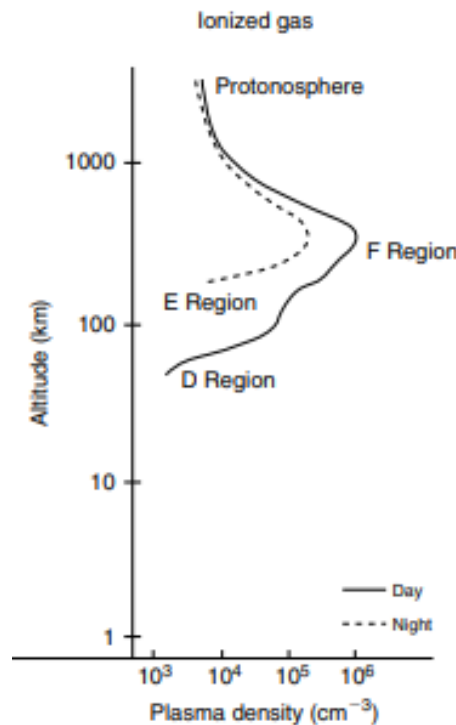
121 GNSS-TEC technique has been playing an important role in studying ionospheric
122 disturbances of space weather origin. Such disturbances include the large scale travelling
123 ionospheric disturbances (LSTID) and medium scale travelling ionospheric disturbances (MSTID)
124 in the mid-latitude region (e.g. Saito, 1998; Otsuka et al., 2011), as well as the sporadic-E,
125 extremely high electron density patches occurring in the E-region of the ionosphere (Muafiry and
126 Heki, 2018).

127 The GNSS-TEC method has enabled researcher to detect ionospheric disturbances
128 triggered by lithospheric phenomena. For example, those associated with large earthquakes are
129 known as the coseismic ionospheric disturbance (CID) (Calais and Minster, 1995; Heki and Ping,
130 2005; Cahyadi and Heki, 2015). Acoustic waves excited by coseismic vertical crustal movements
131 propagate upward and disturb the ionosphere as CID. I will further discuss this topic later in the
132 thesis. In addition earthquakes, Heki (2006) detected ionospheric disturbances excited by acoustic
133 waves by a 2004 Vulcanian volcanic explosion of the Asama volcano in central Japan. Kundu et

134 al. (2021) detected ionospheric disturbances caused by an artificial explosion in 2020 August in
135 Beirut, Lebanon.

136 1.3 Ionospheric Structure

137 Ionosphere is the uppermost layer of the earth's atmosphere where significant amounts of
138 neutral gasses are ionized due to solar radiation. Such photoionization produces electrons and
139 positive ions (Kelley, 2009). The ionosphere ranges in altitude from ~80 km up to several
140 hundreds of kilometers. They are divided into the D (~80 km), E (~100 km), and F (higher) regions.
141 The peak electron density occurs at altitude of ~300 km in the F-region (Kelley, 2009). During the
142 night, D and E regions become ambiguous, but they emerge again soon after sunrise.



143

144 **Figure 1.** Typical vertical profile of ionosphere (Kelley, 2009)

145 In 1931, Sydney Chapman, in USA, presented a mathematical model for the formation of
146 ionized layers based on the photoionization processes. He is the first who derived the distribution
147 of ionization as a function of height based on absorption of solar radiation. In Chapter 2.6, I
148 introduce his simple expression of electron production as functions of height and the solar zenith
149 angle. The Chapman function will be used in constraining the solution around zero in the 3D
150 tomography calculations in this study.

151 The existence of the ionosphere was recognized for the first time when radio waves are
152 realized to propagate over large distances. In 1882, Balfour Stewart in Scotland suggested the
153 existence of an ionized region in the atmosphere by measuring the variation of geomagnetic field
154 using a compass. In 1901, Guglielmo Marconi, Italy, sent radio waves from England to Canada
155 demonstrating that the ionosphere acted like a mirror for high frequency (HF) radio waves.

156 Ionosphere has been extensively utilized for long-distance radio communications using HF
157 radio waves, which are bounced back to ground and enable global-scale propagation. Higher
158 frequency (e.g. VHF) radio waves penetrate ionosphere and cannot be used for
159 telecommunications. Owing to the usefulness of the ionosphere for public, people have long been
160 monitoring ionosphere with various sensors including ionosondes, satellites, and radars.

161 I consider that recent discoveries of ionospheric disturbances related to large earthquakes
162 greatly enhanced the implication of the ionospheric studies. Among others, I pick up a recent topic
163 of ionospheric anomalies preceding large earthquakes. Considering a long unsuccessful history of
164 earthquake prediction, TEC changes immediately before large earthquakes found shortly after the
165 2011 Tohoku-oki earthquake by Heki (2011) could become a key phenomenon toward the

166 operation of practical earthquake prediction and mitigation of earthquake disasters in the future. I
167 will discuss the link between earthquakes and ionosphere in more detail in Chapter 1.6.

168 **1.4 Solid Earth and Ionosphere**

169 The lithosphere is the uppermost part of the solid earth from the surface (0 km altitude)
170 way down to the depth ~100 km. Lithosphere is divided into tectonic plates, which consist of
171 oceanic and continental plates. The asthenosphere below the lithosphere allows tectonic plates to
172 move around and interact with each other causing variety of phenomena along their boundaries.

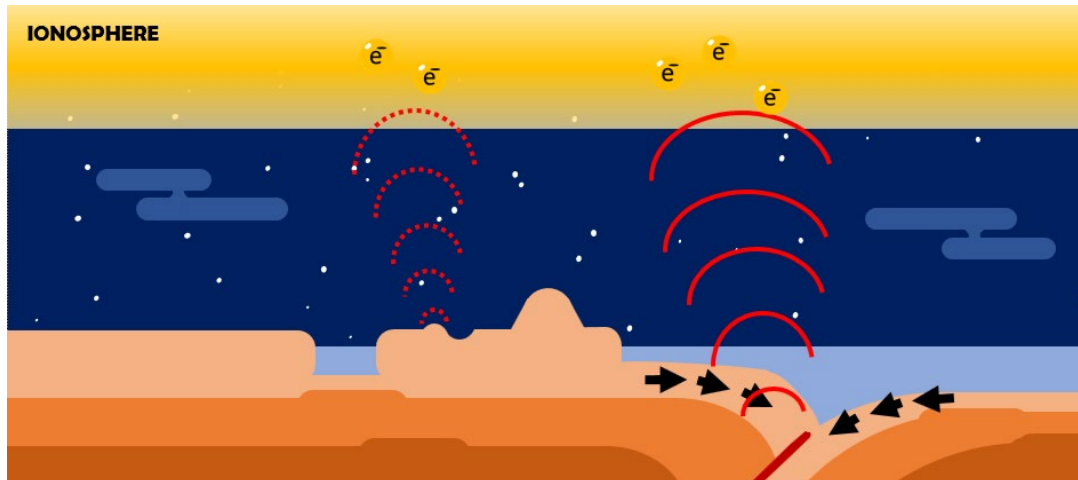
173 There are three types of plate boundaries. The first one is the divergent boundary, i.e., one
174 plate goes away from another plate due to extensional force acting along the boundary. Divergent
175 plate boundaries usually exist in the ocean floor as submarine mountain ranges, such as the Mid-
176 Atlantic Ridge and the East Pacific Rise. The second boundary is the convergent boundary, where
177 the plates collide with each other. Compressional forces between the two plates cause large
178 earthquakes along such convergent boundaries. Such boundaries include the Japan Trench off the
179 Pacific coast of NE Japan, and the Sumatra subduction zone running to the west of the Sumatra
180 Island. Plate convergence often causes mountain building, and an island arcs is formed at one side
181 of the convergent boundary. The last type is the translational plate boundary, where one plate
182 moves sideways along the plate boundary (transform faults). The San Andreas fault zone in the
183 western United States (US) is the typical plate boundary of this type.

184 Recently, solid earth was found to disturb the ionosphere in several different ways. For
185 example, vertical movement of the surface during an earthquake faulting excites acoustic waves
186 in the atmosphere. This wave propagates upward and reach the F-layer of the ionosphere and

187 makes a N-shaped pulse in TEC (Heki, 2021). This typically occurs ~10 minutes after the
188 earthquake and can be as early as ~8 minutes after earthquake (Astafyeva et al., 2011). This kind
189 of ionospheric anomaly is often called coseismic ionospheric disturbance (CID) and propagates
190 horizontally at the F region sound speed 0.8-1.0 km/s.

191 Since the first detection of CID with GNSS by Calais and Minster (1995), there have been
192 numbers of studies discussing the characteristics and underlying physics of CID. For example,
193 Heki and Ping (2005) showed that the directivity of CID is controlled by the geomagnetic field by
194 studying CID due to the 2003 Tokachi-oki earthquake, Hokkaido, for the first time using a dense
195 network of GNSS. Such a directivity arises because of the Lorentz force acting on the movement
196 of free electrons associated with the propagation of acoustic wave within neutral atmosphere in F-
197 region. In the mid-latitude region in the northern hemisphere, such particle motions become
198 perpendicular with the magnetic field at the northern side of the epicenter resulting in suppression
199 of electron oscillations to the north of the epicenter.

200 Astafyeva and Heki (2009) studied the diversity of the CID waveforms for earthquakes
201 with different focal mechanisms by studying the three large earthquakes 1994, 2006, and 2007
202 with different focal mechanisms in the Kuril Islands. They demonstrated that a normal fault
203 earthquake could give rise to CID starting with a negative change of TEC, in contrast to CID by
204 reverse fault earthquakes starting with positive changes. For these earthquakes, Astafyeva et al.
205 (2009) also identified the co-existence of two different kinds of acoustic waves, i.e., CID due to
206 direct acoustic waves from the epicenter, and those excited by vertical crustal movements
207 associated with the passage of the Rayleigh surface wave. The latter can be distinguished from the
208 former by the propagation speed (~4 km/s) much faster than the former.



209

210 **Figure 2.** The acoustic wave (red circular wave) excited by coseismic vertical crustal movement
 211 may propagate upward and disturb the ionosphere as CID. Surface Rayleigh wave triggers
 212 secondary acoustic wave (dashed red circular wave).

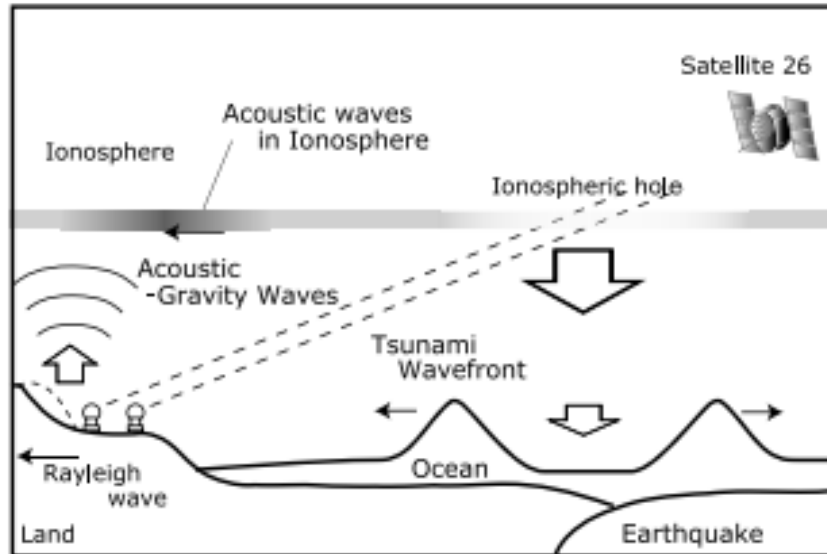
213

214 The CID by the Rayleigh surface waves has smaller geometric decay allowing the wave to
 215 reach farther distance propagation. Heki (2021) shows clear signatures of the Rayleigh wave
 216 generated by the 2004 M_w 9.2 Sumatra-Andaman earthquake in GEONET data in Japan ~40
 217 minutes after the main shock. This kind of ionospheric disturbances help us infer surface wave
 218 velocities in a region with limited number of seismometers.

219 **1.5 Ionospheric Disturbance due to the Sea Surface Motion**

220 Initial ocean motion generated by subduction zone earthquake causes acoustic disturbance
 221 in ionosphere. There, the electron motion constrained by geomagnetic field makes long-lasting
 222 electron depletion (formation of an ionospheric hole) above the tsunami source area (Kakinami et
 223 al., 2012; Shinagawa et al., 2013; Zettergren and Snively, 2019). Such an ionospheric hole shows
 224 TEC decrease right above the region of maximum uplift (due to the meter-scale downwelling of

225 the sea surface, Figure 3). The anomaly in the ionosphere starts right after the arrival of the acoustic
226 wave and stays above the rupture area with little migration.



227

228 **Figure 3.** The coupling between ionosphere and sea surface and formation of the ionospheric hole
229 after a large earthquake (Kakinami et al., 2012)

230

231 Rolland et al. (2010) found that the tsunami of the 2006 M_w 8.3 Kuril earthquake excited
232 internal gravity waves and subsequent ionospheric disturbances with amplitudes 0.15-0.50 TECU.
233 The tsunami waves generated by the 2004 M_w 9.2 Sumatran-Andaman earthquake also caused
234 similar disturbances in the upper atmosphere above the Hawaiian Islands (Liu et al., 2006). There,
235 the maximum peak-to-trough change was ~ 0.16 TECU. Such waves were also detected by
236 altimeters on board the Jason-1 and Topex/Poseidon satellites and yielded TEC changes of 0.2-0.6
237 TECU in 30 seconds (Occhipinti et al., 2006).

238 **1.6 Earthquake Precursors in Ionosphere**

239 Ionospheric precursors of large earthquake are divided into long-term and short-term
240 anomalies. The long-term precursors are detectable more than 1 day prior to the earthquake. Liu
241 et al. (2001) found anomalous diurnal variation of ionospheric TEC from GNSS observations
242 above the epicentral region of the 1999 Chi-chi earthquake ($M_w 7.7$), Taiwan. They showed that
243 the diurnal variation amplitude decreased three to four days before the earthquake. Based on the
244 analyses of many past earthquakes, Le et al. (2011) and Thomas et al. (2017) gave positive and
245 negative conclusions, respectively, on the statistical significance of such precursory changes. On
246 the other hand, the short-term anomaly first found by Heki (2011) occurs immediately before the
247 main shock. This is the phenomenon I discuss in this thesis. For both long- and short-term
248 anomalies, underlying physical mechanisms have remained ambiguous and controversial.

249 Searches for ionospheric anomalies related to large earthquakes involved satellites orbiting
250 the earth. Using the data from the DEMETER (Detection of Electro-Magnetic Emissions
251 Transmitted from Earthquake Regions) satellite launched by France, Němec et al. (2008) and Li
252 and Parrot (2013) reported statistically significant anomalies in lower ionospheric electron density
253 shortly before earthquakes. Newly launched China Seismo-Electromagnetic Satellite (CSES) has
254 been used to investigate the TEC precursors. Song et al. (2020) found anomalies several days
255 before the 2018 $M_w 6.4$ Lombok Earthquake. Adopting the moving median method (MMM) to the
256 electron density data, they found precursory electron density enhancements occurred 2-5 days
257 before this earthquake.

258 **1.7 3D Tomography for Ionospheric Electron Density Anomalies**

259 Computerized Tomography (CT) for ionospheric imaging has been developed over the last
260 three decades. It was started by Austen et al. (1988), who tried to demonstrate the feasibility of
261 CT to image ionospheric electron density distributions. He reconstructed two-dimensional (2D)
262 image of electron density using TEC data obtained along the path from the naval navigation
263 satellite systems (NNSS) toward several ground-based receivers. The results demonstrated that CT
264 can be applied to study the ionosphere.

265 In the last decade, tomographic approaches to the ionosphere has advanced owing to the
266 improved computation techniques and new data sets they used. For example, Tang et al. (2015)
267 presented clear images of the ionosphere in 3D during an ionospheric storm under high
268 geomagnetic activity. They utilized multiple observation techniques including radio-occultation,
269 satellite-borne altimetry, conventional ionosonde, and the GPS-TEC technique.

270 After that, another ionospheric 3D tomography study was reported by Chen et al. (2016).
271 There, they used only the GPS-TEC data to study the 3D spatial structure of MSTID. Taking
272 advantage of the dense network of the receivers, they could successfully reconstruct electron
273 density irregularities with 3D tomography. As another example, Garcia et al. (2005) imaged
274 coseismic ionospheric perturbation by the Denali earthquake using GPS-TEC data. Although the
275 anomaly was very large in space and GPS stations were not so dense, they could reveal the 3D
276 structure to a certain extent.

277 Investigation of the electron density distribution in ionosphere is crucial in understanding
278 physical mechanisms of ionospheric disturbances. The computerized ionospheric tomography is

279 an effective and promising approach to study 3D structures of ionospheric electron density,
280 particularly in the region where dense GNSS networks are available like the Japanese Islands
281 (Seemala et al., 2014; Chen et al., 2016; Saito et al., 2016).

282 **1.8 Research Objectives**

283 This thesis aims to map the ionospheric electron density anomalies related to large
284 earthquakes by using the 3D tomography method and TEC data sets from ground GNSS networks.
285 There are four specific ionospheric anomalies to be investigated here:

- 286 1. The ionospheric anomalies prior to the 2011 M_w 9.0 Tohoku-oki earthquake
- 287 2. The ionospheric anomalies prior to the 2010 M_w 8.8 Maule earthquake
- 288 3. The ionospheric anomalies after the 2011 Tohoku-oki earthquake
- 289 4. The ionospheric anomalies after the 2010 Maule earthquake

290 Then, I will discuss the differences in the preseismic ionospheric anomalies of the 3
291 different earthquakes, i.e. the 2011 M_w 9.0 Tohoku-oki and the 2010 M_w 8.8 Maule earthquakes
292 studied here, and the 2015 M_w 8.3 Illapel earthquake reported in He and Heki (2018). I finally
293 discuss physical mechanisms for the short-term precursory changes in ionosphere, based on the
294 3D tomography results obtained in this study.

295

296

297 **Chapter 2: Data and Method**

298 **2.1 GNSS Network in Japan**

299 Geospatial Information Authority of Japan (GSI) operates the nationwide dense GNSS-
300 network that covers the Japanese archipelago with ~1,300 stations with an average interval of ~20
301 km. This network is used to study crustal deformation and to serve as “electronic reference points”
302 in local geodetic surveys in Japan. This nationwide GNSS array is called GEONET (GNSS Earth
303 Observation Network). The raw observation data and daily coordinates of the GEONET station
304 are open to public on-line (terras.gsi.go.jp) in Japan. The raw data files in the receiver-independent
305 exchange (RINEX) format provide data with the 30 second sampling interval. In this study, I
306 downloaded the RINEX files from all the GEONET stations available for the studied dates.

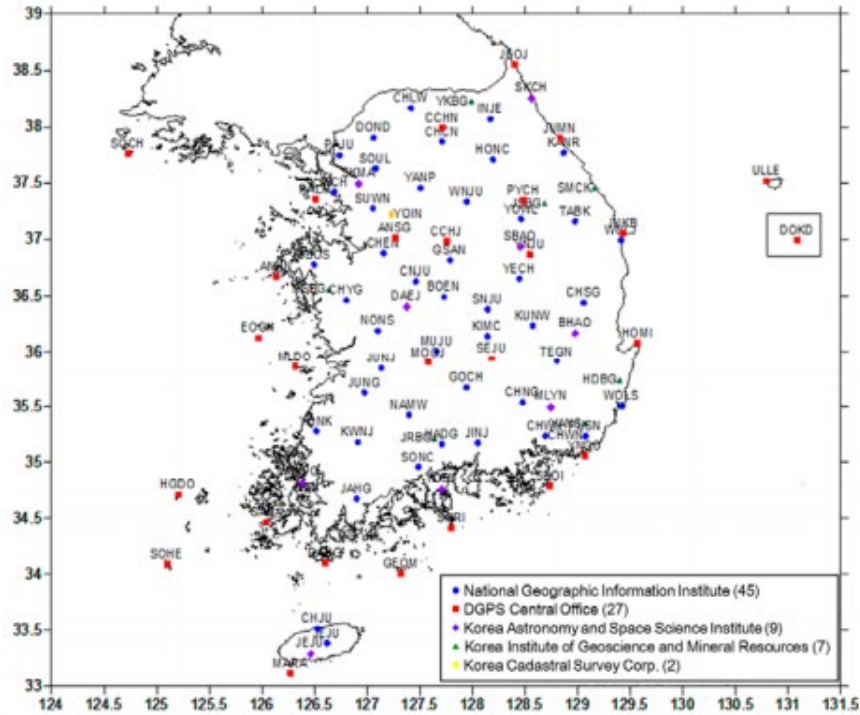


307

308 **Figure 4.** ~1,300 GEONET stations (red dots) are available in Japan (Tsuji and Hatanaka, 2018)

309 **2.2 GNSS Network in South Korea**

310 National Geographic Information Institute (NGII) of South Korea operates Korean GNSS
311 Network (KGN) that covers the South Korea with over 45 stations with separations of 20-50 km.
312 This network has been operated since March 1995 to investigate crustal deformation in the Korean
313 Peninsula and its vicinity and serves as the national datum for precise positioning system (Kwon,
314 2012). The raw GNSS data in the RINEX format files are recorded with the time interval of 30
315 seconds (Choi and Hong, 2019).



316

317

Figure 5. The dense GNSS network in South Korea (Kwon, 2012)

318

319

320

321

322

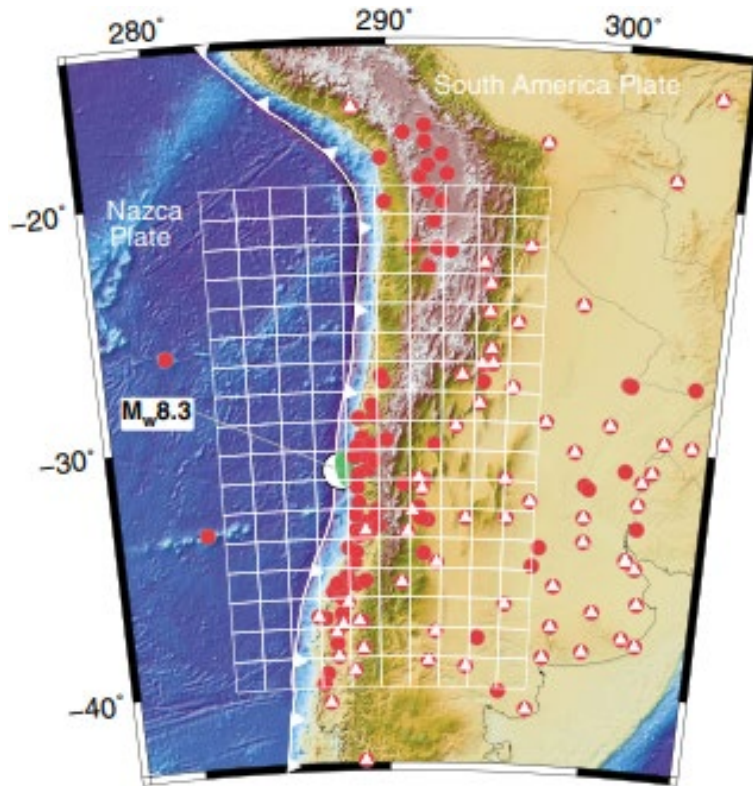
323

324

In this study, 53 stations of the Korean GNSS network are used for studying the ionospheric anomalies before and after the 2011 M_w 9.0 Tohoku-oki earthquake. Although the target of this study is ionosphere above the Tohoku region (far away from Korea), the availability of far-field station for this study is important to reinforce the spatial resolution of the 3D tomography of the ionosphere, especially in the western part of studied area.

325 **2.3 GNSS Networks in South America**

326 The RINEX data used in this study for South America are obtained from several different
327 organizations including the Centro Sismológico Nacional of Universidad de Chile, the Red
328 Argentina de Monitoreo Satelital Continuo (RAMSC) network of Instituto Geográfico Nacional
329 de Argentina (IGNA), the Rede Brasileira de Monitoramento Contínuo dos Sistemas GNSS
330 (RBMC) network of Instituto Brasileiro de Geografia e Estatística (IBGE), International GNSS
331 Service (www.igs.org), and University NAVSTAR Consortium (www.unavco.org).



332

333 **Figure 6.** 146 GNSS stations in South America used by He and Heki (2018) for 3D ionospheric
334 tomography of ionospheric anomalies before the 2015 Illapel earthquake.

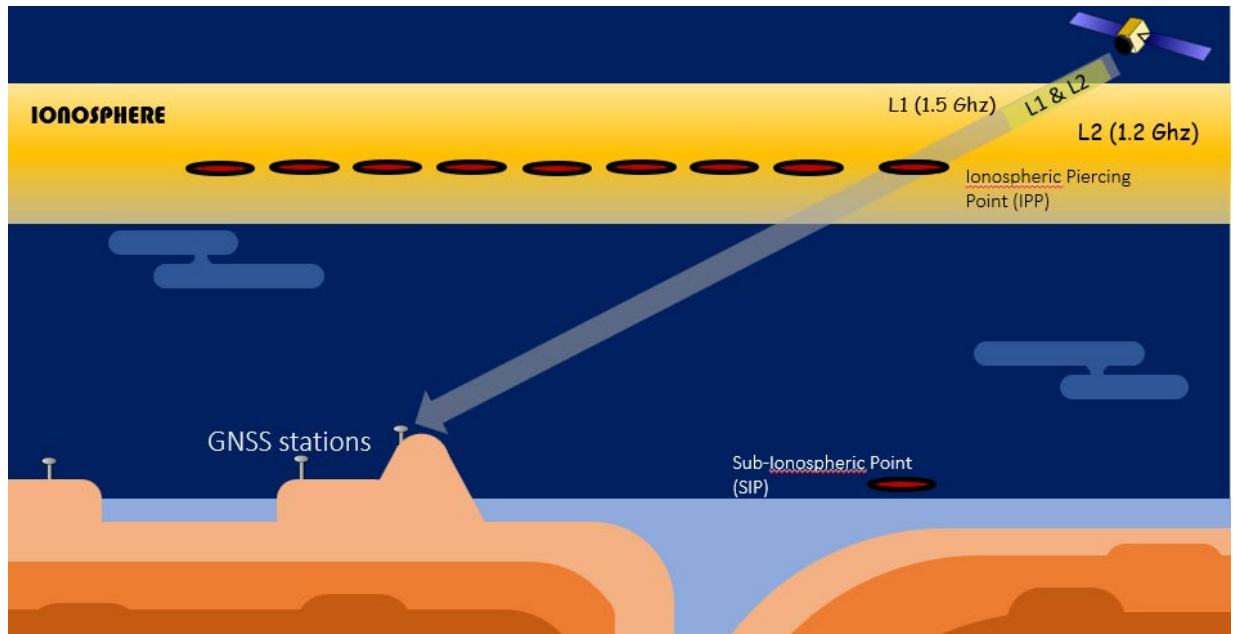
335 There are 146 GNSS stations in South America and 65 of them can track GLONASS as
336 well as GPS. These data are used to analyze the TEC changes before the 2015 M_w 8.3 Illapel, and
337 89 of those GNSS stations were used to study the 2010 M_w 8.8 Maule earthquakes.

338 **2.4 GNSS-TEC Method**

339 The slant TEC (STEC) is observed for a pair of GNSS satellite and receiver and
340 corresponds to the total number of electrons integrated along the line-of-sight (LoS). The STEC is
341 derived from the change in the phase differences ΔL_4 between the L1 and L2 microwave carrier
342 phases (expressed in length). In this study, equation (2) is used to convert L4 changes into STEC
343 changes:

$$344 \quad \Delta STEC = \left(\frac{1}{40.308} \right) f_1^2 f_2^2 / (f_1^2 - f_2^2) \Delta L_4 \quad (2)$$

345 There, f_1 (1575.42 MHz), f_2 (1227.6 MHz) are the frequencies of the two carrier waves (L1
346 and L2) in the L-band from GPS satellites, respectively (such frequencies are slightly different for
347 other GNSS). The phase difference of the two frequencies (ΔL_4) are often called the ionospheric
348 linear combination or geometry-free linear combination. The coefficient 40.308 is to convert
349 ionospheric delays into TEC in TEC unit (TECU, 10^{16} electrons/m²).



350

351 **Figure 7.** Illustration of L1 and L2 microwave signals propagating from GNSS satellites to GNSS
 352 receivers. IPP is the intersection of LoS with the hypothetical thin layer in ionosphere, and its
 353 ground projection is called SIP.

354

355 When GNSS satellites transmit microwave signals in both L1 and L2 frequencies, LoS will
 356 have an intersection point with the ionosphere. This intersection is called as ionospheric pierce
 357 point (IPP) and its projection onto the earth surface is named as sub-ionospheric point (SIP).
 358 Although the actual ionosphere is distributed over a wide range of altitudes, we assume a thin
 359 hypothetical layer at the height of largest electron density (~300 km) to calculate IPP and SIP
 360 coordinates, usually expressed with the geocentric cartesian coordinates fixed to the solid earth.
 361 There are 32 GPS satellites at this moment, and the number of satellites have been increasing
 362 drastically by the development of GNSS other than GPS. The increase of numbers of ground
 363 stations and GNSS satellites is important in the performance of the 3D tomography technique used
 364 in this study.

365 We need to remove the satellite and receiver inter-frequency biases (IFB) caused by
366 different electric path lengths of L1 and L2 circuits within satellites and receivers. For the
367 GEONET stations, such biases can be downloaded from Electric Navigation Research Institute
368 (ENRI) website (www.enri.go.jp) (Sakai, 2005). After correcting for these biases, we can convert
369 STEC to vertical TEC (VTEC) by multiplying them with the cosine of the incidence angle of LoS
370 to ionosphere. For the stations in South Korea and South America, the receiver biases are
371 determined by minimum scalloping method by Rideout and Coster (2006). In this method, a
372 receiver IFB of a certain station is obtained by minimizing the scatter of VTEC during a period
373 from midnight to dawn obtained with various satellites observed at that GNSS station. Satellite
374 IFBs are obtained from the header information of the Global Ionosphere Maps (GIM) downloaded
375 from University of Berne (aiub.unibe.ch/CODE).

376 I first isolated the absolute STEC by removing IFBs. Then, such STEC is converted to
377 VTEC by multiplying it with the cosine of the incident angles of LoS with a thin layer at 300 km
378 altitude. I use equation (3) to calculate VTEC:

$$379 \qquad \qquad \qquad \text{VTEC} = (\text{STEC} - d)\cos\theta, \qquad (3)$$

380 where θ and d represent the incidence angle of LoS at IPP altitude, and IFB (sum of satellite IFB
381 and receiver IFB) for this satellite-receiver pair, respectively. Such VTEC data do not contain
382 apparent U-shaped changes caused by elevation angle variations and are much easier to interpret
383 than STEC.

384 2.5 Strategies to Isolate Anomalies from GNSS-TEC Data

385 In this study, I use TEC changes obtained from the time series of VTEC. Anomalous
386 behavior of VTEC needs to be extracted from the observed data. Here I adopt the following two
387 types of strategies to isolate the ionospheric anomalies:

388 1. Modelling the temporal change of VTEC with a polynomial of time which is estimated
389 using the least-squares method. For example, if the polynomial degree is two, the model is
390 expressed by equation (4):

$$391 \text{VTEC}(t) = at^2 + bt + c, \quad (4)$$

392 where a , b , and c are parameters to be estimated using the least squares method. The
393 estimated models will serve as reference curves, and differences from these curves are
394 defined as the anomalies. There are two key factors we need to care when we obtain the
395 most appropriate models. First one is the choice of the polynomial degree. I use the L-curve
396 method to choose the best degree, i.e., I compare the root-mean-squares of the residuals
397 and employ the degree with which the residual showed a large drop (and insignificant drop
398 for higher degrees). Second factor is the start and the end of the exclusion time window to
399 avoid the leakage of the earthquake-related anomalies into the reference curves. Proper
400 selection of the windows is important to avoid artificial anomalies. I will discuss these two
401 factors in more detail in the next chapter.

402 2. Making the difference between medians of VTEC from two periods (before and after the
403 start of the anomalies). I use this method when it is difficult to estimate reference curves in
404 an objective manner. Further explanation to this topic will be discussed later.

405 In this study, I use the first strategy when I analyze preseismic ionospheric changes for the
406 2011 M_w 9.0 Tohoku-oki, 2015 M_w 8.3 Illapel, and the 2010 M_w 8.8 Maule earthquakes. On
407 the other hand, the second strategy is used to isolate the postseismic electron depletion of the
408 2011 M_w 9.0 Tohoku-oki earthquake. Each strategy is used to obtain ionospheric anomalies as
409 VTEC residuals. In this study, such VTEC residuals are converted back to STEC residuals and
410 are used as the input to the 3D tomography calculations.

411 **2.6 Ionospheric 3D Tomography Method**

412 The first step to perform 3D tomography is to set up voxels covering the studied region
413 and the target altitude range. The electron density anomaly within a block is assumed
414 homogeneous, and such anomalies are estimated for all the voxels. I employ different setting of
415 voxels for different earthquake cases considering the anticipated region of the anomaly signals and
416 the GNSS station distribution. Smaller voxels would result in a better spatial resolution of the
417 results. However, dense distribution of LoS penetrating the blocks is needed to make the
418 tomography results meaningful.

419 Thus, the second step is to collect as many LoS passing through the blocks as possible. If
420 the ground GNSS stations track multi-GNSS, i.e., not only GPS but also GLONASS, Galileo and
421 QZSS, such data should also be used as the input to the tomography. In fact, Muafiry et al. (2018)
422 used both GPS and GLONASS data to perform 3D tomography of sporadic E irregularities.

423 TEC anomaly of an LoS (y_i) from a certain satellite to a certain receiver is composed of
424 the sum of the products of the electron density anomalies (L_j for the j -th block) and the penetration
425 lengths (A_{ij}) for blocks located along the LoS as expressed by equation (5).

426
$$y_i = \sum_j A_{ij} L_j + e_i \quad (5)$$

427 There, e_i represents the measurement error of the i -th pair, and I assumed it as 0.05 TECU
 428 for all the measurements. This corresponds to a typical error for differential GNSS VTEC
 429 measurements (Coster et al., 2013). Equation (5) serves as the observation equation and the matrix
 430 A_{ij} becomes the Jacobian matrix.

431 First, I need to calculate the penetration lengths of LoS with voxels (A_{ij}) using simple
 432 geometric calculations. Generally speaking, one LoS has two (penetrated) or zero (not penetrated)
 433 intersection points with the surface of one voxel, and L_j is the distance between the entry point to
 434 the exit point for penetrated voxels. I use the GNSS station positions available in the header
 435 information of the RINEX files. The instantaneous satellite coordinates are calculated using the
 436 broadcast orbit information of the GNSS satellites. Then, the coordinates of the intersection points
 437 of LoS with the block surfaces can be calculated. Let x, y, z be the coordinate of points along a
 438 certain LoS, they can be expressed as follows:

439
$$x = x_a + \varepsilon (x_s - x_a) \quad (6)$$

440
$$y = y_a + \varepsilon (y_s - y_a) \quad (7)$$

441
$$z = z_a + \varepsilon (z_s - z_a) \quad (8)$$

442 where x_a, y_a, z_a represent the receiver coordinate x_s, y_s, z_s represent the satellite coordinate. The
 443 parameter, ε , changes over a range from zero to one ($0 < \varepsilon < 1$), i.e., (x, y, z) signify the receiver
 444 and satellite coordinates when ε is 0 and 1, respectively. Coordinates of points on the up-down,

445 east-west, and north-south surfaces of the block should satisfy the following three equations,
 446 respectively.

$$447 \quad x^2 + y^2 + z^2 = (R + H)^2 \quad (9)$$

$$448 \quad \frac{y}{x} = \mathbf{\tan} \varphi \quad (10)$$

$$449 \quad \frac{z^2}{(x^2+y^2)} = \mathbf{\tan}^2 \theta \quad (11)$$

450 There, R is the radius of the Earth at this latitude, H , φ , θ are the height, longitude and
 451 latitude of the horizontal, vertical (north-south), vertical (east-west) surfaces of a block. Here I
 452 assumed that the earth is a sphere without flattening. The coordinates of the LoS penetration points
 453 with these surfaces could be obtained by substituting x , y , z in (9)-(11) with those in (6)-(8), and
 454 solving for the parameter ε .

455 Now, the elements of the Jacobian matrix (A_{ij}) in equation (5) has been obtained, and I
 456 will proceed to estimate the set of parameters L_j to obtain the electron density anomalies within
 457 individual voxels. The observation equation (5) can be written in a matrix form as:

$$458 \quad \mathbf{y} = \mathbf{Ax} + \mathbf{e} \quad (12)$$

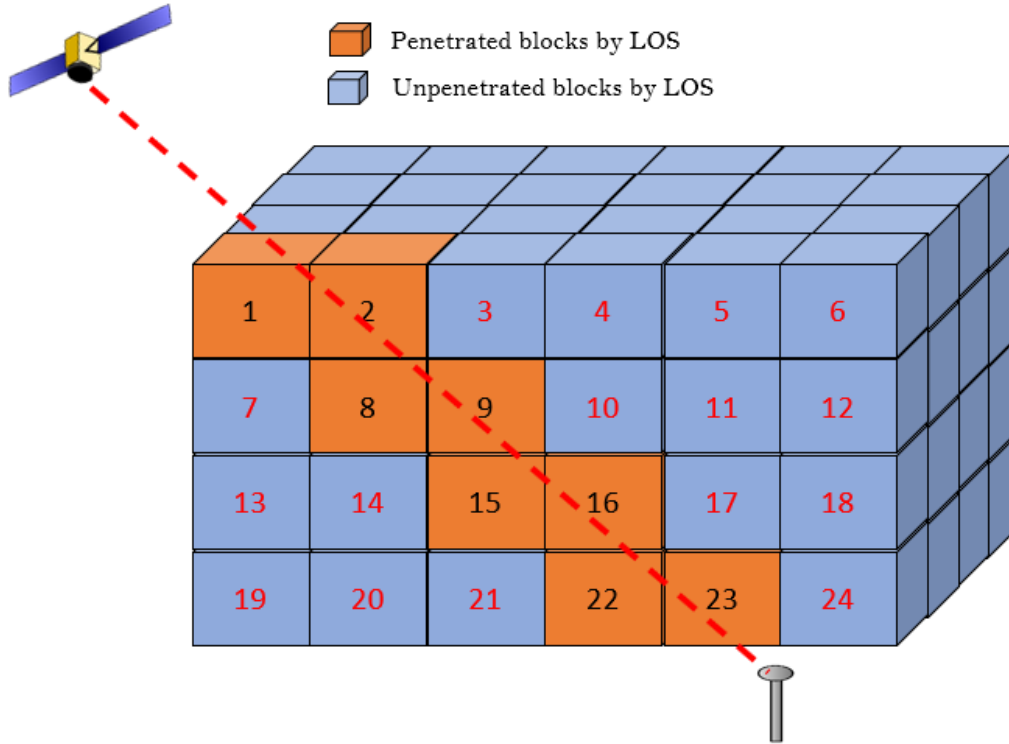
459 where \mathbf{y} is the vector composed of STEC anomalies y_i , \mathbf{A} is the Jacobian matrix composed of A_{ij} ,
 460 \mathbf{x} is the vector composed of unknown parameters x_j (electron density anomalies of individual
 461 blocks), and \mathbf{e} is the measurement errors. The vector \mathbf{x} is derived by solving the normal equation:

$$462 \quad \mathbf{x} = (\mathbf{A}^T \mathbf{A})^{-1} \mathbf{A}^T \mathbf{y} \quad (13)$$

463 after the Cholesky's decomposition, i.e., by decomposing the normal matrix $A^T A$ into lower
464 triangular matrix L and its transpose.

$$465 \quad \mathbf{A}^T \mathbf{A} = \mathbf{L} \mathbf{L}^T \quad (14)$$

466 Even if the LoS are densely distributed, they may not penetrate all the blocks, especially
467 above the oceanic and above areas without sufficient stations. Hence, certain constraints need to
468 be introduced to regularize the least-squares inversion. Here, a continuity constraint is used, i.e., it
469 is assumed that neighboring blocks have the same electron density anomalies with a certain
470 allowance for the difference. Suppose block number j is at the east side of block number i , then
471 assuming x_i and x_j , the electron density anomalies of these blocks, satisfy $x_i - x_j = 0$. One block
472 normally has six neighboring blocks (up, down, north, south, east, and south), and all these pairs
473 are added to the normal matrix as virtual observations (Nakagawa and Oyanagi, 1982). The block
474 pairs that are not juxtaposed is not constrained. I used the allowance for this constraint of $0.10 \times$
475 10^{11} el/m³ (this unit is equivalent to 1 TECU, or 10^{16} electrons/m², for penetration length of 100
476 km).



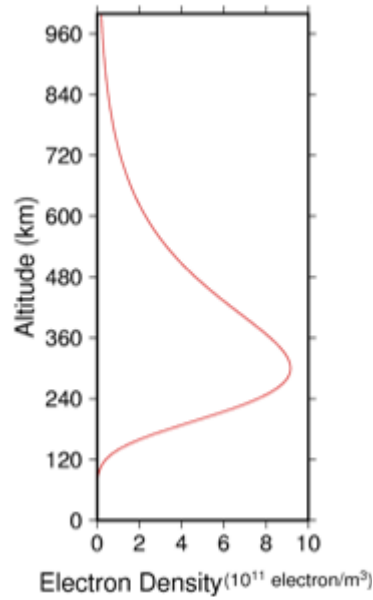
477

478 **Figure 8.** Illustration of blocks (voxels) in 3D tomography and penetration of LoS with a part of
 479 the blocks.

480

481 As an additional constraint, I weakly constrained the electron density anomalies around
 482 zero with an altitude-dependent allowance. According to the Chapman distribution, electron
 483 density at height h is proportional to $\exp(1 - A - e^{-A})/2$, where A equals to $(h - h_{\max})/H$. There, h_{\max}
 484 is the electron density peak altitude (300 km) and H is assumed 80 km. The allowance for this
 485 second constraint was assumed to be proportional to this distribution, and set as large as 1 % of
 486 the electron density at that altitude. This implies that I constrain the electron density strongly
 487 around zero for altitudes in the D and E regions, where electron density is lower, and weakly

488 around zero in the F region of the ionosphere, where electron density is higher. This is to avoid
489 estimation of unrealistically large electron density anomalies in very high or very low altitudes.



490

491 **Figure 9.** The Chapman functions showing altitude dependence of ionospheric electron densities.

492

493 **Chapter 3: 3D Tomography of the Ionospheric Anomalies immediately before**

494 **Earthquakes: The 2011 Tohoku-oki Earthquake**

495

496 *The content of this chapter was published in Journal Geophysical Research Space Physics, Muafiry, I.N.and K. Heki, 3D*

497 *tomography of the ionospheric anomalies immediately before and after the 2011 Tohoku-oki (M_w 9.0) earthquake, J. Geophys. Res.*

498 *Space Phys., 125, e2020JA027993, doi:10.1029/2020JA027993, 2020*

499

500 **3.1 Introduction: History of Debate**

501 Differential ionospheric delays (phase advances) of the two microwave carriers from
502 GNSS satellites enable us to study ionospheric TEC and its change in high temporal and spatial
503 resolutions. TEC data represents the number of electrons integrated along the LoS connecting
504 satellites and ground receivers. Vertical crustal movements associated with large earthquakes
505 trigger direct acoustic waves propagating upward. They reach the F-region of the ionosphere 8-10
506 minutes after earthquakes and disturb ionosphere causing changes in TEC.

507 Such a coseismic ionospheric disturbance (CID) has been first studied with GNSS by
508 Calais and Minster (1995) and with a dense GNSS network by Heki and Ping (2005). Later,
509 Astafyeva et al. (2011) studied immediate ionospheric response to the 2011 Tohoku-oki
510 earthquake, and Rolland et al. (2013) clarified mechanisms of several important properties such as
511 the CID directivity. Cahyadi and Heki (2015) proposed an empirical law connecting the earthquake
512 magnitude and the CID amplitudes, and Astafyeva and Shults (2019) explored the way to study
513 smaller earthquakes with CID. As reviewed in Heki (2021), the Japanese dense network GEONET
514 (GNSS Earth Observation Network) produces TEC data with high spatial (~20 km) and temporal
515 (30 s) resolution and contributed to our understanding of ionospheric disturbances related to
516 earthquakes.

517 Shortly after the 2011 March 11 Tohoku-oki ($M_w 9.0$) earthquake, Heki (2011) reported the
518 occurrence of positive (and partly negative) changes in TEC starting ~40 minutes before the
519 earthquake near the epicenter using GEONET. Heki (2011) also reported the occurrences of
520 similar anomalies before the 2004 Sumatra-Andaman ($M_w 9.2$), 2010 Maule ($M_w 8.8$), and the
521 1994 Hokkaido Toho-oki ($M_w 8.3$) earthquakes.

522 Then three papers published after that (Kamogawa and Kakinami, 2013; Utada and
523 Shimizu, 2014; Masci et al., 2015) doubted the reality of the TEC changes before the 2011 Tohoku-
524 oki earthquake. Coseismic acoustic disturbance makes not only short-term N-shaped TEC changes
525 but also airglow (Inchin et al., 2020) and long-lasting electron depletion in the ionosphere
526 (Kakinami et al., 2012; Shinagawa et al., 2013; Zettergren and Snively, 2019). In Heki (2011), the
527 TEC anomalies were defined as the departure from the reference curves. The major criticism by
528 these three papers is that the enhancement is an artefact that emerged by using the data after the
529 earthquake (including the long-lasting TEC drop) in defining the reference curves.

530 Rebuttals to those three papers have been published in the same journal (Heki and Enomoto,
531 2013; 2014; 2015). For example, Heki and Enomoto (2015) showed the reality of the positive
532 bending of TEC before earthquakes using the Akaike information criterion (AIC). They confirmed
533 statistical significance of the bending immediately before large earthquakes (e.g. 40 minutes before
534 the 2011 Tohoku-oki earthquake), demonstrating that such bending could be detected even without
535 using the data after earthquake occurrences. They further demonstrated that the leading times and
536 the intensities of the bending depend on M_w from seven large earthquakes with reasonable amount
537 of available GNSS data.

538 In a mean time, a new algorithm to detect such preseismic TEC changes was proposed by
539 focusing the spatial correlation of preseismic TEC data (Iwata and Umeno, 2016). This work,
540 together with Heki and Enomoto (2015), substantiate the existence of the preseismic anomalies.
541 Subsequently, He and Heki (2017) lowered the threshold of earthquake magnitudes and compiled
542 similar TEC enhancements prior to 18 earthquakes worldwide with M_w 7.3-9.2 and confirmed

543 systematic M_w dependence of preseismic ionospheric anomalies, i.e. the anomalies for earthquakes
544 of larger M_w start earlier and grow stronger (relative to background TEC).

545 The physical mechanism responsible for these preseismic signals is only partly understood.
546 Evidences obtained so far suggest it electromagnetic, assuming e.g. positive surface charges
547 responsible for the ionospheric electron redistribution. Mobile positive holes generated by the
548 breakage of the peroxy bonds that are ubiquitous in rocks (Freund, 2011) offer a scenario consistent
549 with the TEC observations. The holes are a quantum mechanical state and spread as fast as a few
550 hundreds of meters per second from seismogenic depths to the surface (Freund, 2013). Regarding
551 the ionospheric electron redistribution by surface charges, several mechanisms have been proposed,
552 e.g., Kuo et al. (2014) and Kelley et al. (2017). This issue will be discussed in detail later.

553 To understand the underlying physical process, it is effective to investigate the spatial
554 structure and temporal evolution of the preseismic electron density anomalies. Recently, He and
555 Heki (2018) studied the spatial structure of the electron density anomalies before the 2015 Illapel
556 earthquake, Chile (M_w 8.3), using 3D tomography technique. The result suggested that the
557 preseismic changes were composed of two parts, ionosphere electron density increase and decrease.
558 They emerged \sim 20 minutes before earthquake and are situated at lower and higher altitudes,
559 respectively, along the geomagnetic field. The same 3D tomography technique has been applied
560 for studies of 3D structures of electron density changes by the 2017 total eclipse in North America
561 (He et al., 2018) and sporadic-E irregularities in Japan (Muafiry et al., 2018).

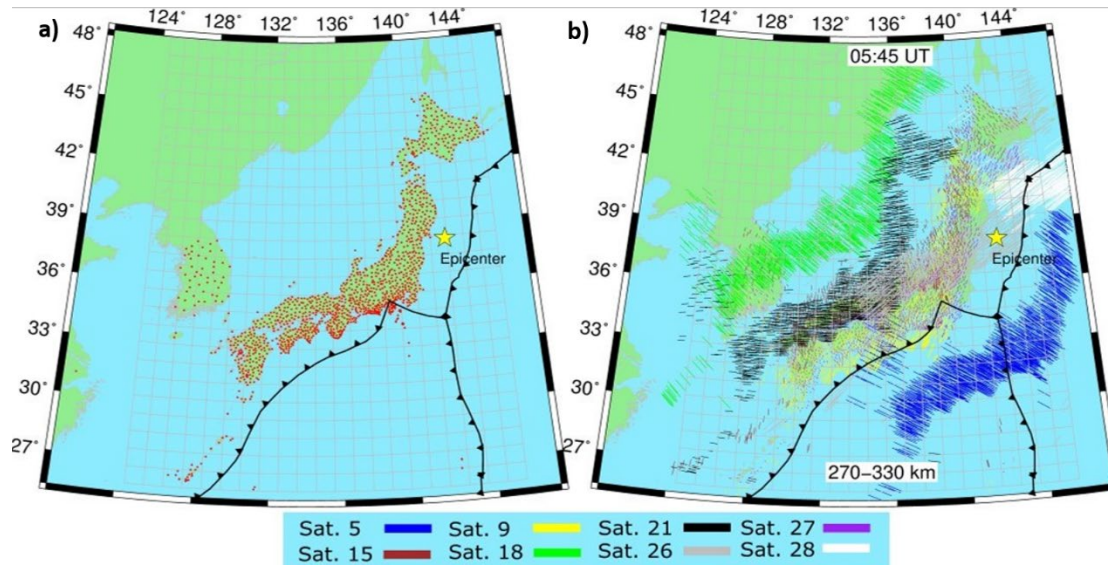
562 In this study, an improved version of the 3D tomography technique is applied to anomalies
563 immediately before the 2011 Tohoku-oki earthquake. The explanation about our 3D tomography

564 method is explained in detail in Chapter 2. Here, the anomaly signals are stronger than the 2015
565 Illapel earthquake and would help us better understand the 3D structure and the evolution of the
566 ionospheric electron density anomalies. The leading time of the preseismic anomaly of the 2011
567 earthquake is longer (~40 minutes) than the 2015 earthquake (~20 minutes). This makes us select
568 the objective procedure to isolate the TEC anomalies carefully, and this issue has been partly
569 discussed in Chapter 2 and will be discussed again later on. At the end of Chapter 3, a simple
570 mechanism to redistribute ionospheric electrons by surface charges is also proposed.

571

572 **3.2 Data set**

573 GNSS data from the entire GEONET is used, a dense array of continuous GNSS receiving
574 stations in Japan. I also add data from the GNSS network in South Korea, with 53 stations and ~40
575 km average separation (Choi and Hong, 2019), to reinforce the resolution in the western part of
576 the studied area. In total, I used 1,284 GNSS stations to study the preseismic anomalies of the 2011
577 Tohoku-oki earthquake (Figure 10a). I used 8 GPS satellites (PRN 05, 09, 15, 18, 21, 26, 27, 28)
578 visible from the studied region immediately before the mainshock (05:45 UT). Unfortunately,
579 GEONET did not track GNSS other than GPS in 2011. Other data set has been explained in detail
580 in Chapter 2.



581

582 **Figure 10.** Maps showing the GNSS station distribution (red dots) and the voxels for 3D
 583 tomography above Japan, the Sea of Japan, and the Eurasian Continent including the Korean
 584 Peninsula (a). Yellow star indicates the epicenter of the 2011 Tohoku-oki (M_w 9.0) Earthquake.
 585 Black curves illustrate boundaries between tectonic plates in and around the Japanese Islands. The
 586 short lines indicate the LoS of satellite-station pairs at the altitude 270-330 km (one layer of voxels)
 587 one minute before the earthquake (b). Color of the lines indicates satellite numbers.

588 3.3 Data Processing Strategy

589 As described in Chapter 2, the study of preseismic anomaly will be using reference curves
 590 to isolate the VTEC anomalies. This method has been often criticized by two reasons, (1)
 591 postseismic drops influence the reference curves and cause artificial enhancements, and (2) it is
 592 inappropriate to use the TEC data after the earthquake for earthquake prediction studies. As for
 593 (1), I avoid the influence of the postseismic drop by excluding the part of VTEC time series when
 594 SIP (the ground projection of the intersection of LoS with a thin layer at 300 km altitude) is above
 595 the focal area (see Figure 11 inset maps). Considering the mechanism of postseismic TEC drops
 596 by downward plasma transport and recombination (Kakinami et al., 2012; Shinagawa et al., 2013)
 597 and numerical simulation of its long-term behavior (Zettergren and Snively, 2019), it is unlikely

598 that the area of postseismic drop occurs in areas far from the focal area, and its influence can be
599 mostly avoided by excluding VTEC data with SIP overlapping the focal region. This will be
600 discussed again later in this section.

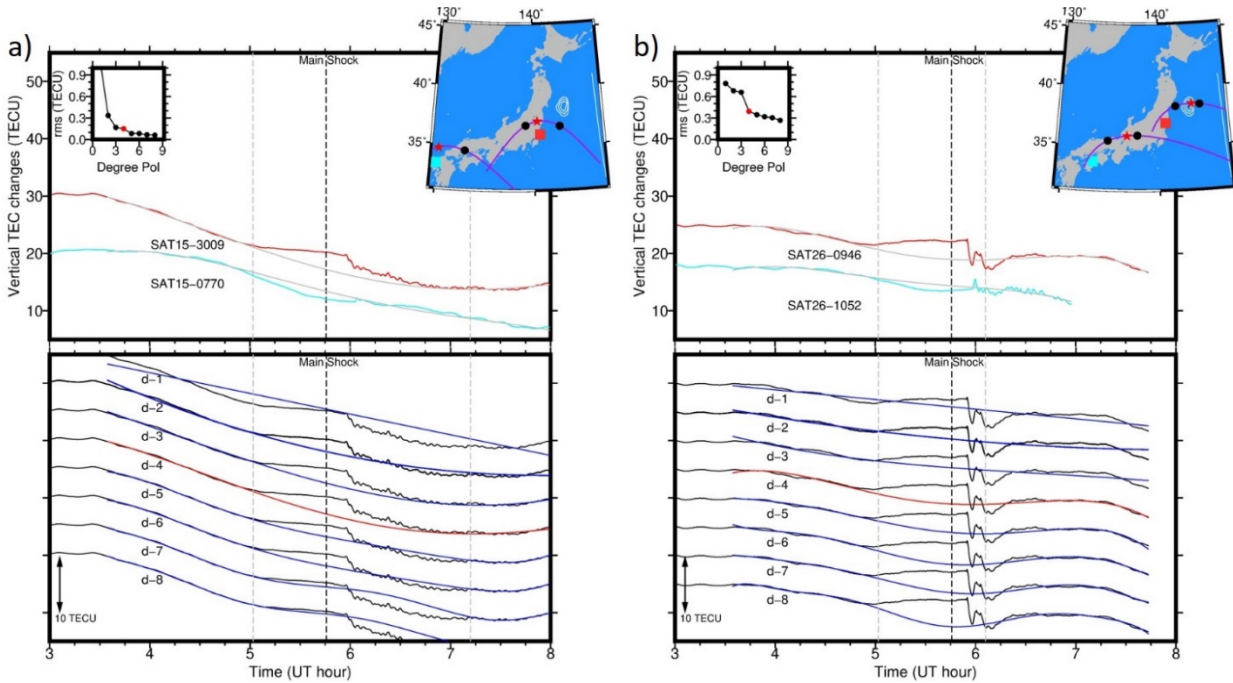
601 Regarding (2), a series of studies on this topic, from Heki (2011) to this thesis, do not aim
602 at practical earthquake prediction by observing GNSS-TEC in a near future. It would be more
603 important to answer the question if earthquakes know their final sizes when they start (i.e. the
604 question whether earthquakes are predictable or not) at this moment. From this point of view, the
605 reference curve method is appropriate to study preseismic signals because earthquakes would not
606 leave permanent changes (like coseismic steps in station coordinates) in TEC.

607 There are numbers of difference in the method to obtain the TEC anomalies from the early
608 study (Heki, 2011). Here I explain the three main differences, (1) input data, (2) selection of
609 exclusion windows, and (3) determination of polynomial degrees. For point (1), biased STEC is
610 converted to absolute VTEC beforehand and the reference curves are estimated to model the
611 absolute VTEC time series as explained in Chapter 2. This is different from Heki (2011), where
612 both polynomial coefficients and the bias are estimated simultaneously using STEC time series as
613 the input data. The new method enables us to model the time series using higher order polynomials
614 and to optimize the polynomial degrees using the L-curve method.

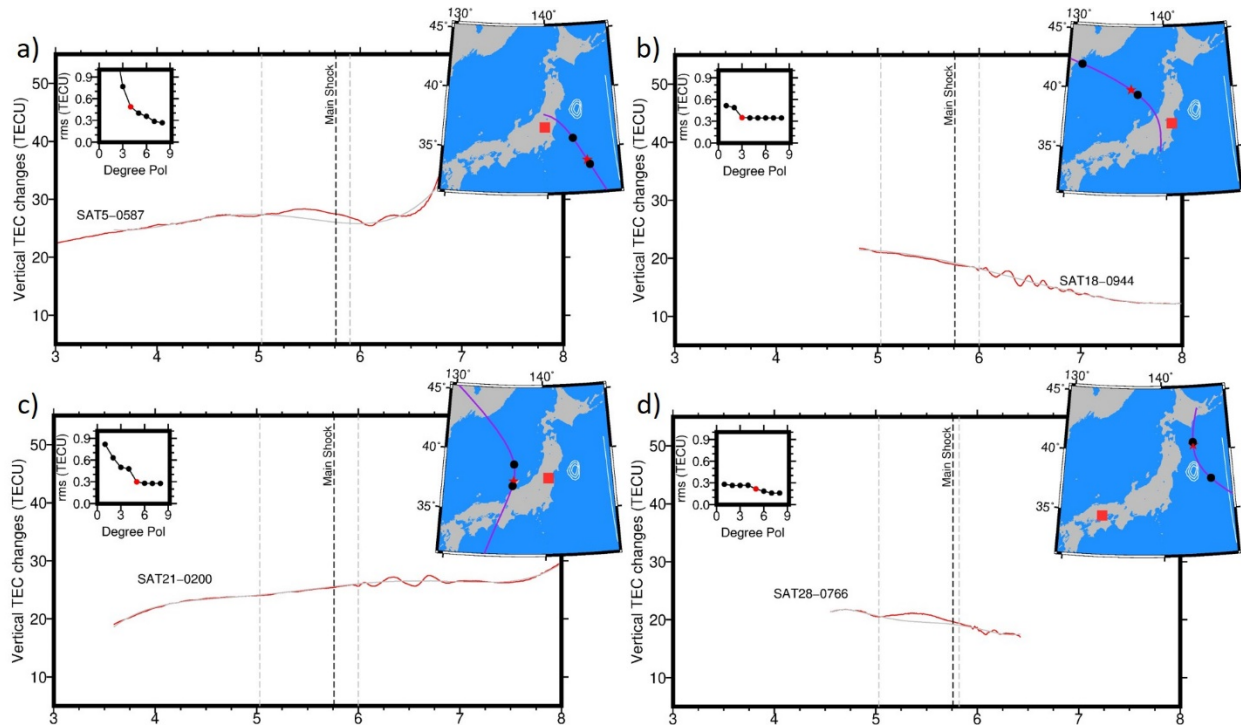
615 Another difference is that here I include the satellites that do not show significant
616 anomalies. For example, GPS Sat.18 was not studied in Heki (2011) because they showed little
617 TEC anomalies. However, such data are important to show where preseismic anomalies do “not”
618 emerge. After all, I used 8 GPS satellites including four new satellites 5, 18, 21, and 28 in addition

619 to 9, 15, 26, and 27 studied in Heki (2011). In Figure 12a-d, I show time series, similar to Figure
620 11, of four examples with these new satellites. There I fit the data with polynomials with degrees
621 determined by the L-curves in the insets. The geometry of the station position, satellite SIP track
622 (calculated assuming 300 km as the height of the thin ionosphere), and the epicenter are given in
623 inset maps. Satellites 18 (c) and 21 (d) do not show significant preseismic anomalies (only
624 coseismic acoustic disturbances) although the excluding windows are used in the polynomial
625 fitting. The data from Satellites 5 (a) and 28 (d) include weak preseismic anomalies together with
626 coseismic acoustic disturbances. These LoS do not penetrate the postseismic negative anomaly
627 and do not show postseismic TEC drops.

628



629
 630 **Figure 11.** Fitting reference curves of VTEC changes for satellite-receiver pairs of GPS Sat.15-
 631 3009 (a) and Sat.26-0946 (b) showing positive preseismic anomalies (upper panel, red curves). I
 632 also show two different pairs showing negative anomalies for comparison (upper panel, cyan
 633 curves). Vertical dashed lines indicate the exclusion window in fitting the model with polynomials.
 634 Red stars and black circles attached to the SIP tracks in the inset maps show the SIP positions at
 635 the main shock and at the start and end of the exclusion window (I assumed 300 km to calculate
 636 the SIP positions). Red and cyan rectangles indicate the locations of the two receivers. The maps
 637 also include the coseismic slip distribution drawn with the contours of 3-meters step (Ozawa et al.,
 638 2011). The L-curves in the left insets show the root-mean-square (rms) of the VTEC residuals
 639 obtained by fitting curves of various polynomial degrees. I employed the red curves in the lower
 640 panels, i.e. degree 4 for (a) and (b), that showed significant rms drops in the L-curves.



641

642 **Figure 12.** VTEC time series (red curves) and models with polynomials (grey curves) for satellite-
 643 receiver pairs with four newly used GPS satellites, i.e. Sat.5-0587 (a), Sat.18-0944 (b), Sat.21-
 644 0200 (c), and Sat.28-0766 (d). See the caption of Figure 11 for other symbols.

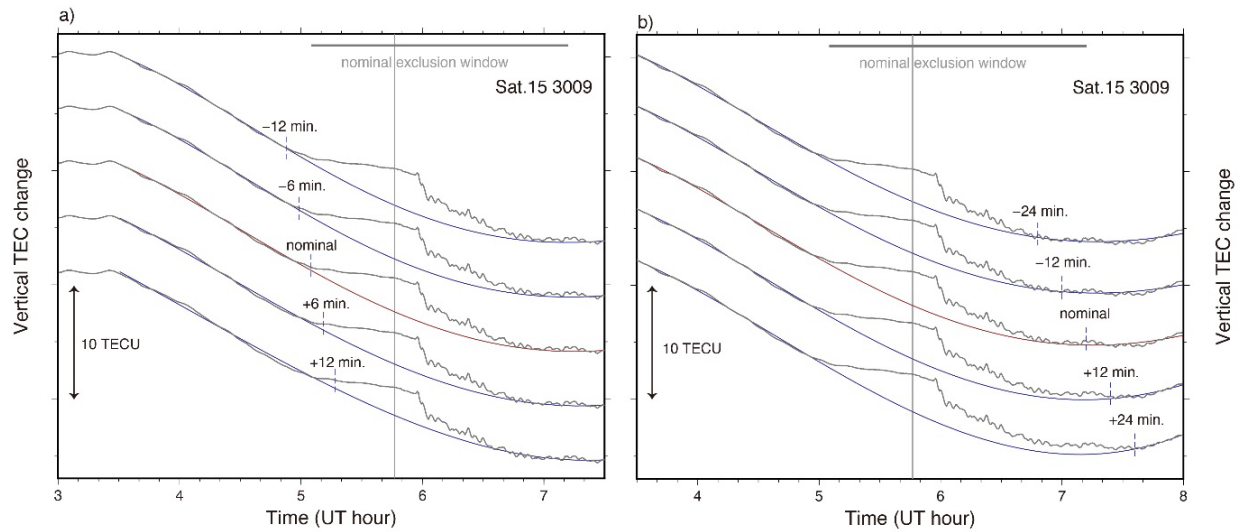
645

646 Regarding point (2), Heki (2011) excluded a time window 5.2-6.0 UT possibly influenced
 647 by the pre-, co-, and postseismic ionospheric disturbances in fitting the reference curves for all the
 648 four satellites. Here, I fit the polynomial to absolute VTEC using the excluding windows with the
 649 start and end times determined from external information. The selection of the end of this exclusion
 650 window is especially important because reference curves estimated using the period influenced by
 651 the long-lasting postseismic TEC drop may give rise to artificial preseismic TEC increase. In
 652 Figure 13, I demonstrate that the VTEC anomalies during the preseismic period 5:05-5:46 UT is
 653 not so sensitive to the excluding window settings using the case of Figure 2a.

654 For the start of the exclusion window, I employed the onset of the preseismic anomaly 5:05
655 UT for all the satellites (~40 minutes prior to the main shock). This time was obtained by Heki and
656 Enomoto (2015) by searching significant positive bending in VTEC time series using AIC. As
657 shown in Figure 13a, changing this starting time by ± 12 minutes does not make significant
658 differences in the reference curves for this pair of the satellite and the station.

659 Regarding the end time of the exclusion window, it is assumed that the postseismic drop
660 (ionospheric hole) occurs by coseismic vertical crustal movement and hence over the ruptured
661 fault. This will be confirmed later in Chapter 5 and supported by a numerical simulation, e.g.
662 Figure 4a of Zettergren and Snively (2019). I determined the end time of the exclusion window by
663 drawing the SIP trajectories to know the time for SIP to go out of the affected area (defined as the
664 area above the fault with slips exceeding 3 m). Naturally, the end times depend on satellites (see
665 Figure 11 inset maps). Table 1 lists the exclusion time windows for individual satellites used in
666 this study (windows depend on regions of the stations, too, for some satellites).

667



668

669 **Figure 13.** The numerical experiments to move the starting (a) and ending (b) times of the
 670 exclusion window in estimating the reference curves for the same data as in Figure 11a (station
 671 3009, satellite 15). In (a), the starting time is set to 4:53, 4:59, 5:05 (nominal), 5:11, and 5:17 UT,
 672 fixing the ending time to the nominal value (7:12UT). In (b) the ending time is set to 6:48, 7:00,
 673 7:12 (nominal), 7:24, and 7:36 UT, fixing the starting time to the nominal value (5:05 UT). The
 674 reference curve changes only slightly suggesting that the selection the excluding window is not a
 675 crucial factor to calculate the VTEC anomalies for this case.

676

677 **Table 1.** List of the exclusion time windows, and the polynomial degrees optimized by the L-curve
 678 method for individual satellites used in this study. Some satellites have 2 values for the polynomial
 679 degrees^{1,2} and the end of the exclusion windows^{3,4}, applied for 2 different areas in Japan.

680

681

682

683

684

685

686

687

688

689

690

691

692

GPS satellite number	Degree of polynomial	Start of the exclusion window (UT)	End of the exclusion window (UT)
5	4	5:05 (common)	5:54
9	5 ¹ and 7 ²		6:30
15	2 ¹ and 4 ²		7:12
18	3		6:00
21	5		6:00
26	4		6:06 ³ and 6:25 ⁴
27	5 ¹ and 2 ²		6:48
28	5		5:48

693 ¹for northern Hokkaido (north of 43.5N), ²for other parts, ³for stations east of 139.5E, ⁴for stations
 694 west of 139.5E

695

696 It should be noted that this study does not rely on the decay of the hole, which may last for
697 hours, but avoid the spatial overlap of the hole with the LoS. This procedure enables us to isolate
698 the VTEC anomalies caused by the earthquake robustly to a certain extent. Using the Figure 11a
699 case, Figure 13b demonstrates that moving the ending time of the exclusion window by 24 minutes
700 backward and forward let positive anomalies immediately before the earthquake change by only -
701 3.7% and +10.8%, respectively. This suggests that the uncertainty in the ending time of a few tens
702 of minutes is not crucial in isolating the preseismic VTEC anomalies.

703 For the satellites whose SIP does not go over the focal area (e.g. Sat. 18), I fixed the end
704 of the excluding window at 10 minutes after the earthquake. For a few satellites (e.g. Sat.5 and
705 Sat.28) with short postseismic VTEC data, I had to set up earlier end times for a part of stations
706 (e.g. 5 minutes after the earthquake). I did not set up a specific elevation cut-off angle and assumed
707 a thin layer at 300 km for STEC-VTEC conversion regardless of the elevations.

708 As for the point (3), the L-curve method is used to determine the optimum degree of
709 polynomials curve (see Figure 7 of He and Heki, 2017). Root-mean-squares (rms) is calculated
710 using the post-fit residuals outside the exclusion windows. Their dependences on the polynomial
711 degree are shown in the left insets of Figure 11. The lower-left edge of the L-curve is considered
712 to provide the most appropriate degree of polynomial to fit the VTEC changes. Table 1 also shows
713 the degrees of polynomials for different satellites employed here. In Figure 11, the total time span
714 of 5 hours is used for satellites 15 and 26 (the time spans are shorter for other satellites). The time
715 spans also influence the best polynomial degree, i.e. the best degree tends to be higher for a longer
716 time span. However, the shapes of the anomalies within the exclusion windows are not much
717 influenced by the total time spans.

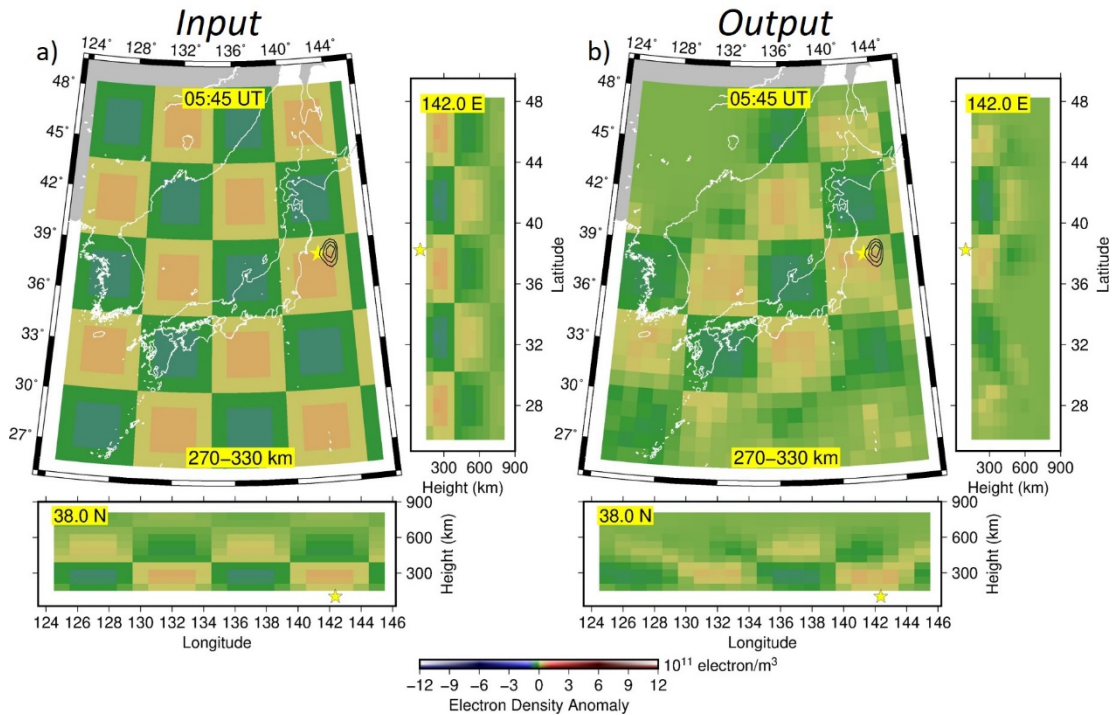
718 The departure from these reference curves (TEC anomalies) is used as the input for the 3D
719 tomography calculation. In doing so, the VTEC anomalies were converted back to the STEC
720 anomalies by dividing with cosine of the incidence angle of LoS to the 300 km layer. In short, I
721 took advantage of VTEC for its simplicity in fitting the reference curves (because the apparent
722 changes caused by elevation angle variations are already removed). However, the values after
723 converting to STEC anomalies are used for 3D tomography.

724 As emphasized in Heki and Enomoto (2013) and He and Heki (2016), preseismic TEC
725 anomalies take either positive or negative values. In Figure 11, I show examples of VTEC time-
726 series showing positive and negative preseismic TEC anomalies with red and cyan curves,
727 respectively. The difference would originate from the difference of the parts in ionosphere these
728 LoS penetrate, i.e. the former would have penetrated more positive parts than negative parts of the
729 electron density anomalies, and vice versa. The explanation on the variety of waveform of VTEC
730 in penetrated LoS will be discussed in Chapter 5.

731 **3.3 Resolution tests**

732 For the 2011 Tohoku-oki earthquake case, ~6,800 blocks are set up over the Japanese
733 Islands, the Sea of Japan, and the Korean Peninsula, with the size of 1.0° (east-west) \times 0.9° (north-
734 south) \times 60 km (vertical) for altitudes 90-870 km (Figure 10). Now the dataset (VTEC residual) is
735 ready, and the 3D tomography inversion could be performed to map the ionospheric electron
736 density anomalies before the earthquake using the method explained in Chapter 2. However, it is
737 often preferable to test the performance of the program and the resolution achieved by the available
738 data set beforehand, by applying the program to synthetic data. Such a test is important to discuss

739 if the block size is appropriate. It is also important to know in which region the inversion results
 740 have enough resolution. This depends on spatial distribution of available LoS, i.e., it is essential
 741 that multiple LoS penetrate certain areas to infer the electron density anomalies there.



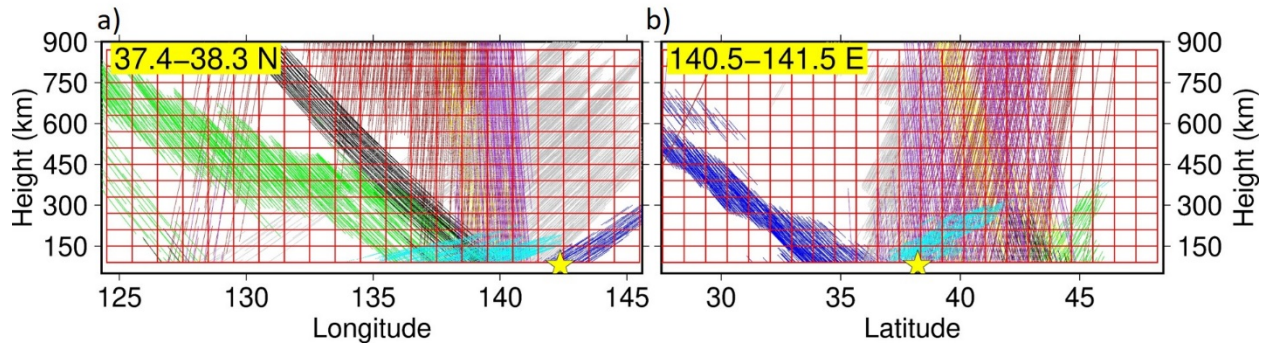
742
 743 **Figure 14.** The resolution test with the classical checkerboard pattern. The assumed electron
 744 density anomalies (a) and the output of the 3D tomography (b) are given in map view and north-
 745 south, east-west profiles.

746
 747 The accuracy of the 3D tomography can be assessed by performing the 3D tomographic
 748 inversion to recover artificial distribution of electron density anomalies using synthetic data. I first
 749 perform a test using the classical checkerboard pattern. I assumed the same satellite and station
 750 geometry as the epoch 05:45 UT on 2011 March 11, 1 minute before the Tohoku-oki earthquake,

751 to synthesize the input STEC data for the 3D tomography. In recovering the 3D distribution of
752 electron density anomalies, I applied the constraints explained in the previous chapter.

753 Figure 14a shows the assumed checkerboard pattern. It is composed of the electron density
754 anomalies of $\pm 2.00 \times 10^{11}$ el/m³. I let the anomaly change gradually between the positive and
755 negative parts to make the pattern consistent with the continuity constraint. I also assumed the
756 amplitudes of the anomalies to decay in very high and low altitude to make it compatible with the
757 constraint around zero with altitude-dependent tolerances, assumed proportional to the a-priori
758 electron density profile predicted by the Chapman distribution.

759 Figure 14b shows the recovered pattern for the blocks at the altitude range 270-330 km.
760 The pattern is well recovered particularly over the land (i.e. the Japanese Islands) and the offshore
761 area within ~200 km from the coast, including the area above the rupture. Similarly, in the vertical
762 section the resolution remains good in the altitudes 150-510 km, although the amplitudes of the
763 recovered anomalies are ~2/3 of the input model possibly originating from the constraint around
764 zero. On the other hand, resolution is poor where we do not have enough LoS penetrations (Figures
765 10b and Figure 15). Such regions include the Pacific Ocean to the south of the rupture and the
766 region above North Korea and Russia. The checkerboard-test generally shows a high performance
767 of our 3D tomography in the region of interest. As suggested by Figure 15, vertical resolution is
768 poor even above NE Japan for the highest layers of the blocks.

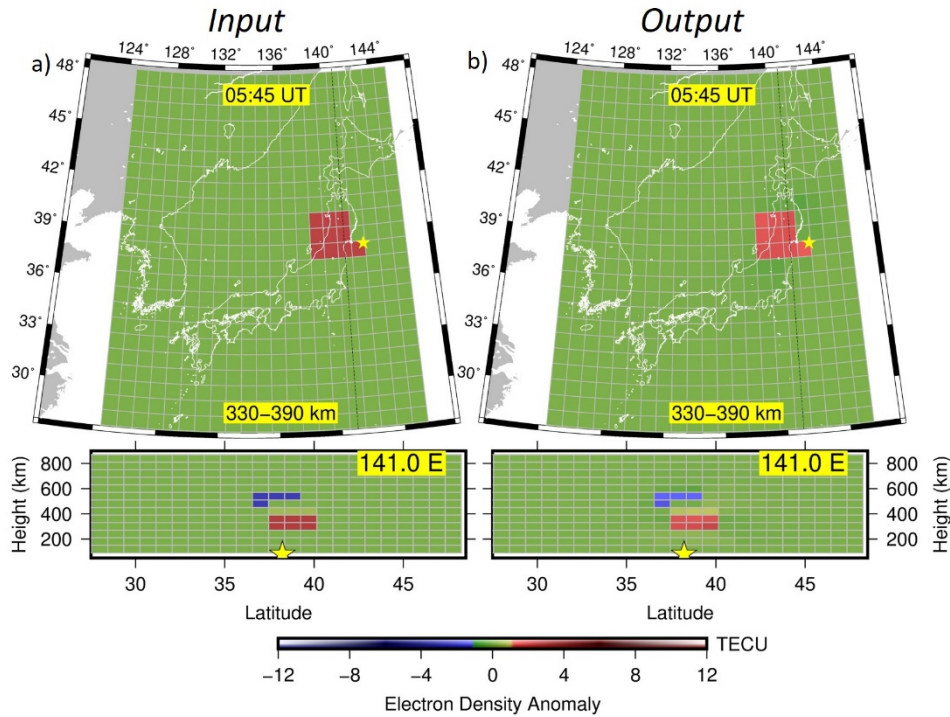


769

770 **Figure 15.** Vertical walls running east-west (a) and north-south (b) are assumed with the thickness
 771 of one block, and the LoS penetrating those walls are plotted with lines with colours corresponding
 772 to satellites (same colour as in Figure 10b, except for satellite 28 whose colour was changed into
 773 cyan for visual clarity). Electron density anomalies of voxels penetrated by many LoS with
 774 different angles are easier to be estimated than those penetrated by small number of LoS with
 775 similar directions.

776

777 I next assessed the robustness of our result for later discussions on preseismic electron
 778 density anomalies, by recovering patterns composed of a pair of positive and negative ($\pm 3.00 \times$
 779 10^{11} el/m^3) anomalies in low and high altitudes, respectively, in neutral background (Figure 16a).
 780 The results (Figure 16b) well reproduced the assumed pattern of the positive anomaly again
 781 reduced to $\sim 2/3$ amplitude of the input model due to the constraints. Similarly, the positive and
 782 negative anomaly patterns in the latitudinal profiles are well recovered with only weak smears in
 783 surrounding blocks not exceeding a few percent of the assumed anomaly. The results of the two
 784 resolution tests show that our 3D tomography results are accurate enough in the region of interest,
 785 where the TEC anomalies appeared immediately before and after the 2011 Tohoku-oki earthquake.



786

787 **Figure 16.** Second resolution test for a pair of compact positive and negative anomalies above NE
 788 Japan. The upper and bottom panels are horizontal view and latitudinal profile of the anomalies of
 789 the assumed pattern (a) and the output of the 3D tomography (b).

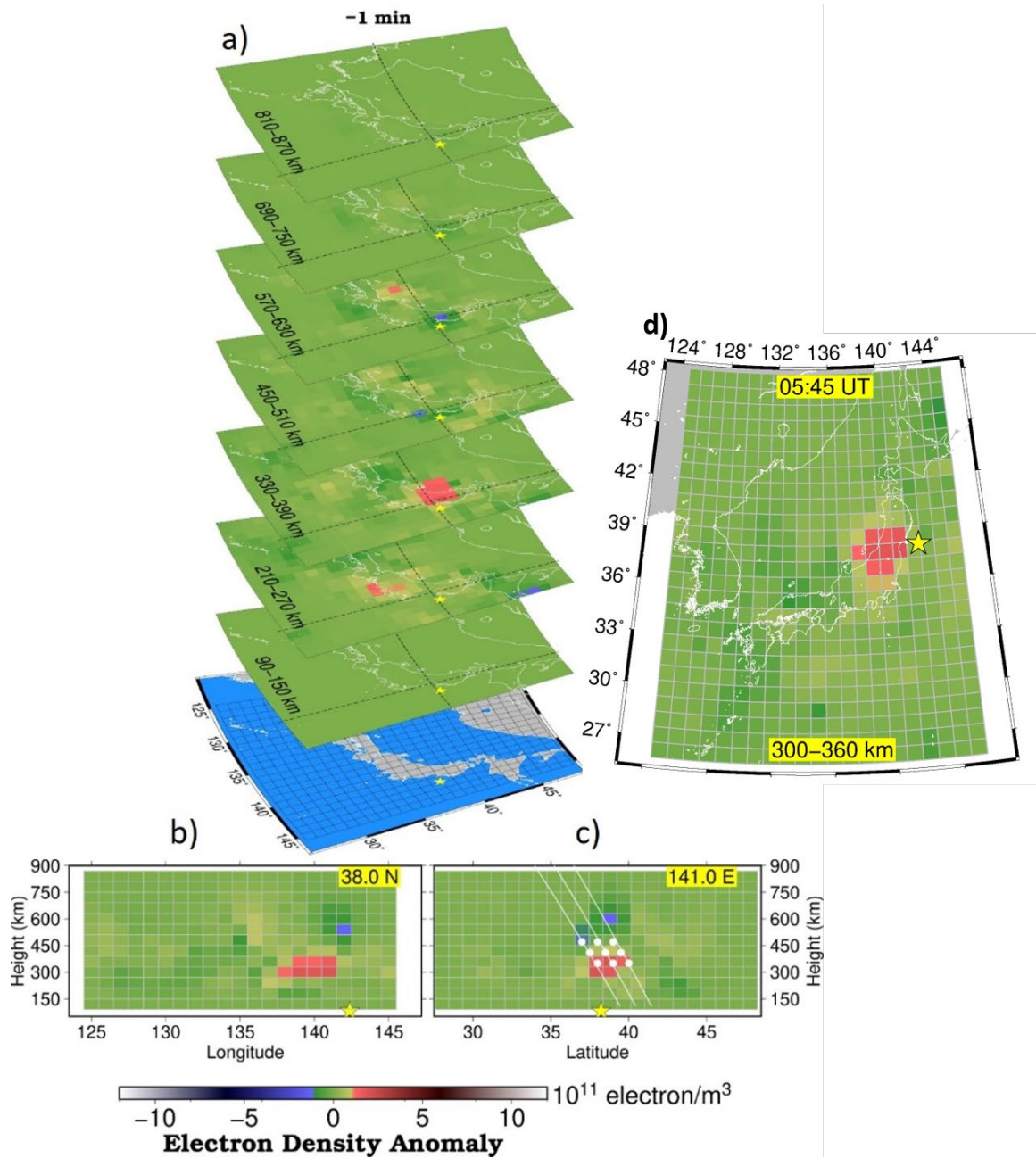
790

791 3.4 Tomography results

792 Figure 17a shows the map view of the 3D tomography result for altitudes of 90-870 km at
 793 05:45 UT, 1 minute before the 2011 Tohoku-oki earthquake, with longitudinal and latitudinal
 794 profiles. In Figure 18 I show the results at five epochs before the earthquake (40, 30, 20, 10, and
 795 1 minute before the earthquake). I confirmed beforehand by resolution tests that the performance
 796 of the tomography remains high for all these epochs. The results present that the strong positive
 797 electron density anomalies occurred at 270-330 km and 330-390 km altitude layers and the
 798 anomalies grow large without notable pattern change or spatial drifts toward the main shock. In

799 fact, the latitude of the voxel showing the largest positive anomaly stays around 38°N during the
800 40 minutes period.

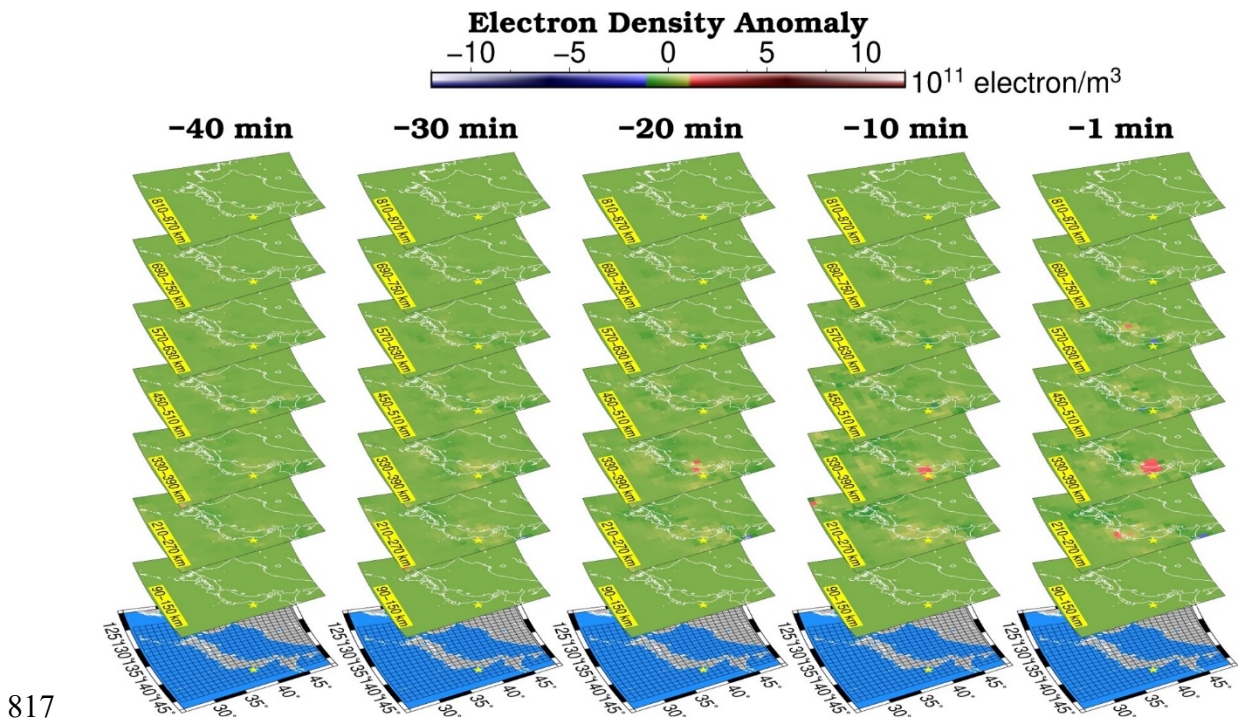
801



802

803 **Figure 17.** 3D tomography results of electron density anomalies 1 minute before the Tohoku-oki
 804 earthquake (a). The east-west and north-south profiles are also shown in (b) and (c), respectively.
 805 The white lines in (c) show the geomagnetic fields, and yellow stars show the latitude and
 806 longitude of the epicenter. White circles in (c) show selected positions used to draw Figure 22.
 807 The results for other epochs are given in Figure 18. An enlarged plan view showing positive
 808 electron density anomaly is given in (d).

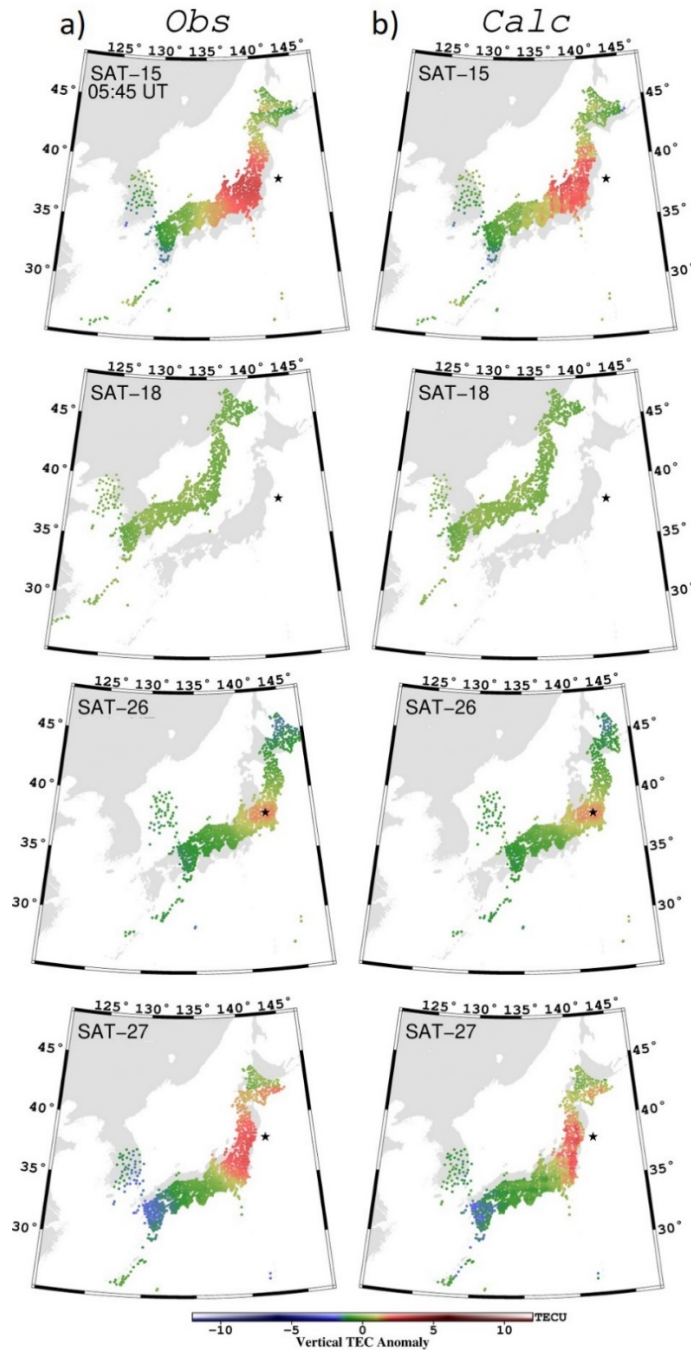
809 An important feature is that the positive anomaly lies above the land of NE Japan rather
 810 than right above the focal area (Figure 17d). Its implication will be discussed later. The
 811 longitudinal and latitudinal profiles (Figure 17b, c) show that the positive anomaly is the strongest
 812 at altitude 270-390 km. Above this positive anomaly lies the negative anomaly at altitude ~600
 813 km. These two anomalies are diffuse, and it is not very clear if they lie along the geomagnetic field.
 814 Nevertheless, the pattern resembles to the earlier report for the 3D structure of the preseismic
 815 anomalies of the 2015 Illapel earthquake (He and Heki, 2018), a pair of positive (height 150-225
 816 km) and negative (height 450-525 km) anomalies located along the geomagnetic field.



817
 818 **Figure 18.** 3D tomography results of electron density anomalies for altitudes 90-870 km at five
 819 epochs, 40, 30, 20, 10, and 1 minute before the 2011 Tohoku-oki earthquake.

820

821 Figure 19 compares the observed and calculated anomalies for four satellites, 15, 18, 26,
822 and 27, at the epoch 1 minute before the main shock. The “observed” anomalies (Figure 19a) are
823 those obtained as the departure from the reference curves to VTEC time series, and they are plotted
824 at their SIP. On the other hand, the “calculated” anomalies (Figure 19b) were derived as the sum
825 of the products of the estimated electron density anomalies (Figure 17) and the penetration lengths
826 of voxels along the LoS. Such calculated STEC anomalies are converted to VTEC for comparison
827 with the observed anomalies. These two are expected to nearly coincide if the 3D tomography
828 inversion is successful. We can see that the observed TEC anomalies are well reproduced by the
829 estimated 3D electron density anomalies shown in Figure 17.

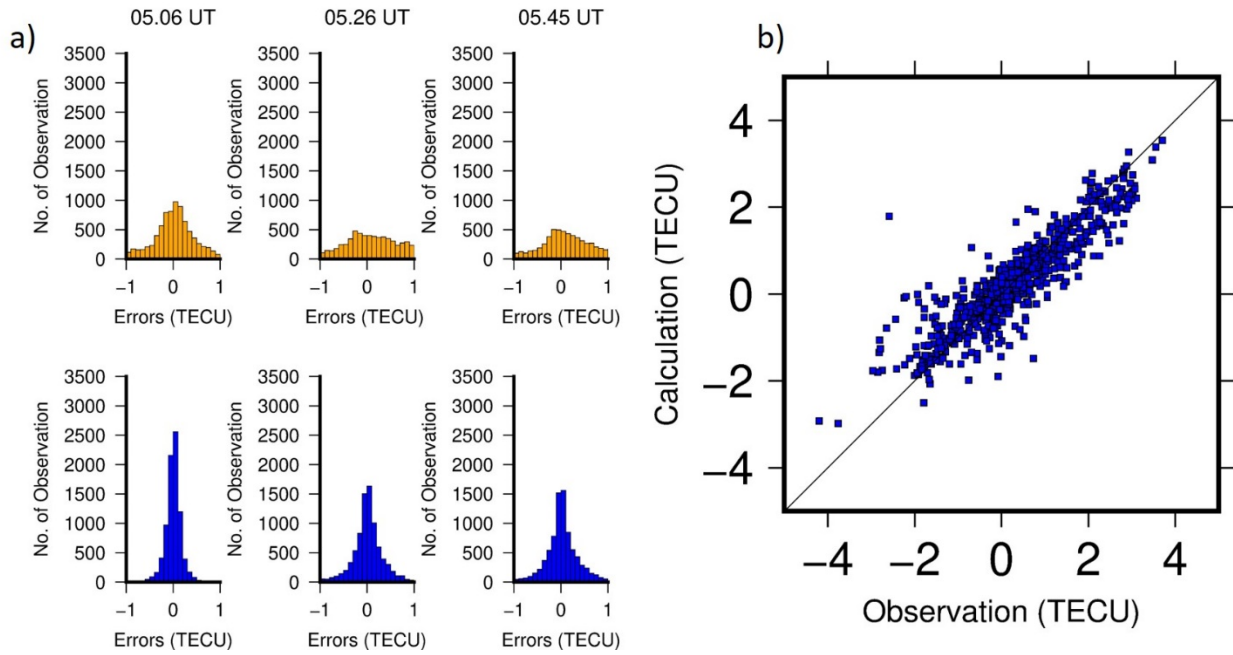


830

831 **Figure 19.** Comparison of the observed (a) and calculated (b) VTEC anomalies for 4 GPS satellites
 832 at the epoch at 05:45 UT, 1 minute before the earthquake. They are mostly consistent with each
 833 other showing that the estimated 3D electron density anomaly structure well explains the observed
 834 TEC changes.

835 Next, I perform two additional assessments of the accuracy; (1) confirming the reduction
836 of the variances of the original STEC anomalies to those of the post-fit residuals (the difference
837 between the calculated and the observed values compared in Fig.19), and (2) checking the
838 consistency of the subset data not used for 3D tomography with the result of the 3D tomography
839 estimated using the rest of the data. Figure 20a shows the results of (1) for three different time
840 epochs. Original STEC residuals have large variance around zero, but the post-fit STEC residuals
841 of the 3D tomography show much reduced scatter around zero. Together with Figure 19, this would
842 imply that the estimated 3D distribution of the electron density anomalies well explains the
843 observed STEC.

844 Figure 20b shows the result of a validation test for the epoch 05:45 UT. I removed
845 randomly selected 10% of the original input data as the validation data subset. Next, I used the
846 remaining 90% as the input to our 3D tomography method. Then, I calculated the STEC for the
847 removed 10% subset using the estimated 3D electron density anomaly distribution. They are
848 expected to coincide with each other. Figure 20b shows that the coincidence is as good as ~ 0.51
849 TECU.



850

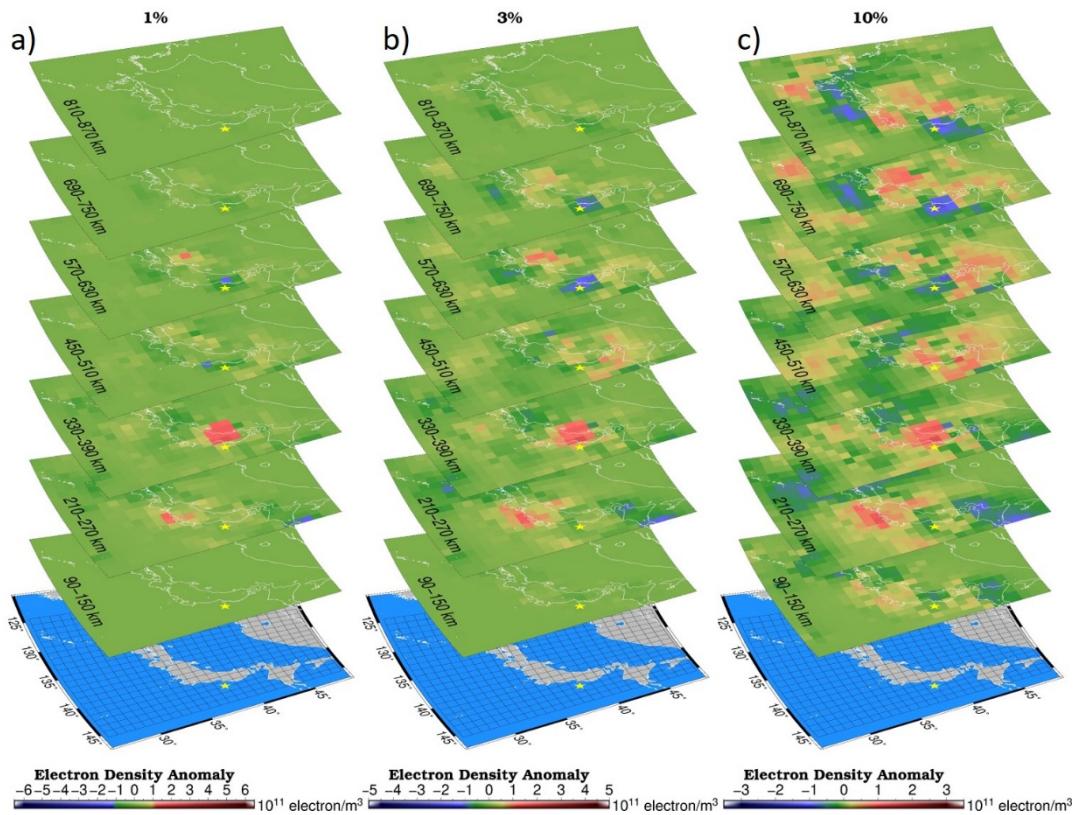
851 **Figure 20.** (a) The histograms of the STEC input to the 3D tomography (upper panel in orange),
 852 and the post-fit residuals (lower panel in blue) at three-time epochs (40 minutes, 20 minutes, and
 853 1 minute before earthquake). (b) Comparison between the randomly removed 10% subset of the
 854 observed STEC data at 05:45 UT (horizontal axis) and those calculated using the 3D electron
 855 density anomalies estimated with the remaining 90% data (vertical axis). The rms of the scatter
 856 around the 45 degrees line is ~ 0.51 TECU.

857

858 Figure 21 compares the tomography results based on three different settings of the
 859 constraint around zero, i.e., 1, 3, 10% of the Chapman distribution. It can be seen that the positive
 860 anomaly ~ 300 km high and negative anomaly ~ 600 km high persistently appear for those solutions.
 861 At the same time, a weaker constraint tends to yield complicated patterns in layers near the top of
 862 the blocks.

863 In Figure 15, I showed the distribution of the LoS connecting ground GNSS stations and
 864 the GPS satellites penetrating the vertical walls running east-west (a) and north-south (b) with the

865 one-block thickness. We can see that blocks with altitude up to 600 km above NE Japan are
866 penetrated by many LoS with multiple satellites having different penetration angles. On the other
867 hand, the highest layers are penetrated only by nearly vertical LoS, suggesting difficulty in
868 constraining altitudes of electron density anomalies there. I think that such irregular anomalies
869 emerging in the highest layers for weak constraint cases are not real.



870
871 **Figure 21.** 3D tomography results of electron density anomalies at the epoch 1 minute before the
872 mainshock with different strength of constraints around zero, i.e. 1 % (a), 3 % (b), and 10 % (c) of
873 the Chapman distribution of the electron density.

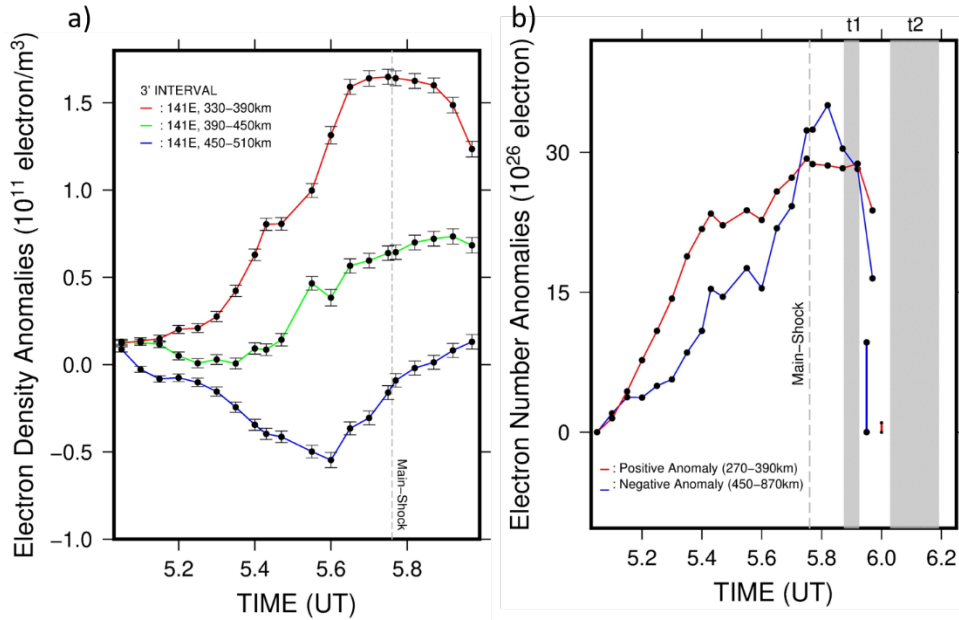
874

875 **3.5 Growth and polarity balances of the preseismic anomalies**

876 To further study the evolution of the electron density anomalies immediately before the
877 earthquake, in Figure 22a, I plot the electron density anomalies at points with three different
878 altitudes, 330-390 km, 390-450 km, and 450-510 km (white circles in Figure 17c) connected with
879 the geomagnetic field. The three altitudes correspond to the center of positive anomaly, middle
880 point between the positive and negative anomalies, and the center of negative anomaly,
881 respectively.

882 Figure 22a shows the averages of three blocks at low, medium, and high altitudes every 3
883 minutes before and after the earthquake. The positive anomalies show larger values than negative
884 anomalies. However, this does not necessarily mean the dominance of the spatially integrated
885 positive anomalies. Figure 22b indicates the total amount of positive and negative electron density
886 anomalies obtained by integrating them in space. They are well balanced, suggesting that the
887 growth of the anomalies occurred as the electron transport rather than net increase or decrease of
888 electrons.

889 The build-up of the positive and negative anomalies starts ~40 minutes before the
890 earthquake. They grow until ~20 minutes before the main shock and remain nearly constant until
891 the earthquake. After the earthquake, the anomalies remain stationary for ~10 minutes and start to
892 decay. I have no idea on the fluctuations of the curve around 5.4-5.6 UT and sudden increase of
893 the negative anomaly after 5.6 UT in Figure 22b. They may reflect a certain instability coming
894 from the VTEC observation errors. It should be noted that I did not perform in our tomography
895 any temporal smoothing which would be an effective remedy to reduce such instability.



896

897 **Figure 22.** (a) The evolution of the average estimated electron density anomalies of the three
 898 different blocks at the 3 altitudes, 360 km, 420 km, 480 km (see Fig.17c for positions), with 3-
 899 minutes interval. The error bars are the average of the formal errors of the 3 voxels sampled at the
 900 3 altitudes. (b) shows the integrated amount of positive and negative anomalies at lower (270-390
 901 km) and higher (450-870 km) altitude voxels, respectively. To the right side of (b), I show the
 902 spatially integrated increase in negative (blue) and positive (red) postseismic electron density
 903 anomalies measured as the difference between the two periods shown in grey squares (see Figure
 904 34 in Chapter 5).

905

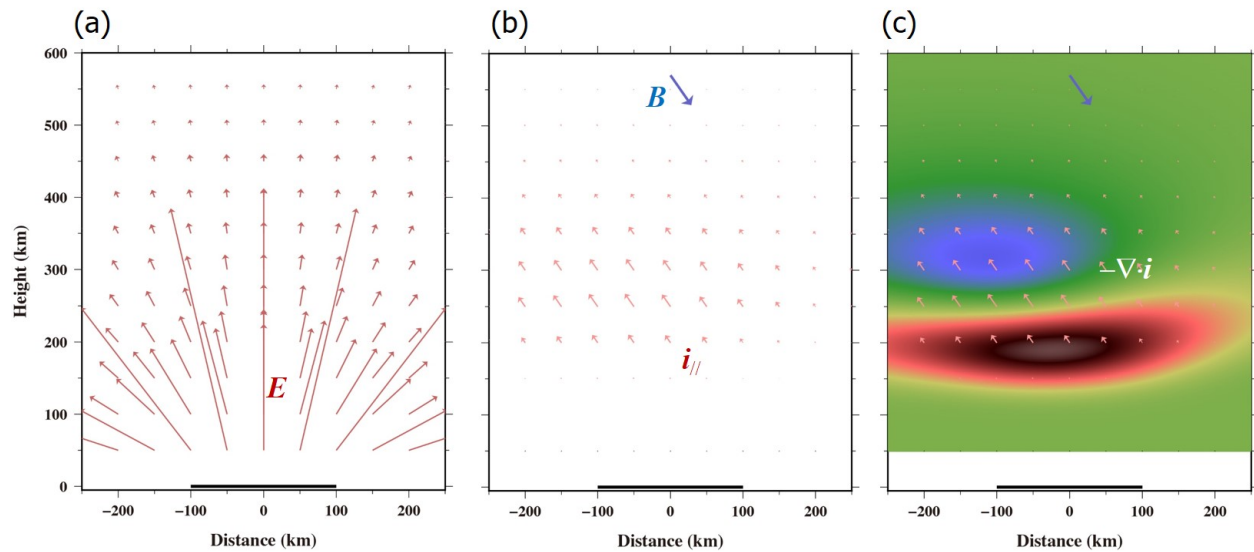
906 3.6 Discussion on the physical mechanism of the preseismic anomalies

907 The result showed that the total amounts of the positive and negative electron density
 908 anomalies increased in a similar manner (Figure 22b) suggesting little changes in the total number
 909 of electrons in the preseismic stage. Hence, such changes would have occurred without net increase
 910 or decrease of electrons, e.g., by electron transportation, rather than enhanced ionization
 911 (generation of new free electrons) or recombination (loss of free electrons).

912 Another important fact is that the strong positive anomalies before the 2011 earthquake
913 emerge only above land (Figure 17d). This suggests that the electron redistribution is due to electric
914 fields made by surface electric charges. Such surface charges would be relatively stable on land,
915 but they diffuse rapidly in the ocean due to high electric conductivity of sea water (areal density
916 of the surface charges would be determined by the balance between the production at depth and
917 the diffusion at the surface). Considering these features, I discuss possible physical mechanisms
918 connecting the surface electric charges to the preseismic ionospheric electron redistributions.

919 Two hypotheses have been proposed before to explain how surface electric charges
920 redistribute ionospheric electrons. Kuo et al. (2014) showed that the anomaly can be generated by
921 an upward electric current from stressed rock. This leads to the westward Hall electric field E .
922 This E , together with the geomagnetic field B , drives downward $E \times B$ drift of the ionospheric
923 plasma and makes a pair of positive and negative electron density anomalies. This model, however,
924 needs large electric fields near ground to let substantial electric current flow through the highly
925 resistive lower atmosphere. Kelley et al. (2017) proposed that the $E \times B$ drift could be driven
926 directly by electric fields made by surface electric charges. Their model needs the surface electric
927 fields only $\sim 1/500$ of the fair-weather field to produce the anomalies observed before the 2011
928 Tohoku-oki earthquake.

929



930

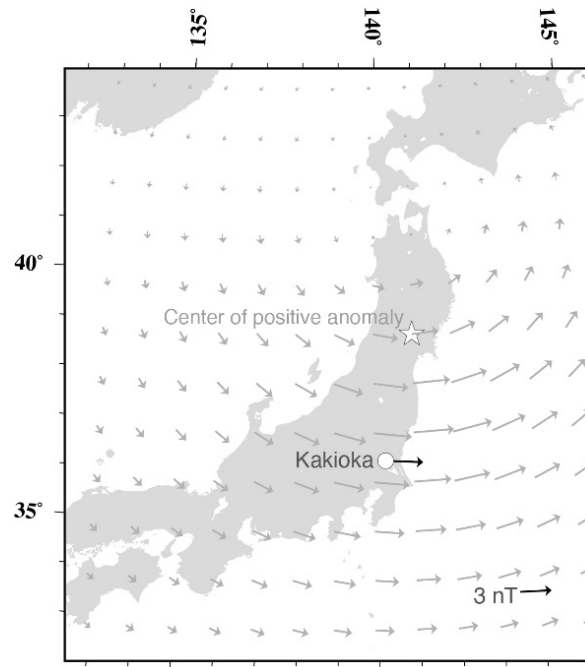
931 **Figure 23.** A two-dimensional image of the preseismic electron redistribution by surface electric
 932 charges. (a) Positive charges distributed on the surface (grey line at the bottom) make upward
 933 electric field E , and (b) the component parallel with the geomagnetic field B exerts electromotive
 934 forces and drives electric current $i_{//}$ along the geomagnetic field where there are enough free
 935 electrons. (c) Convergence and divergence of the electron flow makes positive (red) and negative
 936 (blue) electron density anomalies, respectively. This is a qualitative model, and scales to convert
 937 the illustrated quantities to real values are not given.

938

939 Muafiry and Heki (2020) proposed a new model focusing on the induced polarization, that
 940 would occur together with the process proposed by Kelley et al. (2017). Figure 23 qualitatively
 941 illustrates the idea. Electric fields E made by surface charges would reach the ionosphere (Figure
 942 23a). The field generates electromotive forces and makes electrons move along geomagnetic fields.
 943 If surface charges are positive, electron movements will be downward, and the current will be
 944 upward ($i_{//}$ in Figure 23b). The current will continue until the induced electric field cancels the
 945 external field made by surface charges, making the electric potential uniform along the magnetic
 946 field. The current will depend on the along- B component of the external electric field and the
 947 density of free electrons as a function of altitude. The non-uniform electric currents would result
 65

948 in convergence/divergence of electrons and make positive/negative electron density anomalies at
949 the lower/higher ionosphere along the magnetic field (Figure 23c), the structure found in Chile
950 (He and Heki, 2018) and in Japan (this thesis) by the 3D tomography.

951 The model is qualitative, and it is not supposed to give actual figures for quantities such as
952 areal density of surface charges and E . This stems from the limitation of the GNSS-TEC method,
953 i.e., GNSS can sense only electrons and cannot count positive ions. In fact, substantial amount of
954 positive ion would move together with electrons to keep the plasma “nearly” neutral (there should
955 be deviation from neutral, however, to cancel the external electric fields by the induced fields). In
956 short, the 3D tomography results do not allow us to directly infer E or i_{\parallel} .



957

958 **Figure 24.** Magnetic field on the surface caused by the upward current along geomagnetic field
959 above the star (the center of the positive anomaly), equivalent to cause ~ 0.15 of electron transport
960 given in Figure 7b from altitude 330 km to 600 km. This makes disturbing field of ~ 3 nT eastward
961 at the Kakioka station, consistent with those reported in Heki and Enomoto (2013).

962 One external test of the model might come from the magnetic fields possibly generated by
963 the upward current along B ($i_{//}$ in Figure 23b). Such a current would make eastward magnetic fields
964 on surface, mainly in the region to the south of the epicenter (Figure 24). As discussed above, the
965 electron density anomalies as revealed by 3D tomography (Figures 17) only reflect the electron
966 redistribution, and the net current would depend on the movements of positive ions. I drew Figure
967 24 assuming an arbitrary current, to let 4.5×10^{26} electrons (~ 0.15 of the amount in Figure 22b)
968 flow along a thin line extending from the center of positive electron density anomaly at 330 km
969 altitude upward along the magnetic field to 600 km altitude in 40 minutes. Then the Bio-Savard's
970 law predicts the eastward field of ~ 3 nT in the Kanto District (Figure 24). This nearly coincides
971 with the change in declination observed at the Kakioka observatory in Kanto (relative to Kanoya
972 in Kyushu) starting ~ 40 minutes before the earthquake as reported in Figure 4 of Heki and
973 Enomoto (2013). Anyway, the assumption is arbitrary (the value 0.15 does not have a theoretical
974 basis), and Figures 23 and 24 just provide a rough sketch illustrating how the induced polarization
975 occurs.

976 It is also assumed that the declination change at Kakioka (Heki and Enomoto, 2013) was
977 not a regular space weather phenomenon. It should be born in mind, however, that the 2011
978 Tohoku-oki earthquake occurred during a magnetic storm. So, a careful study is needed to attribute
979 the observed declination changes to the ionospheric electron redistribution process as proposed in
980 this study. It would be also important to detect magnetic field changes immediately before many
981 other large earthquakes to draw a more realistic picture of the whole process.

982

983 **Chapter 4: 3D Tomography of the Ionospheric Anomalies Before the 2010**
984 **Maule Earthquake, Chile: Comparison with the 2011 Tohoku-oki and 2015**
985 **Illapel Earthquake**
986

987 **4.1 Introduction: Structure of preseismic ionospheric anomalies**

988 In this chapter, the short-term preseismic ionospheric anomalies before the 2011 Tohoku-
989 oki earthquake is compare with other earthquakes for the sake of better understanding of their
990 features. So far, we studied examples of the 3D distributions of ionospheric electron density
991 anomalies immediately before two large earthquakes, i.e. 2011 Tohoku-oki (M_w 9.0, this thesis)
992 and 2015 Illapel earthquake, central Chile (M_w 8.3, He and Heki, 2018). Both cases show a
993 common structure, lower positive and higher negative electron density anomalies. Their vertical
994 profiles suggest that the altitudes of the positive and negative anomalies before the 2011
995 earthquake (\sim 300 and \sim 600 km) are somewhat higher than those of the 2015 earthquake (\sim 200 and
996 \sim 500 km).

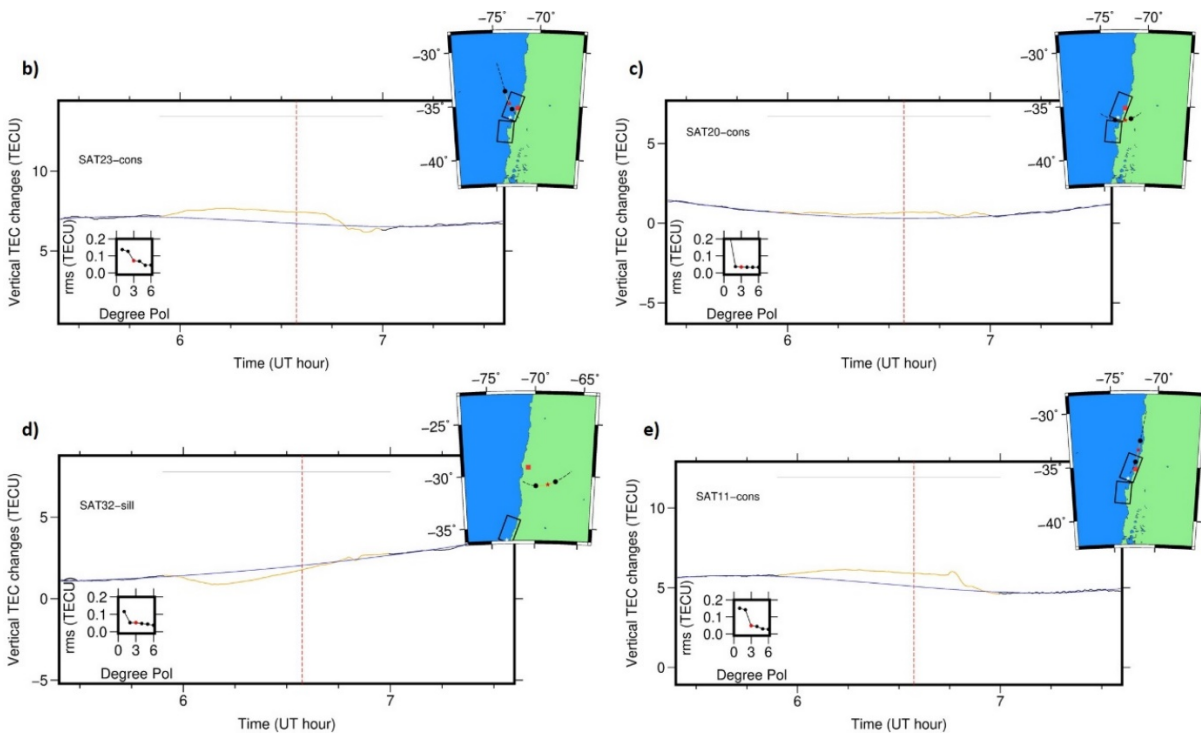
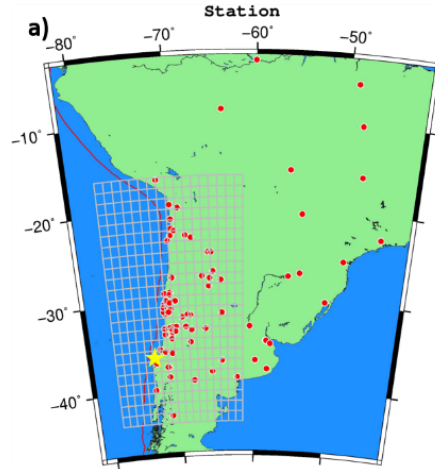
997 On the other hand, horizontal extents of anomalies are little different in the two cases, i.e.
998 the positive anomalies of 2011 lie within circles with diameter of \sim 300 km above the land region
999 and not above the epicenter (off-shore). This strongly supports the physical model presented in the
1000 previous chapter that electric charges on the land surface redistributed ionospheric electrons.
1001 Regarding the 2015 Illapel earthquake, its epicenter is close to the coast, and such a feature, e.g.
1002 lack of the anomaly above the ocean, is not clear.

1003 In this chapter, I analyze the 3D structure of the preseismic ionospheric anomaly of the
1004 2010 M_w 8.8 Maule earthquake, another M9-class earthquake occurred in central Chile \sim 1 year
1005 before the 2011 Tohoku-oki earthquake. I follow the same 3D tomography approach employed in
1006 He and Heki (2018) and this thesis.

1007 **4.2 Data set**

1008 In the morning (03:34 in local time) of 27 February 2010, a Mw8.8 earthquake ruptured
1009 the Topocalma, Carranza, and Arauco segments of the Chilean subduction zone (Jara-Munoz et
1010 al., 2015). The epicenter of this Maule earthquake is located at the geographic latitude of 35.9°S
1011 (geomagnetic latitude of 36.1°S), and He and Heki (2016) reported that the geomagnetic activity
1012 was low before and after this earthquake. Here I use the GNSS-TEC data extracted from raw
1013 RINEX data files obtained at 89 permanent GNSS stations in South America (Figure 25). The
1014 TEC data from six GPS satellites (11, 13, 17, 20, 23 and 32) are used. The spatial coverage of
1015 the GNSS stations is not so good as in the 2015 Illapel earthquake case (He and Heki, 2018)
1016 because many of the stations used there were not operating in 2010. The station density is much
1017 lower than the 2011 Tohoku-oki case (this thesis).

1018



1019

1020 **Figure 25.** Maps showing the GNSS station distribution (red dots) and the voxels for 3D
 1021 tomography above the middle South-America (a). Yellow star indicates the epicenter of the 2010
 1022 Maule ($M_w 8.8$) Earthquake. A red curve illustrates the Peru-Chile Trench, the boundary between
 1023 the Nazca and the South American Plates. Panels (b-e) show VTEC time series (yellow curves)
 1024 and reference curves by best-fit polynomials (blue curves) for satellite-receiver pairs with four
 1025 GPS satellites, i.e. Sat.23-CONS (b), Sat.20-CONS (c), Sat.32-SILL (d), and Sat.11-CONS (e).
 1026 Insets of (b-e) show the behaviour of the residuals for the change of the polynomial degrees (L-
 1027 curve method to optimize the degree). See the caption of Figure 11 for other symbols.

1028 **4.3 Data processing strategy**

1029 The 3D tomography input data are the STEC residuals (converted from VTEC) from
1030 available station-satellite pairs with LoS penetrating the voxels. I followed the procedure
1031 described in Chapter 3.3 of this thesis. I first calculate the absolute VTEC for each pair by
1032 multiplying the de-biased STEC with the cosine of the incidence angle of LoS into a thin shell at
1033 300 km altitude from the surface. The inter-frequency biases (station and satellite biases) are
1034 removed beforehand. The satellite biases are extracted from the header of the Global Ionosphere
1035 Maps (GIM) downloaded from aiub.unibe.ch/CODE. The receiver biases were estimated so that
1036 the scatters of VTEC during the stable local time (from midnight to dawn) are minimized
1037 (minimum scalloping).

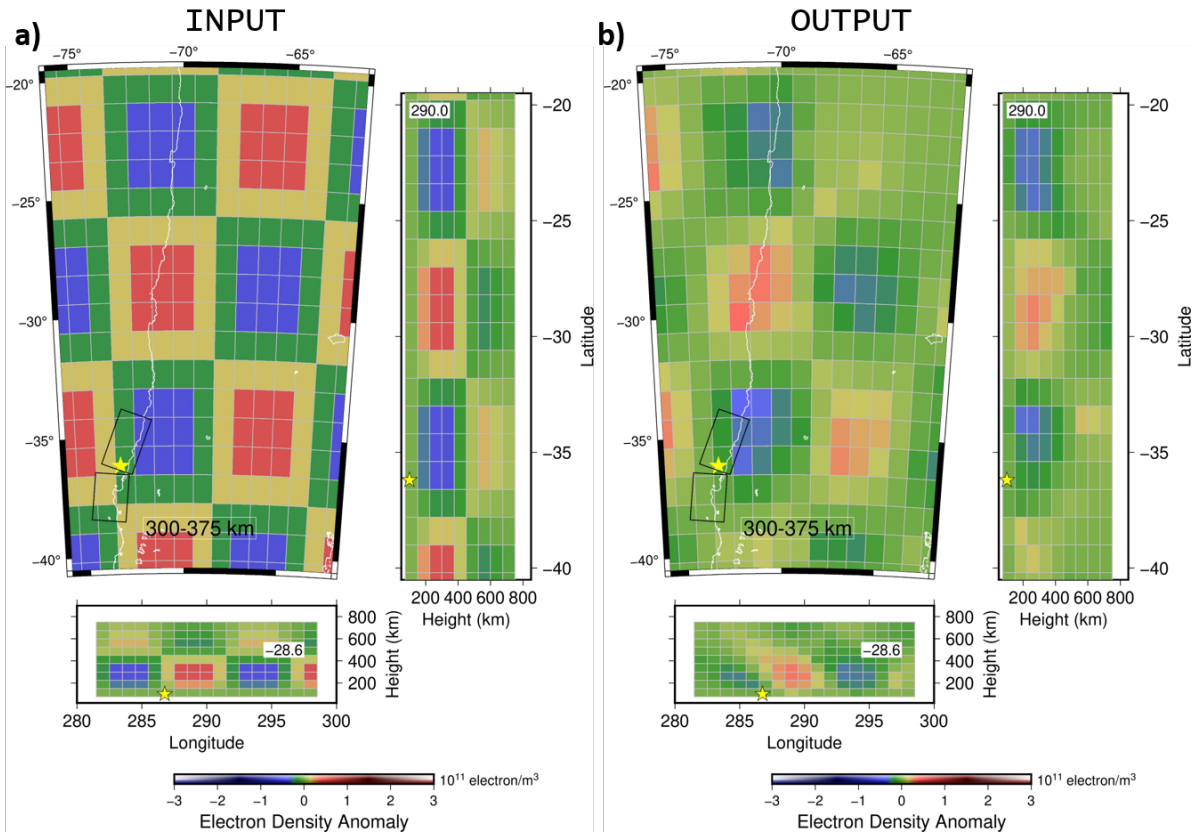
1038 The VTEC anomaly is obtained as the difference between the observed VTEC and
1039 reference curves estimated as polynomials whose degree is optimized by the L-curve method
1040 (selection of best degree of polynomial). The exclusion time-window was used in estimating the
1041 reference curves. The window starts from 40 minutes before the main shock following the
1042 detection of the bending done in Heki and Enomoto (2015) using AIC. As for the end time of the
1043 exclusion window, I employed 07:00 UT when the SIP trajectories of GPS-23 and GPS-20 left the
1044 focal region (Figure 25b and 25c), i.e. the position of the expected postseismic ionospheric hole.
1045 For the remaining GPS satellites, I used the same settings because this window worked fine for
1046 those satellite, too. VTEC residuals were converted back to STEC residuals by dividing with the
1047 cosine of the incidence angle that were used to convert the de-biased STEC to VTEC.

1048 **4.4 Resolution test**

1049 I set up the voxels for the 3D tomography of the electron density anomalies before and
1050 after the 2010 Maule earthquake. The 792 blocks are distributed above South America, with the
1051 size of 1.0° (east-west) \times 1.2° (north-south) \times 75 km (vertical) for the altitude range 75-750 km
1052 (Figure 25).

1053 The distribution of LoS and the block size are important factors for the accuracy of the
1054 tomography results. Before performing 3D tomography using the real STEC residual data, I first
1055 perform tests with synthetic data to recover artificial distribution of electron density anomalies to
1056 evaluate the accuracy of the method. I employ the classical checkerboard pattern for the resolution
1057 test. I assumed the same satellite and station geometry as the epoch 06:33 UT, 1 minute before the
1058 earthquake, to synthesize the input STEC data for the 3D tomography. In recovering the 3D
1059 distribution of electron density anomalies, I applied the same constraints as the 2011 Tohoku-oki
1060 case (continuity constraint and constraint around zero with altitude-dependent tolerance) as
1061 explained in the previous chapter.

1062 Figure 26a shows the assumed checkerboard pattern. It is composed of the electron density
1063 anomalies of $\pm 2.00 \times 10^{11}$ el/m³. I let the anomaly change gradually between the positive and
1064 negative parts to make the pattern consistent with the continuity constraint. I also assumed the
1065 amplitudes of the anomalies to decay in very high and low ionosphere to make it compatible with
1066 the other constraint.



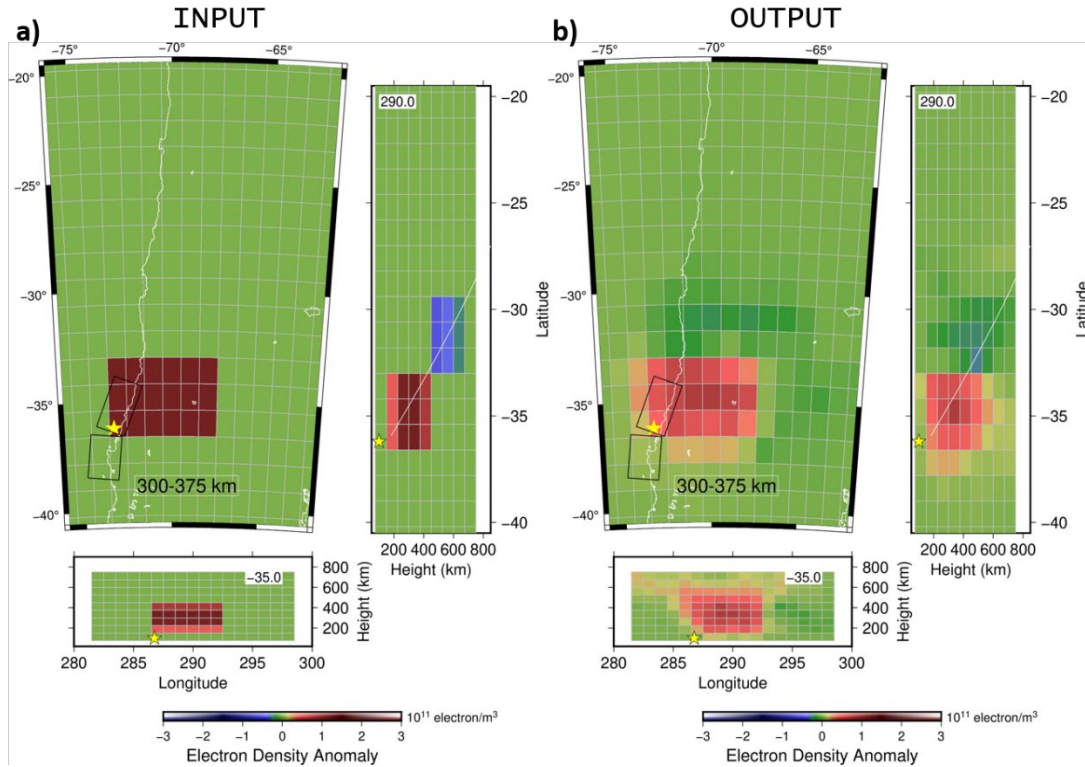
1067

1068 **Figure 26.** The resolution test of the 3D tomography of ionospheric electron density anomalies
 1069 before the 2010 Maule earthquake, central Chile, with the classical checkerboard pattern. The
 1070 assumed electron density anomalies (a) and the output of the 3D tomography (b) are given in map
 1071 view and north-south, east-west profiles. The yellow stars indicate the position of the epicenter of
 1072 the earthquake. Black rectangles is an approximate rupture area.

1073

1074 Figure 26b shows the recovered pattern for the blocks at the altitude range 300-375 km.
 1075 The pattern is well recovered particularly over the land and the offshore area within ~ 100 km from
 1076 the coast, including the area above the rupture. Similarly, in the vertical section the resolution
 1077 remains good in the altitudes 150-525 km, although the amplitudes of the recovered anomalies are
 1078 $\sim 1/3$ of the input model due possibly to the constraint around zero. On the other hand, resolution

1079 is poor where LoS do not penetrate the voxels (Figure 30). Such regions include the northeastern
1080 part of the studied area.



1081
1082 **Figure 27.** The second resolution test for a pair of positive and negative anomalies above middle
1083 of South America. The upper, bottom, and right panels are horizontal view, longitudinal and
1084 latitudinal profiles of the anomalies of the assumed pattern (a) and the output of the 3D tomography
1085 (b). Black rectangles is an approximate rupture area.

1086
1087 I next assessed the robustness of our result by recovering patterns composed of a pair of
1088 positive and negative ($\pm 2.30 \times 10^{11} \text{ el/m}^3$) anomalies in low and high altitudes along the
1089 geomagnetic field, respectively, in neutral background (Figure 27a). The results (Figure 27b) well
1090 reproduced the assumed pattern of the positive anomaly again reduced to $\sim 2/3$ amplitude of the
1091 input model due to the constraint.

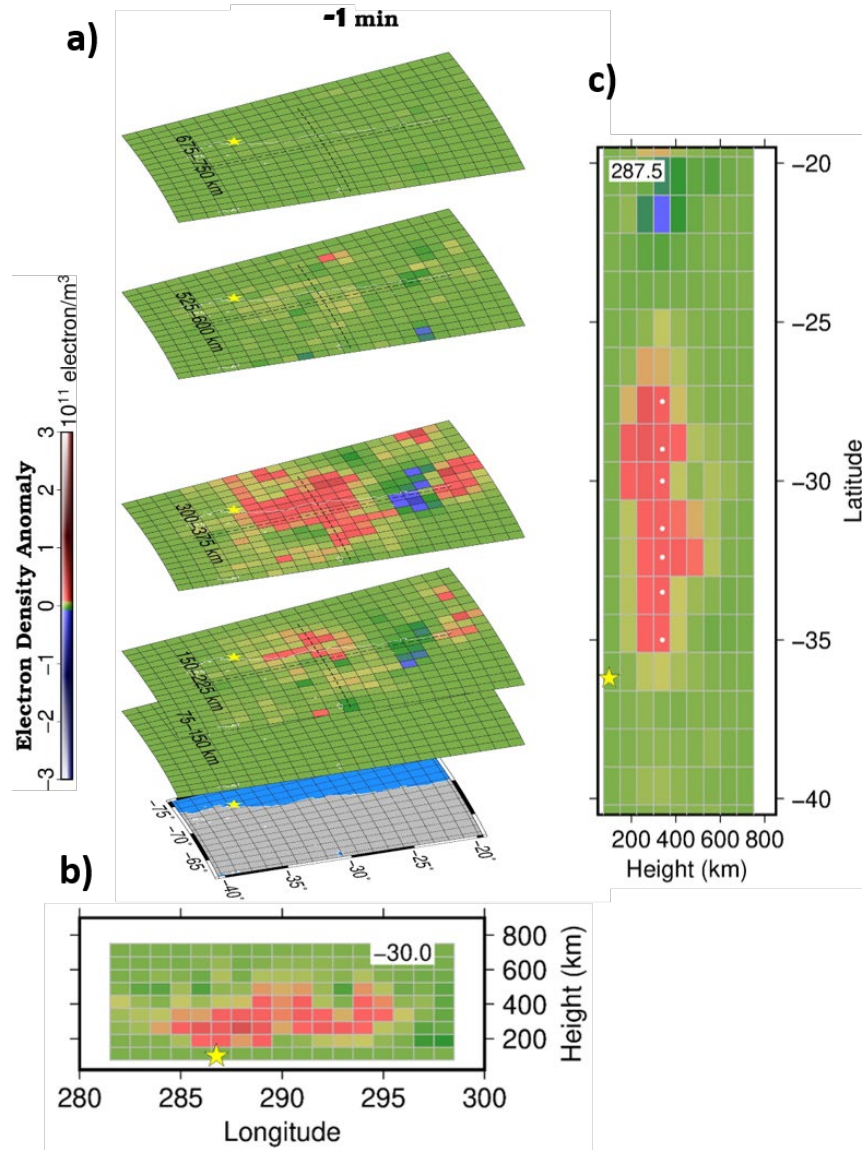
1092 However, the high-altitude negative anomaly pattern in the latitudinal profile is not well
1093 recovered. This indicates the limited availability of LoS is in the region where the negative
1094 anomaly is supposed to appear (Figure 30). The results of the two resolution tests show that our
1095 3D tomography results are accurate enough in a part of the region of interest, i.e., where the
1096 positive TEC anomalies are expected to emerge immediately before the 2010 Maule earthquake.
1097 However, it would be difficult to identify the negative anomaly expected to emerge at a higher
1098 altitude.

1099

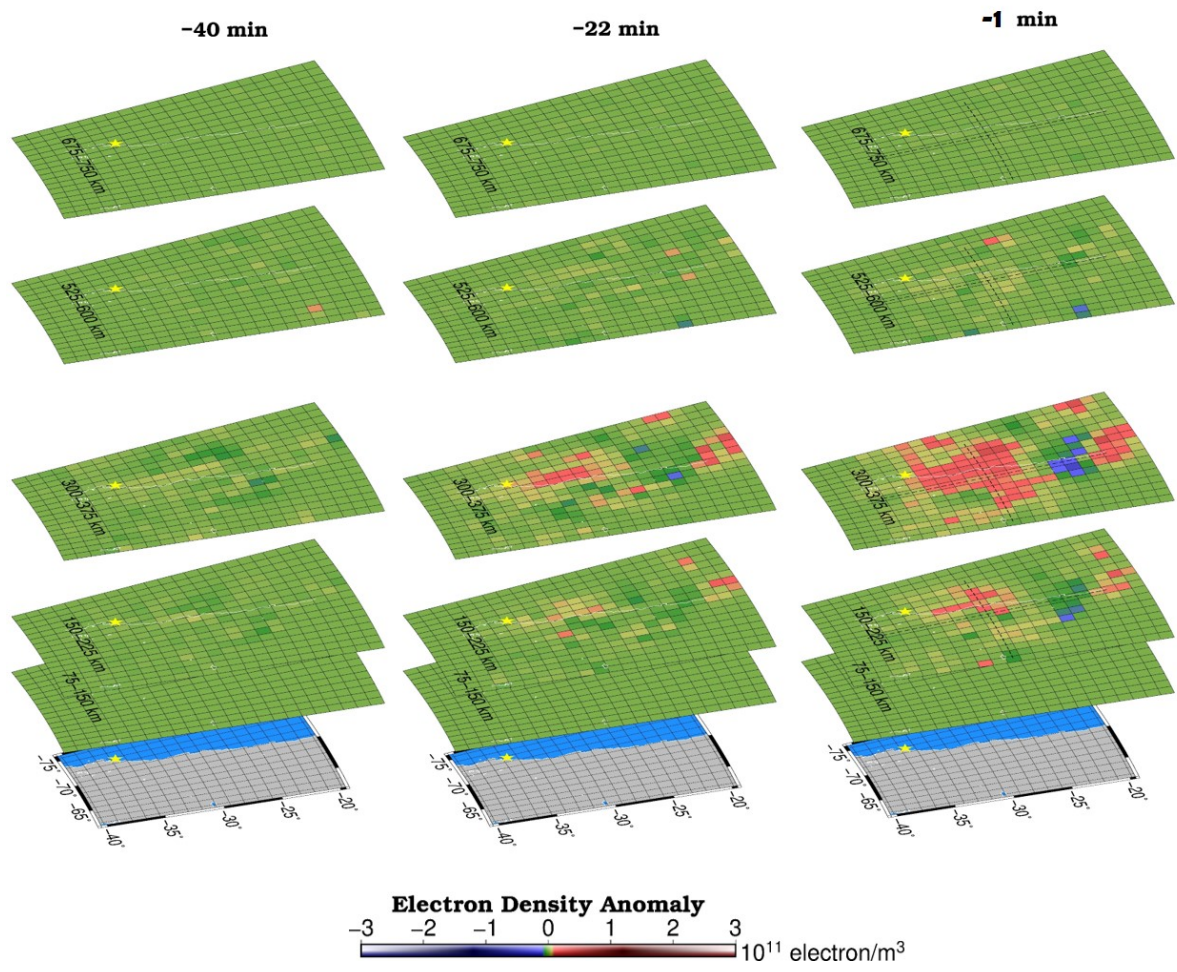
1100 **4.5 Tomography result**

1101 Figure 28 shows the map view of the 3D tomography result for altitudes of 75-750km at
1102 06:33 UT, 1 minute before the 2010 Maule earthquake, together with longitudinal and latitudinal
1103 profiles. Figure 29 shows the results at three epochs before the earthquake (40, 22 and 1 minutes
1104 before the earthquake). I confirmed beforehand that the performance of the tomography 40 and 22
1105 minutes before earthquake remains comparable to that 1 minute before earthquake shown in
1106 Figures 26 and 27. The results present that the strong positive electron density anomalies occurred
1107 at the 225-375 km altitude layers and the anomalies grow large without notable pattern change or
1108 spatial drifts toward the main shock. In fact, the latitude of the voxel showing the largest positive
1109 anomaly stays around 28°N during the 40 minutes period. The high-altitude negative electron
1110 density anomaly is not clear in this result. Figure 30 shows the LoS distributions in EW and NS
1111 profiles where the negative anomaly is supposed to appear. In comparison with Figure 15 for the
1112 2011 Tohoku-oki earthquake, it can be seen that there are not enough number of paths penetrating

1113 voxels in those areas. This is because the GNSS stations used here are fewer than the earlier study
 1114 for the 2015 Illapel earthquake (station increased markedly after the 2010 earthquake), and they
 1115 concentrate near the epicenter.



1116
 1117 **Figure 28.** 3D tomography results of electron density anomalies 1 minute before the 2010 Maule
 1118 earthquake (a). I also show the east-west (b) and north-south (c) profiles. Yellow stars show the
 1119 latitude and longitude of the epicenter. White circles in (c) show selected positions used to draw
 1120 Figure 31. The results for other epochs are given in Figure 29.

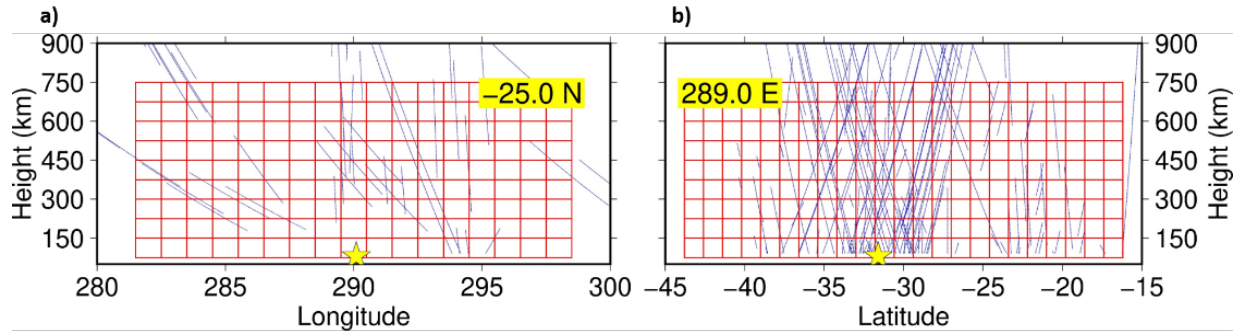


1121

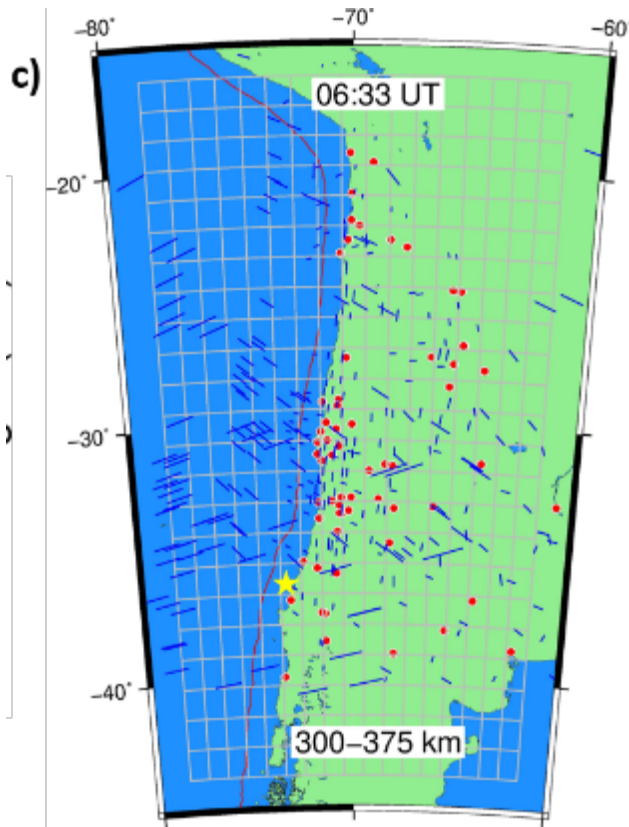
1122

1123 **Figure 29.** 3D tomography results of electron density anomalies from 75-750 km altitudes at three
 1124 epochs, 40, 22, and 1 minute before the 2010 Maule earthquake.

1125



1126

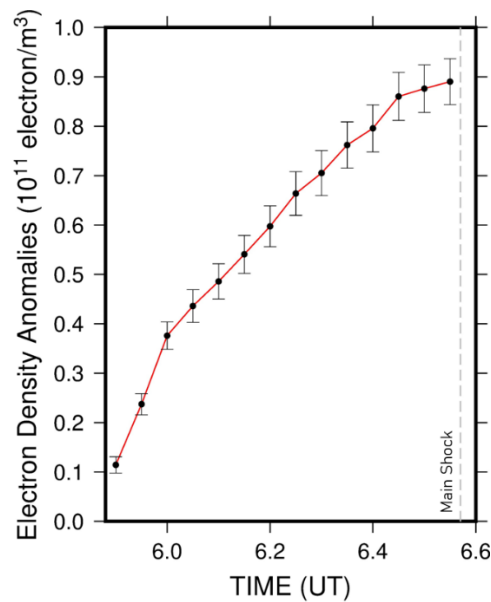


1127

1128 **Figure 30.** For vertical walls running east-west (a) and north-south (b) with the thickness of one
 1129 block, the LoS penetrating those walls are plotted with blue lines. Blue short lines in the map (c)
 1130 indicate the LoS of satellite-station pairs at the altitude 300-375 km (one layer of voxels) one
 1131 minute before the earthquake. Sparseness of the data can be confirmed by comparing with Figures
 1132 10 and 15 for the 2011 Tohoku-oki case.

1133

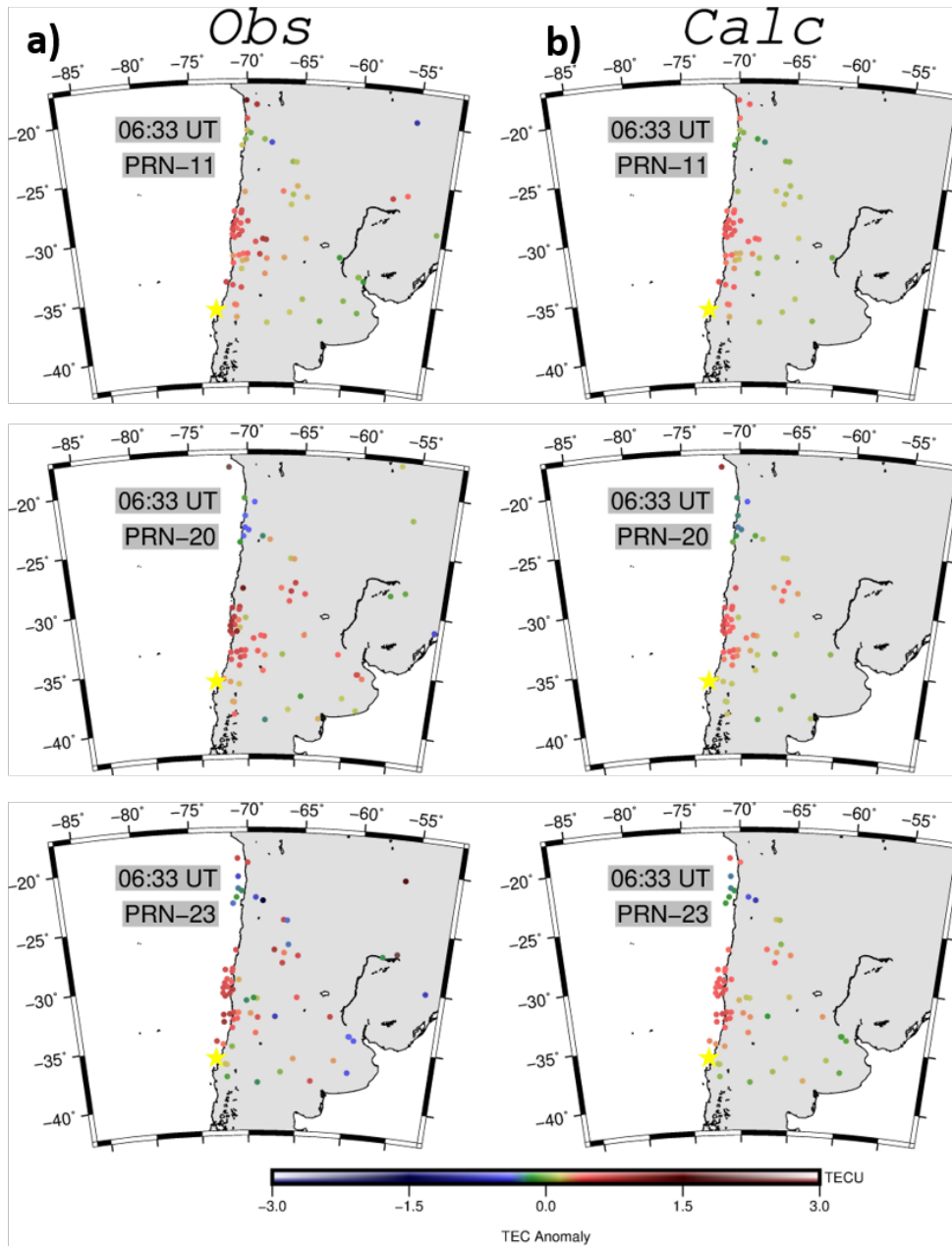
1134 In Figure 31, I plot the average estimated positive electron density anomalies of the three
1135 different blocks at the altitudes of 300-375 km using 3D tomography result in Figure 28. This
1136 corresponds to Figure 22 in the 2011 Tohoku-oki case. I could see the smooth growth of the
1137 positive anomaly from 40 to 1 minutes, around 5.9-6.5 UT, before the mainshock. Unlike Figure
1138 22, I did not include the growth curve for the negative anomalies. This is because the negative
1139 anomalies at high altitudes are hard to identify due to unfavorable distribution of the available LoS
1140 (Figure 30).



1141
1142 **Figure 31.** The growth of the average values of positive electron density anomalies at the three
1143 different blocks at the altitude of 300-375 km before the 2010 Maule earthquake. The error bars
1144 show the standard deviation around the average of the 7 voxels. The positions of the 7 voxels are
1145 indicated with white dots in Figure 28c.

1146
1147 Figure 32 compares the observed and calculated anomalies for four satellites, 11, 20, and
1148 23 at the epoch 1 minute before the main shock. The “observed” anomalies (Figure 32a) are those
1149 obtained as the departure from the reference curves to VTEC time series, and I plotted them at
80

1150 their SIP. On the other hand, the “calculated” anomalies (Figure 32b) were derived as the sum of
1151 the products of the estimated electron density anomalies (Figure 28) and the penetration lengths of
1152 voxels along the LoS. Such calculated STEC anomalies are converted to VTEC for comparison
1153 with the observed anomalies. These two are expected to nearly coincide if the 3D tomography
1154 inversion is successful. We can see that the observed TEC anomalies are well reproduced by the
1155 estimated 3D electron density anomalies shown in Figure 28.



1156

1157 **Figure 32.** Comparison of the observed (a) and calculated (b) VTEC anomalies for three GPS
 1158 satellites at the epoch at 06:33 UT, 1 minute before the earthquake. They are mostly consistent
 1159 with each other demonstrating that the estimated 3D electron density anomaly structure well
 1160 explains the observed TEC changes

1161 **4.6 Comparison with the 2011 Tohoku-oki and 2015 Illapel Earthquakes**

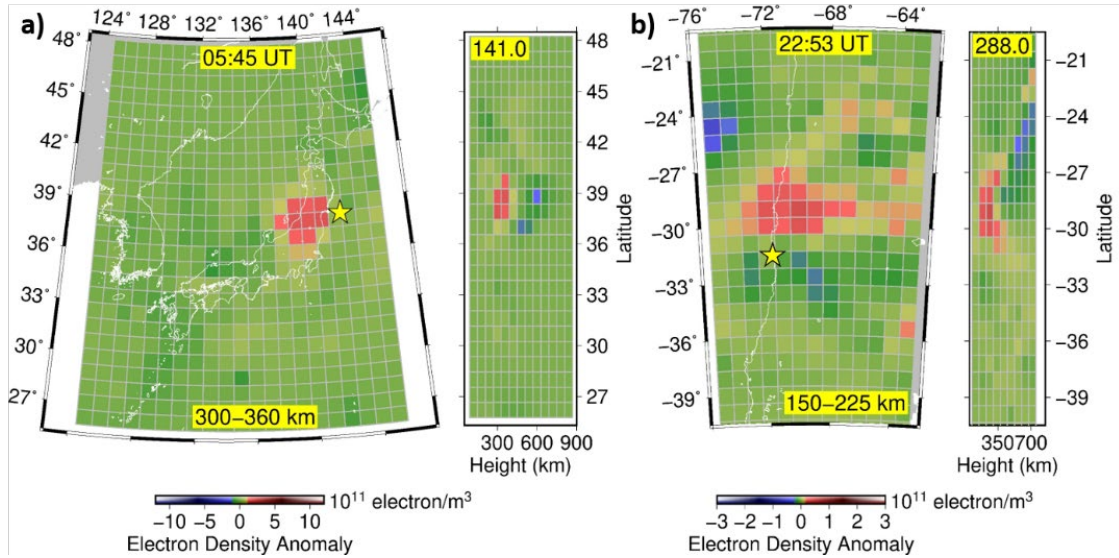
1162 Now, there are three examples of the 3D distributions of ionospheric electron density
1163 anomalies immediately before large earthquakes, i.e. 2011 Tohoku-oki (M_w 9.0, this thesis), 2015
1164 Illapel (M_w 8.3, He and Heki, 2018) and 2010 Maule earthquake (this thesis). They are compared
1165 in Figure 33. At a glance, we could see their similarities. They are composed of low-altitude
1166 positive anomalies and high-altitude negative anomalies. This does not apply for the 2010 Maule
1167 earthquake, but it is due to insufficient coverage of LoS in the region (Figure 27). Regarding the
1168 intensity of the anomaly, they largely differ (the two cases are drawn with different color palettes
1169 in Figure 33), i.e., the positive anomalies of the 2011 Tohoku-oki are ~ 7 times as strong as those
1170 of the 2015 earthquake. This would possibly reflect the difference in their magnitudes, M_w 9.0 and
1171 8.3, respectively.

1172 The 2010 Maule earthquake has slightly stronger preseismic anomalies than the 2015
1173 Illapel event (M_w 8.3), although its magnitude (M_w 8.8) is more similar to the 2011 Tohoku
1174 earthquake (M_w 9.0). It might be because the background VTEC is low during the 2010 Maule
1175 earthquake, which occurred very early in the morning (03:34 AM in local time). Smaller amount
1176 of the original ionospheric electron density would result in smaller anomalies. Here I compare
1177 them using the ratios of the anomalies observed as GPS-TEC to the background values using three
1178 station-satellite pairs for each case. I found the ratio is $9.2 \pm 0.74\%$ for 2010 Maule Earthquake,
1179 $9.63 \pm 1.91\%$ for 2011 Tohoku Earthquake, and $6.0 \pm 0.61\%$ for 2015 Illapel Earthquake. These
1180 results suggest that the intensity of ionospheric anomalies depends on earthquake magnitudes.
1181 Such M_w dependences are also seen in the leading times and the intensities of the initial bending
1182 of the VTEC curves (Heki and Enomoto, 2015; He and Heki, 2017).

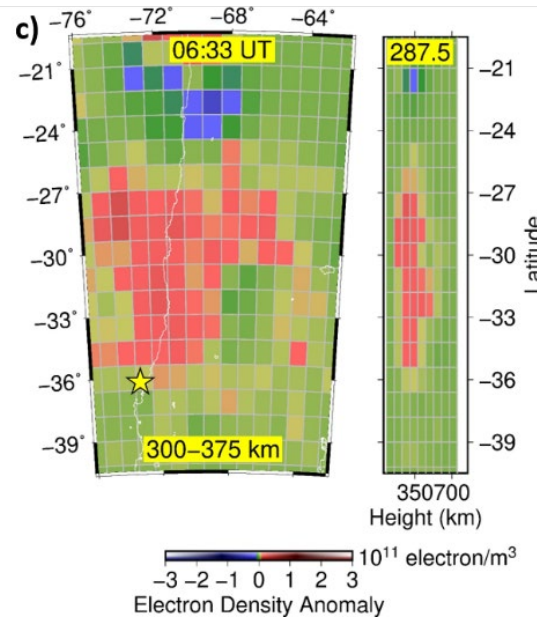
1183 As for the altitude where the anomalies appeared, their vertical profiles suggest that the
1184 altitudes of the positive and negative anomalies before the 2011 earthquake (~300 and ~600 km)
1185 are somewhat higher than the 2015 earthquake (~200 and ~500 km). The altitude of the positive
1186 anomaly before the 2010 Maule earthquake is similar to that of the 2011 earthquake (~300 km).
1187 Hence, it seems that the 3D structure of the anomalies spatially expands for earthquakes with larger
1188 magnitudes.

1189 On the other hand, horizontal extents of the anomalies before the 2011 and 2015
1190 earthquakes are little different in the three cases, i.e. the positive anomalies lie within circles with
1191 diameter of ~300 km for 2011 Tohoku earthquake. The horizontal extent of the positive anomalies
1192 before 2010 Maule (M_w 8.8) is much larger than the anomalies before 2015 Illapel (M_w 8.3). The
1193 difference is almost twice in north-south and east-west dimensions (Figure 33b,c). It suggests that
1194 magnitudes control the size of the anomaly if other conditions are similar. As I discussed in the
1195 previous chapter, the strong positive anomalies of the 2011 Tohoku-oki earthquake did not occur
1196 directly above the epicenter but emerged above land. This suggests that the electron redistribution
1197 is due to electric fields made by surface electric charges. Such surface charges would be relatively
1198 stable on land, but they diffuse rapidly in the ocean due to high electric conductivity of sea water.
1199 Horizontal extent of the anomaly before the 2011 Tohoku-oki earthquake might have been limited
1200 by the land-sea distribution in the Japanese Islands, i.e. the anomaly may have expanded larger if
1201 NE Japan was a continental arc like Chile.

1202



1203



1204 **Figure 33.** The estimated 3D distributions of ionospheric electron density anomalies prior to the
1205 2011 Tohoku-oki earthquake (this thesis) (a), the 2015 Illapel earthquake (He and Heki, 2018) (b),
1206 and the 2010 Maule earthquake (this thesis) (c), drawn with the similar spatial scales. Each case is
1207 composed of two panels showing the plan view and the north-south profile at the longitude
1208 crossing the anomaly. (a) and (b,c) use different colour palettes, and the anomalies in (a) are ~7
1209 times as strong as in (b). The anomalies in (c) has larger horizontal extent than in (b) suggesting
1210 magnitude also controls the size of the anomaly if ambient land-ocean geometry is similar. The
1211 yellow stars are the epicenters of the three events.

1212 **Chapter 5: 3D Tomography of the Ionospheric Anomalies after Earthquakes:**

1213 **The 2011 Tohoku-oki Earthquake**

1214

1215 *The content of this chapter was published in Journal Geophysical Research Space Physics, Muafiry, I.N.and K. Heki, 3D*

1216 *tomography of the ionospheric anomalies immediately before and after the 2011 Tohoku-oki (M_w 9.0) earthquake, J. Geophys. Res.*

1217 *Space Phys., 125, e2020JA027993, doi:10.1029/2020JA027993, 2020*

1218

1219 **5.1 Introduction: Tsunamigenic ionospheric anomalies**

1220 Ionospheric electron density drops (formation of the tsunami hole) are considered to occur
1221 right above the fault following the arrival of acoustic waves at the ionospheric F region ~10
1222 minutes after the 2011 Tohoku-oki earthquake (Kakinami et al., 2012; Shinagawa et al., 2013;
1223 Zettergren and Snively, 2019). The physics related to this ionospheric hole is discussed in Chapter
1224 5.6. Here I estimate the 3D structure of this postseismic anomaly to study its difference in structure
1225 and in position from the preseismic anomalies. This is expected to serve as a rebuttal to the
1226 opponents who claim that this hole served as a source of artifact for the preseismic TEC increases
1227 (Kamogawa and Kakinami, 2013; Masci et al., 2015).

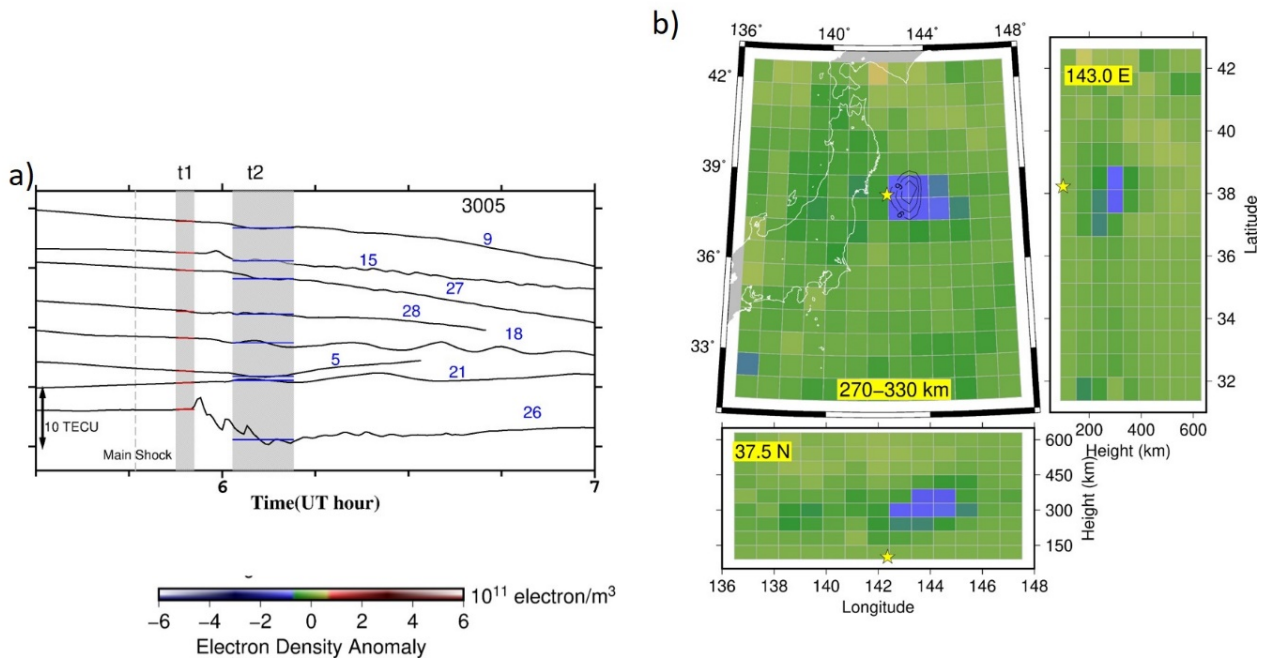
1228 **5.2 Data set**

1229 GNSS data from the entire GEONET is used, 1,231 GNSS stations, to study the post-
1230 seismic anomalies of the 2011 Tohoku-oki earthquake. I used 8 GPS satellites (PRN 05, 09, 15,
1231 18, 21, 26, 27, 28) visible from the studied region after the mainshock (05:46 UT). Unfortunately,
1232 GEONET did not track GNSS other than GPS in 2011. See also Chapter 2 for the detail of the
1233 input data. I did not use the GNSS data from Korea because of the remoteness of the Korean GNSS
1234 stations from the anomalies to the east of Honshu.

1235 **5.3 Data processing strategy**

1236 In Chapter 2.5, I explained two strategies to isolated TEC anomalies related to earthquakes.
1237 The first one is the modelling the temporal change of VTEC as a polynomial of time which is
1238 determined by least-squares method. The estimated models will serve as reference curves, and
1239 differences from these curves are defined as the anomalies. The other one is to make the difference

1240 between medians of VTEC from two periods (before and after the start of the anomalies). Here I
 1241 used the second strategy, i.e., I subtract the VTEC median before the ionospheric hole formation
 1242 from VTEC after the hole formation to isolate the VTEC changes associated with the generation
 1243 of the ionospheric hole.



1244
 1245 **Figure 34.** (a) VTEC time series of 8 GPS satellites, observed at 3005 in Kanto. The VTEC drops
 1246 are defined as the difference between the median VTEC values in the two periods (grey rectangles).
 1247 The flat red and blue lines within the two periods indicate the VTEC medians in the two periods,
 1248 and I used their differences as the input to the 3D tomography. (b) 3D tomography of the electron
 1249 depletion induced by the coseismic uplift and subsequent drop of the sea surface after the 2011
 1250 Tohoku-oki earthquake (yellow stars represent the epicenter). The contours in the plan view show
 1251 the fault slips in the main shock (the contour interval is 3 meters). Spatially integrated amounts of
 1252 negative and positive electron number changes are shown in Figure 22b in Chapter 3.

1253
 1254 At first, I get the medians of VTEC from the two periods, i.e. 5:52-5:55 UT and 6:03- 6:11
 1255 UT (two grey rectangles in Figure 34a), in VTEC time-series of GNSS stations. These periods

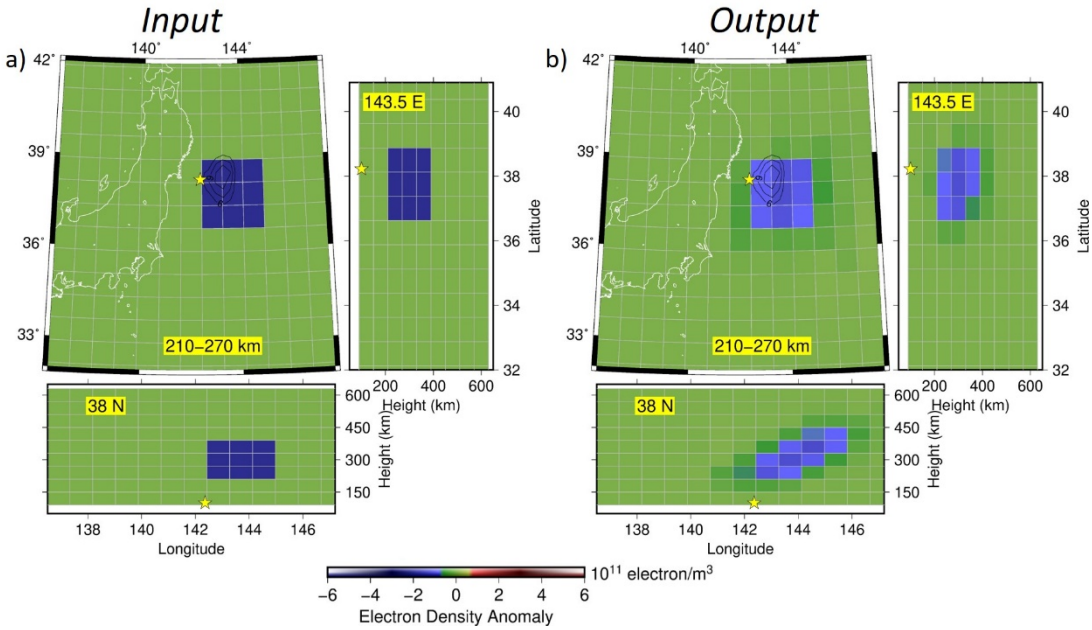
1256 correspond to times immediately before and after the ionospheric hole formation associated with
1257 the acoustic disturbance arrival. I do not use reference curves because the two periods are separated
1258 from each other by only ~10 minutes. The longer interval for the time window after the ionospheric
1259 hole formation was used because of the variety of acoustic disturbances occurring during this time
1260 window. In this method, we cannot remove the contribution from the long-term TEC decrease due
1261 to the increasing solar zenith angle. However, it would make a negative bias of the whole region
1262 and not as a localized anomaly.

1263 I converted the difference of VTEC between the two epochs into STEC and used them as
1264 the input to our tomography program. I used the satellite positions at 6:00 UT, the time in the
1265 middle of the two periods. This would not cause a problem because LoS movements during the 10
1266 minutes period is much less than the voxel size. I applied the same constraints as in the preseismic
1267 case to regularize the inversion.

1268 **5.4 Resolution tests**

1269 I performed the resolution test, by recovering patterns composed of a negative ($-3.00 \times$
1270 10^{11} el/m³) anomaly in the F-region above the fault in neutral background (Figure 35a). The 3D
1271 tomography results (Figure 35b) well reproduced the assumed pattern of the negative anomaly.
1272 Again, the recovered amplitude was reduced to $\sim 2/3$ of the input model due to the constraints. In
1273 the map view, we see only weak smears in surrounding blocks not exceeding a few percent of the
1274 assumed anomaly. However, significant smears are seen in EW profile (lower panel of the output)
1275 because the resolution is poor in the direction of LoS connecting the land and the anomaly. The
1276 results of the two resolution tests show that our 3D tomography results are accurate enough in the

1277 region of interest where the postseismic ionospheric hole appeared after the 2011 Tohoku-oki
1278 earthquake.



1279

1280 **Figure 35.** The resolution test for a compact negative anomaly off the Pacific coast of NE Japan.
1281 The upper, bottom, and right panels are horizontal view, latitudinal and longitudinal profiles of the
1282 anomalies of the assumed pattern (a) and the output of the 3D tomography with synthetic data (b).

1283

1284 **5.5 Tomography result**

1285 Figure 34b shows the 3D structure of the recovered electron density anomalies associated
1286 with the formation of the postseismic ionospheric hole. The main part of the negative electron
1287 density anomaly lies at height of ~300 km above the tsunami source area (the area of large vertical
1288 crustal movements). An important point is that they occur offshore just above the area of large
1289 coseismic slips (contours in Figure 34b), which makes a clear contrast to the preseismic anomalies
1290 that occurred above land (Figure 17a, Chapter 3). Another important point is that the anomaly is
1291 composed only of the negative anomalies in contrast to the pair of positive and negative preseismic
1292 anomalies (Figure 17c Chapter 3). This suggests that the loss of electrons due to their
1293 recombination with positive ions is the main mechanism for the negative anomaly. Next, I will
1294 discuss the physical mechanism of the postseismic ionospheric hole based on these 3D tomography
1295 results.

1296 **5.6 Physical mechanism of post-seismic anomalies**

1297 The negative postseismic anomaly extends offshore beyond the large slip region as far as
1298 ~145E (Figure 34b). However, this is considered be due to the smearing as seen in the resolution
1299 test (Figure 35). An important point is that the post-seismic anomalies are mainly composed of
1300 negative changes. This makes a sharp contrast with the preseismic anomalies whose positive and
1301 negative changes are nearly balanced throughout their growth as shown in Figure 22b in Chapter
1302 3.

1303 These contrasts would reflect the different physical mechanisms responsible for the pre-
1304 and postseismic anomalies, i.e. the former is caused by electron transport, but the latter is caused

1305 by the recombination of the electrons displaced downward by the acoustic disturbance as modelled
1306 by Kakinami et al. (2012) and Shinagawa et al. (2013). We also see that the dimension of the hole
1307 is consistent with the numerical simulation by Zettergren and Snively (2019).

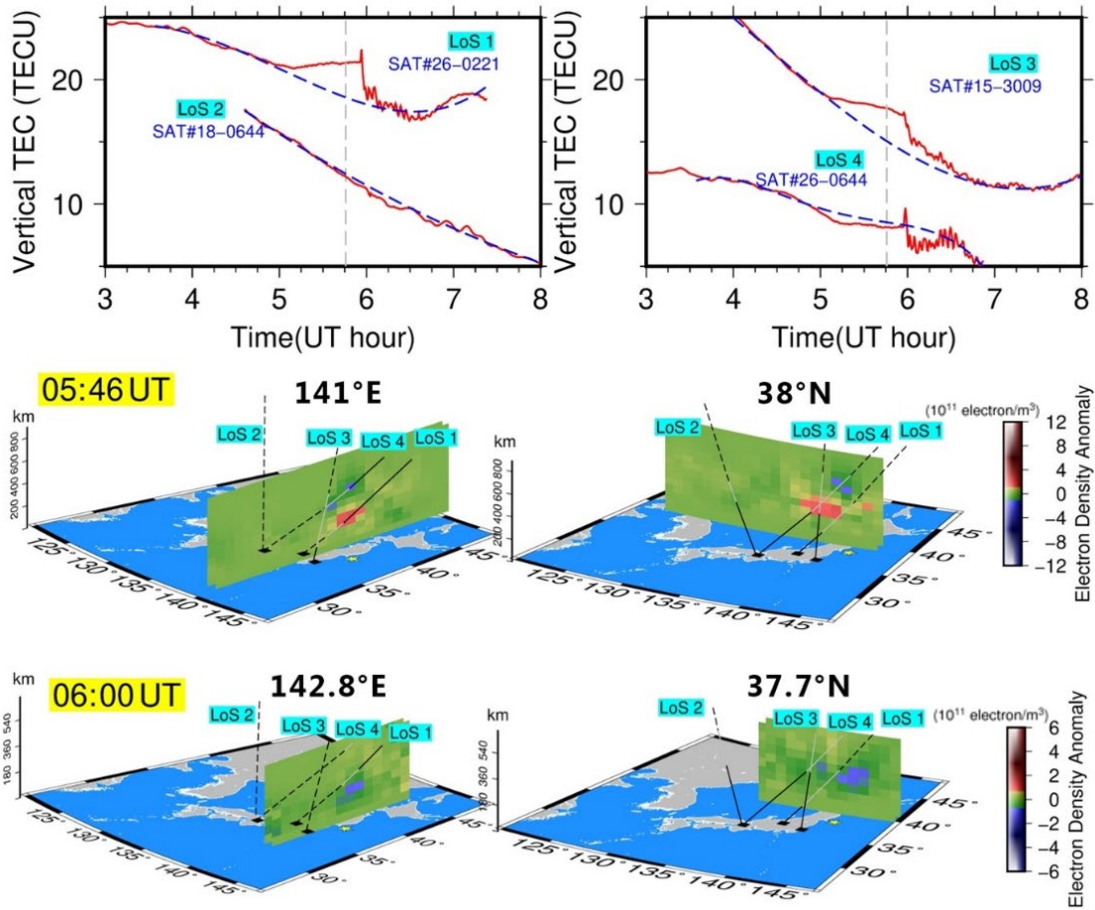
1308 **5.7 Origin of variety of waveforms**

1309 In Chapters 3 and 5, I showed two different kinds of anomalies of the ionospheric electron
1310 density, the preseismic and the postseismic anomalies. Now I identified three electron density
1311 anomalies different in time and polarity, i.e. #1 the preseismic positive anomaly, #2 the preseismic
1312 negative anomaly, and #3 the postseismic negative anomaly. #1 and #2 start to grow
1313 simultaneously at low and high ionosphere ~40 minutes before the earthquake and decay after the
1314 earthquake, while #3 emerges shortly after the acoustic disturbance arriving 8-10 minutes after the
1315 earthquake and last for tens of minutes.

1316 Heki (2011) noticed diversity of signatures of TEC disturbances related to earthquakes. For
1317 example, some LoS show only gradual growth and decay of positive signals (e.g. Sat.15- 3009
1318 shown in Figure 11a) while other LoS show sudden decrease after the acoustic disturbances (e.g.
1319 Sat.26-0946 shown in Figure 11b). On the other hand, some LoS, like the cyan time series in Figure
1320 11 top, show negative changes during the preseismic period. These varieties reflect the difference
1321 in the penetration of those LoS with the anomalies #1, #2, and #3. For example, Sat.15-3009
1322 penetrated only #1, while Sat.26-0946 penetrated both #2 and #3.

1323 Figure 36 explains the variety of waveforms of VTEC changes before and after the
1324 earthquake coming from the diversity in the penetrations of LoS with these three anomalies. There
1325 are four typical VTEC signatures observed in different satellite-station pairs, (1) LoS penetrating

1326 both the preseismic positive and postseismic negative anomalies, (2) LoS without penetrating any
 1327 anomalies, (3) LoS penetrating only preseismic positive, and (4) LoS penetrating only the
 1328 postseismic negative anomalies. In Figure 36, I also show tomography profile before and after the
 1329 earthquake and how the four LoS penetrate them. The VTEC time series are shown on top.



1330

1331 **Figure 36.** The 4 types of VTEC waveforms from different station-satellite pairs (upper panels),
 1332 LoS 1 (Sa.26-0221) penetrating both the preseismic positive and postseismic negative anomalies,
 1333 LoS 2 (Sat.18-0644) without penetrating any anomalies, LoS 3 (Sat.15-3009) penetrating only
 1334 preseismic positive anomaly, and LoS 4 (Sat.26-0644) penetrating only the postseismic negative
 1335 anomaly. Bottom panels are the 3D tomography result of preseismic and postseismic anomalies
 1336 overlain with the LoS of the four examples. Black and grey lines indicate LoS in front of and
 1337 within the profile (one block thick). Black dashed lines correspond to the LoS behind the profile.

1338 93

1339 **Chapter 6: Conclusions and Recommendation**

1340 **6.1 Conclusions**

1341 I studied the 3D structure of the ionospheric electron density anomalies immediately before
1342 the 2011 Tohoku-oki (M_w 9.0) and 2010 Maule (M_w 8.8) earthquakes by using GNSS-TEC data
1343 taken in Japan, South Korea, and South America in order to contribute to the understanding of the
1344 physical processes responsible for the preseismic ionospheric anomalies found by Heki (2011).

1345 I paid special attention to the detail of the method to obtain the TEC anomalies as the input
1346 to the 3D tomographic inversion program. I optimized the polynomial degrees for the reference
1347 curves using the L-curve method. The exclusion windows were set up to estimate the reference
1348 curves without being influenced by ionospheric disturbances due to earthquakes. The start of the
1349 window was defined by the positive bending of the TEC time series detected by statistical
1350 techniques in an earlier study (Heki and Enomoto, 2015). The end of the window was selected
1351 carefully to avoid the interference from the postseismic ionospheric hole.

1352 The linear inversion is stabilized by continuity and altitude-dependent constraints, and the
1353 performance of the method was confirmed by trying 3D tomography to artificial patterns, a
1354 classical checkerboard pattern and a realistic pattern of a pair of positive and negative anomalies.
1355 The tests showed that I can resolve electron density anomalies in the ionosphere above regions
1356 with enough number of ground stations. However, it is not expected that we can identify the upper
1357 negative anomaly before the 2010 Maule earthquake.

1358 The 3D tomography results of the two cases, together with another study for the 2015
1359 Illapel earthquake (He and Heki, 2018), showed that the preseismic ionospheric anomaly has

1360 following similarities; (1) They are composed of pairs of low-altitude positive and high-altitude
1361 negative (not detected for the 2010 Maule earthquake due to limited LoS distribution) electron
1362 density anomalies. (2) They occur above the land area close to the submarine faults. (3) They have
1363 clear onsets a few tens of minutes before earthquakes (~40 min before 2011 Tohoku-oki, and
1364 Maule, and ~20 minutes before the Illapel earthquakes) and grow with decaying rates.

1365 I compared strengths of the electron density anomalies before these three earthquakes. For
1366 example, the positive electron density anomalies before the 2011 Tohoku-oki case was seven times
1367 as strong as that for the 2015 Illapel case. The strength of the preseismic anomalies was also found
1368 to be controlled by the background electron density on the earthquake days. For example, the
1369 positive electron density anomaly before the 2010 Maule earthquake was only as strong as in the
1370 2015 Illapel case. This might be due to smaller electron density in the 2010 earthquake that
1371 occurred after the midnight.

1372 I also compared the dimensions of the electron density anomalies before these three
1373 earthquakes. The 2011 earthquake showed positive anomalies lying above the land, and not above
1374 the submarine epicenter. On the other hand, the 2010 Maule and 2015 Illapel earthquakes showed
1375 positive anomalies located above the coast (i.e. both above land and above ocean close to the coast).
1376 This means that the anomaly partly smears out to the ocean, but it is difficult to tell if it comes
1377 from inadequate density and distribution of the ground GNSS stations. The areal extent of the
1378 anomaly before the 2015 case was similar to the 2011 case. This would be due to the different
1379 situation of land-ocean distribution for the two cases, e.g., the land area is limited in NE Japan, an
1380 island arc, in the 2011 Tohoku-oki case. The 2010 Maule earthquake showed the largest horizontal
1381 extent. This might reflect a larger proportion of land in a continental arc like Chile.

1382 I presented the model for the physical process of the preseismic ionospheric anomalies
1383 consistent with such 3D structure proposed in Muafiry and Heki (2020). Micro-scale cracks and
1384 dislocations could mobilize positive electric charges shortly before large earthquakes. They would
1385 concentrate near the land surface and generate upward electric fields. The field would then reach
1386 the ionosphere and generates electromotive forces to make electrons move down along the
1387 geomagnetic fields. This would continue until the induced downward electric field cancels the
1388 upward fields due to crustal electric charges, making the electric potential uniform along the
1389 magnetic field.

1390 The current will depend on the along-B component of the external electric field and the
1391 density of free electrons as a function of altitude. The nonuniform electric currents would result in
1392 convergence/divergence of electrons and make positive/negative electron density anomalies at the
1393 lower/higher ionosphere along the magnetic field, the structure consistent with those found for
1394 these three earthquakes by 3D tomography. This upward current (downward electron migration)
1395 would also make eastward/westward magnetic field in regions to the south/north of the epicenter
1396 before earthquakes in northern/southern hemisphere.

1397 I also studied the 3D structure of the postseismic anomalies of 2011 Tohoku-oki earthquake
1398 and found that the negative electron density anomaly emerged offshore just above the submarine
1399 fault. Variety of TEC change patterns observed before and after the 2011 Tohoku-oki earthquake
1400 is understood by different combinations of the penetrations of LoS with such electron density
1401 anomalies.

1402 **6.2 Recommendation**

1403 1. There are variety of features of scientific importance in the ionosphere. Conventional
1404 sensors, such as satellite in-situ observations and ionosondes, used to require a lot of efforts and
1405 resources to observe ionosphere. Recent launch of GNSS satellite and deployment of ground
1406 networks of continuous GNSS receivers made such studies much easier for everyone to start. Such
1407 ionospheric studies using GNSS data are especially suitable for university laboratories with limited
1408 human and financial resources.

1409 2. In comparison with the analysis of total electron content (TEC) along line-of-sights
1410 (LoS), 3D tomography provides a robust way to study the 3D structure of various ionospheric
1411 disturbances. The targets of 3D tomography are not limited to those related to surface phenomena
1412 such as earthquakes. It can be applied for various space weather phenomena including various
1413 traveling ionospheric disturbances and sporadic-E irregularities. 3D tomography technique gives
1414 opportunity for human to understand the earth's upper atmosphere better.

1415 3. Ionospheric anomalies occurring immediately before large earthquake, found by Heki
1416 (2011), can become a key phenomenon toward practical earthquake prediction and mitigation of
1417 earthquake disasters in the future. 3D tomography for the electron density anomalies for such
1418 phenomena provides important insight into the physical processes responsible for them. Based on
1419 the 3D structure of the preseismic ionospheric anomalies, I proposed one such model assuming
1420 that surface electric charge redistribute ionospheric electrons through electric fields. In the future,
1421 detailed observations of the ground electric charges might give a conclusive evidence for the
1422 validity of such models.

1423 4. Regarding the practical aspect, sophisticated statistical techniques would be necessary
1424 to detect preseismic ionospheric anomalies as discussed in this thesis, together with automated
1425 real-time analyses of GNSS-TEC data to establish operational early warning system of large
1426 earthquakes.

1427

1428

1429 **References**

- 1430 Astafyeva, E. and K. Heki (2009), Dependence of waveform of near-field coseismic ionospheric
1431 disturbances on focal mechanisms, *Earth Planet. Space*, *61*, 939-943.
- 1432 Astafyeva, E., K. Heki, V. Kiryushkin, E. Afraimovich, S. Shalimov (2009), Two-mode long-
1433 distance propagation of coseismic ionosphere disturbances, *J. Geophys. Res.*, *114*, A10307,
1434 doi:10.1029/2008JA013853.
- 1435 Astafyeva, E., P. Lognonné, and L. Rolland (2011), First ionospheric images of the seismic fault
1436 slip on the example of the Tohoku-oki earthquake, *Geophys. Res. Lett.*, *38*, L22104.
1437 [doi:10.1029/2011GL049623](https://doi.org/10.1029/2011GL049623)
- 1438 Astafyeva, E. and K. Shults (2019), Ionospheric GNSS imagery of seismic source: Possibilities,
1439 difficulties, and challenges, *J. Geophys. Res. Space Phys.*, *124*, 534-543.
1440 doi:10.1029/2018JA026107.
- 1441 Austen JR, Franke J, Liu CH (1988) Ionospheric imaging using computerized tomography. *Radio*
1442 *Sci.*, *23*:299–307, doi:10.1029/RS023i003p00299
- 1443 Cahyadi, M. N., and K. Heki (2015), Coseismic ionospheric disturbance of the large strike-slip
1444 earthquakes in North Sumatra in 2012: M_w dependence of the disturbance amplitudes, *Geophys.*
1445 *J. Int.*, *200(1)*, 116-129, doi:10.1093/gji/ggu343.
- 1446 Calais, E. and J. B. Minster (1995), GPS detection of ionospheric perturbations following the
1447 January 17, 1994, Northridge earthquake, *Geophys. Res. Lett.*, *22*, 1045–1048,
1448 doi:10.1029/95GL00168.

- 1449 Chen, C. H. A. Saito, C. H. Lin, M. Yamamoto, S. Suzuki, G. K. Seemala (2016), Medium-scale
1450 traveling ionospheric disturbances by three-dimensional ionospheric GPS tomography, *Earth,*
1451 *Planets and Space*, 68:32, DOI 10.1186/s40623-016-0412-6
- 1452 Choi, B.-K., and J. Hong (2019), Observation of the fast-traveling ionospheric disturbances
1453 induced by the 2017 North Korean missile, *Adv. Space Res.*, 63, 2598-2608,
1454 doi:10.1016/j.asr.2018.12.033.
- 1455 Coster, A., J. Williams, A. Weatherwax, W. Rideout, and D. Herne (2013), Accuracy of GPS total
1456 electron content: GPS receiver bias temperature dependence. *Radio Science*, 48, 190–196.
1457 doi:10.1002/rds.20011
- 1458 Freund, F. T. (2011), Pre-earthquake signals: Underlying physical processes. *Journal Asian Earth*
1459 *Sci.*, 41(4-5), 383–400. [doi:10.1016/j.jseaes.2010.03.009](https://doi.org/10.1016/j.jseaes.2010.03.009)
- 1460 Freund, F. (2013), Earthquake forewarning - A multidisciplinary challenge from the ground up to
1461 space, *Acta Geophys.*, 6(14), 775-807, doi:10.2478/s11600-013-0130-4.
- 1462 Garcia, R., F. Crespon, V. Ducic, P. Lognonné (2005), Three-dimensional ionospheric tomography
1463 of post-seismic perturbations produced by the Denali earthquake from GPS data, *Geophys. J. Int.*,
1464 163, 1049–106, doi: 10.1111/j.1365-246X.2005.02775.x
- 1465 He, L., and Heki, K. (2016). Three-dimensional distribution of ionospheric anomalies prior to three
1466 large earthquakes in Chile. *Geophys. Res. Lett.*, 43, 7287–7293. doi:10.1002/2016GL069863
- 1467 He, L., and K. Heki (2017), Ionospheric anomalies immediately before M_w 7.0–8.0 earthquakes. *J.*
1468 *Geophys. Res. Space Phys.*, 122, 8659–8678. [doi:10.1002/2017JA024012](https://doi.org/10.1002/2017JA024012)

1469 He, L., and K. Heki (2018), Three-dimensional tomography of ionospheric anomalies immediately
1470 before the 2015 Illapel earthquake, Central Chile, *J. Geophys. Res. Space Phys.*, *123*, 4015–4025.
1471 [doi:10.1029/2017JA024871](https://doi.org/10.1029/2017JA024871)

1472 He, L., K. Heki, and L. Wu (2018), Three-dimensional and trans-hemispheric ionospheric electron
1473 density changes by the great Solar eclipse in North America on 21 August 2017, *Geophys. Res.
1474 Lett.*, *45*, 10,933-10,940, doi:10.1029/2018GL080365.

1475 Heki, K. and J.-S. Ping (2005), Directivity and apparent velocity of the coseismic ionospheric
1476 disturbances observed with a dense GPS array, *Earth Planet. Sci. Lett.*, *236*, 845–855,
1477 doi:10.1016/j.epsl.2005.06.010.

1478 Heki, K. (2006), Explosion energy of the 2004 eruption of the Asama Volcano, Central Japan,
1479 inferred from ionospheric disturbances, *Geophys. Res. Lett.*, *33*, L14303,
1480 doi:10.1029/2006GL026249

1481 Heki, K. (2011), Ionospheric electron enhancement preceding the 2011 Tohoku-oki earthquake.
1482 *Geophys. Res. Lett.*, *38*, L17312. doi:10.1029/2011GL047908

1483 Heki, K. and Y. Enomoto (2013), Preseismic ionospheric electron enhancements revisited, *J.
1484 Geophys. Res.*, *118*, 6618-6626, doi:10.1002/jgra.50578.

1485 Heki, K. and Y. Enomoto (2014), Reply to comment by K. Heki and Y. Enomoto on "Preseismic
1486 ionospheric electron enhancements revisited", *J. Geophys. Res. Space Phys.*, *119*,
1487 doi:10.1002/2014JA020223.

- 1488 Heki, K., and Y. Enomoto (2015), M_w dependence of the preseismic ionospheric electron
1489 enhancements. *J. Geophys. Res. Space Phys.*, *120*, 7006–7020, doi:10.1002/2015JA021353.
- 1490 Heki, K. (2021), Chapter 21: Ionospheric disturbances related to earthquakes in *Advances in*
1491 *ionospheric research: Current understanding and challenges*, Wiley/AGU Book Space Physics
1492 and Aeronomy, Volume 3, edited by C. Huang and G. Lu, pp.320, ISBN:978-1-119-50755-0.
- 1493 Iwata, T. and K. Umeno (2016), Correlation Analysis forpreseismic Total Electron Content
1494 Anomalies around the 2011 Tohoku-oki Earthquake, *J. Geophys. Res. Space Phys.*, *121*, 8969-
1495 8984, doi:10.1002/2016JA023036
- 1496 Jara-Munoz, J., D. Melnick, D. Brill, M. R. Strecker (2015), Segmentation of the 2010 Maule
1497 Chile earthquake rupture from a joint analysis of uplifted marine terraces and seismic-cycle
1498 deformation patterns, *Quaternary Science Reviews*, *113*:171-192,
1499 doi:10.1016/j.quascirev.2015.01.005
- 1500 Kakinami, Y., M. Kamogawa, Y. Tanioka, S. Watanabe, A. R. Gusman, J.-Y. Liu, Y. Watanabe,
1501 and T. Mogi (2012), Tsunamigenic ionospheric hole, *Geophys. Res. Lett.*, *39*, L00G27,
1502 doi:10.1029/2011GL050159
- 1503 Kamogawa, M., and Y. Kakinami (2013), Is an ionospheric electron enhancement preceding the
1504 2011 Tohoku-oki earthquake a precursor? *J. Geophys. Res. Space Phys.*, *118*, 1751–1754,
1505 doi:10.1002/jgra.50118.
- 1506 Kelley, M.C. (2009), *The Earth's Ionosphere: Plasma Physics and Electrodynamics*, Elsevier, 2nd
1507 ed.

1508 Kelley, M. C., W. E. Swartz, and K. Heki (2017), Apparent ionospheric total electron content
1509 variations prior to major earthquakes due to electric fields created by tectonic stresses, *J.*
1510 *Geophys. Res. Space Phys.*, *122*, doi:10.1002/2016JA023601.

1511 Kundu, B., B. Senapati, A. Matsushita, and K. Heki (2021), Atmospheric wave energy of the 2020
1512 August 4 explosion in Beirut, Lebanon, from ionospheric disturbances, *Sci. Rep.*, *11*, 2793,
1513 doi:10.1038/s41598-021-82355-5.

1514 Kuo, C. L., L. C. Lee, and J. D. Huba (2014), An improved coupling model for the lithosphere-
1515 atmosphere-ionosphere system, *J. Geophys. Res. Space Phys.*, *119*, 3189-3205,
1516 doi:10.1002/2013JA019392.

1517 Kwon, J. (2012), Korea Geodetic Framework for Sustainable Development, *Nineteenth United*
1518 *Nations Regional Cartographic, Conference for Asia and the Pacific*, E/CONF.102/IP.17.

1519 Le, H., Liu, J. Y., and Liu, L. (2011), A statistical analysis of ionospheric anomalies before 736
1520 M6.0+ earthquakes during 2002–2010. *J. Geophys. Res.*, *116*, A02303.
1521 doi:10.1029/2010JA015781

1522 Li, M., and Parrot, M. (2013), Statistical analysis of an ionospheric parameter as a base for
1523 earthquake prediction. *J. Geophys. Res.*, *118*, 3731–3739. doi:10.1002/jgra.50313

1524 Liu, J.-Y., Y.-B. Tsai, K.-F. Ma, Y.-I. Chen, H.-F. Tsai, C.-H. Lin, M. Kamogawa, C.-P. Lee,
1525 (2006), Ionospheric GPS total electron content (TEC) disturbances triggered by the 26 December
1526 2004 Indian Ocean tsunami. *J. Geophys. Res.*, *111*, A05303, doi:10.1029/2005JA011200

1527 Liu, J. Y., Chen, Y. I., Chuo, Y. J., and Tsai, H. F. (2001), Variations of ionospheric total electron
1528 content during the Chi-Chi earthquake. *Geophys. Res. Lett.*, *28*, 1383–1386.

1529 Masci, F., J. Thomas, F. Villani, J. Secan, and N. Rivera (2015), On the onset of ionospheric
1530 precursors 40 min before strong earthquakes, *J. Geophys. Res. Space Phys.*, *120*(2), 1383-1393,
1531 doi:10.1002/2014JA020822.

1532 Muafiry, I. N. and K. Heki (2020), 3D tomography of the ionospheric anomalies immediately
1533 before and after the 2011 Tohoku-oki (Mw9.0) earthquake, *J. Geophys. Res. Space Phys.*, *125*,
1534 e2020JA027993, doi:10.1029/2020JA027993.

1535 Muafiry, I. N., K. Heki, and J. Maeda (2018), 3D tomography of midlatitude sporadic-E in Japan
1536 from GNSS-TEC data. *Earth, Planets Space*, *70*(1). [doi:10.1186/s40623-018-0815-7](https://doi.org/10.1186/s40623-018-0815-7)

1537 Němec, F., Santolik, O., Parrot, M., and Berthelier, J. J. (2008), Spacecraft observations of
1538 electromagnetic perturbations connected with seismic activity. *Geophys. Res. Lett.*, *35*, L05109.
1539 doi:10.1029/2007GL032517

1540 Occhipinti, G., P. Lognonné, E. A. Kherani, and H. Hébert (2006), Three-dimensional waveform
1541 modeling of ionospheric signature induced by the 2004 Sumatra tsunami, *Geophys. Res. Lett.*,
1542 *33*, L20104, doi:10.1029/2006GL026865.

1543 Otsuka Y, Kotake N, Shiokawa K, Ogawa T, Tsugawa T, Saito A (2011), Statistical study of
1544 medium-scale traveling ionospheric disturbances observed with a GPS receiver network in Japan.
1545 In: *Aeronomy of the earth's atmosphere and ionosphere, IAGA Special Sopron Book Series, vol*
1546 *2, part 3*, pp 291–299. doi:10.1007/978-94-007-0326-1_21

1547 Ozawa, S., T. Nishimura, H. Suito, T. Kobayashi, M. Tobita, and T. Imakiire (2011), Coseismic
1548 and postseismic slip of the 2011 magnitude-9 Tohoku-Oki earthquake. *Nature*, 475, 373-376.
1549 doi:10.1038/nature10227

1550 Rideout, W., and A. Coster (2006), Automated GPS processing for global total electron content
1551 data, *GPS Solut.*, 10, 219–228, doi:10.1007/s10291-006-0029-5.

1552 Rolland, L. M., G. Occhipinti, P. Lognonné, A. Loevenbruck (2010), Ionospheric gravity waves
1553 detected offshore Hawaii after tsunamis, *Geophys. Res. Lett.*, 37, L17101,
1554 doi:10.1029/2010GL044479.

1555 Rolland, L. M., M. Vergnolle, J.-M. Nocquet, A. Sladen, J.-X. Dessa, F. Tavakoli, H. R. Nankali,
1556 and F. Cappa (2013), Discriminating the tectonic and non-tectonic contributions in the
1557 ionospheric signature of the 2011, M_w 7.1, dip-slip Van earthquake, Eastern Turkey, *Geophys.*
1558 *Res. Lett.*, 40, 2518–2522, doi:10.1002/grl.50544.

1559 Saito S, S. Suzuki, M. Yamamoto, C.H. Chen, A. Saito (2016), Real-time ionosphere monitoring
1560 by three-dimensional tomography over Japan. In: *Proc. 29th int. tech. meeting, Satellite Division*
1561 *of the Institute of Navigation (ION GNSS+2016)*, Portland, Oregon. pp 706–713.

1562 Sakai, T. (2005), Bias error calibrations for observing ionosphere by GPS network, *IEICE Trans.*
1563 *Comm.*, J88-B, 2382-2389. (in Japanese)

1564 Seemala G. K., M. Yamamoto, A. Saito, C. H. Chen (2014), Three-dimensional GPS ionospheric
1565 tomography over Japan using constrained least squares. *J. Geophys. Res. Space Phys.*, 119,
1566 3044–3052. doi:10.1002/2013JA019582

1567 Shinagawa, H., T. Tsugawa, M. Matsumura, T. Iyemori, A. Saito, T. Maruyama, H. Jin, M.
1568 Nishioka, and Y. Otsuka (2013), Two-dimensional simulation of ionospheric variations in the
1569 vicinity of the epicenter of the Tohoku-oki earthquake on 11 March 2011, *Geophys. Res. Lett.*,
1570 *40*, 5009-5013, doi:10.1002/2013GL05762

1571 Song, R., K. Hattori, X. Zhang, S. Sanaka (2020), Seismic-ionospheric effects prior to four
1572 earthquakes in Indonesia detected by the China seismo-electromagnetic satellite, *J. Atmos. Solar-*
1573 *Terr. Phys.*, *205*, 105291, [doi:10.1016/j.jastp.2020.105291](https://doi.org/10.1016/j.jastp.2020.105291)

1574 Tang, J., Y. Yao, L. Zhang, J. Kong (2015), Tomographic reconstruction of ionospheric electron
1575 density during the storm of 5-6 August 2011 using multi-source data, *Sci. Rep.* *5*, 13042, doi:
1576 10.1038/srep13042

1577 Thomas, J.N., Huard, J., and Masci, F. (2017). A statistical study of global ionospheric map total
1578 electron content changes prior to occurrences of $M \geq 6.0$ earthquakes during 2000–2014. *J.*
1579 *Geophys. Res. Space Phys.*, *122*, 2151–2161. doi:10.1002/2016JA023652

1580 Tsuji, H., and Hatanaka, Y. (2018). GEONET as Infrastructure for Disaster Mitigation. *J. Disaster*
1581 *Res.*, *13*(3), 424-432.

1582 Utada, H., and H. Shimizu (2014), Comment on “Preseismic ionospheric electron enhancements
1583 revisited” by K. Heki and Y. Enomoto, *J. Geophys. Res. Space Phys.*, *119*(7), 6011-6015,
1584 doi:10.1002/2014JA020044.

1585 Zettergren, M. D. and J. B. Snively (2019), Latitude and longitude dependence of ionospheric TEC
1586 and magnetic perturbations from infrasonic-acoustic waves generated by strong seismic events,
1587 *Geophys. Res. Lett.*, *46*, 1132–1140, doi:10.1029/2018GL081569.

1588